EXPERIMENTAL INVESTIGATION AND MODELING OF INERTANCE TUBES

by

Lothar O. Schunk

A thesis submitted in partial fulfillment of the
requirements for the degree of

MASTER OF SCIENCE

(MECHANICAL ENGINEERING)

at the

UNIVERSITY OF WISCONSIN-MADSION

2004

ABSTRACT

Three models describing and predicting the inertance effect in inertance tubes for pulse tube refrigerators are presented in this thesis. All models take the inertance, the compliance, and the resistance associated with oscillating gas flow in the inertance tube into account. The first model is based on electrical transmission line theory, the second is based on lumped components in which the resistance, compliance, and inertance are each represented by a single, lumped component in a network. The third model, introduced for the first time here, divides the inertance tube into a number of smaller tubes with each smaller tube represented by a resistance, compliance, and inertance element. The distributed lumped components can be combined in a network and used to predict mass flow, pressure, and their phase in the inertance tube.

To verify these models, the mass flow rate and pressure characteristics are measured for a number of different inertance tube geometries at different experimental conditions. The instantaneous pressure at various locations and the mass flow rate at the terminating end of the inertance tube can be measured relatively easily. The mass flow rate at the pulse tube end of the inertance tube presented a challenge and several techniques were used to measure this quantity. A commercially available, hot film anemometer was modified in order to measure the rather high mass flow into the inertance tube and withstand the high operating pressure. Unfortunately this modified anemometer failed to measure the true mass flow under oscillating flow conditions. Two methods of indirectly measuring the mass flow exiting the compressor were introduced. Although these two methods were shown to be capable of measuring the mass flow correctly under certain limiting conditions, they failed to accurately measure the mass flow rate consistently over a range of operating conditions. Therefore, the models are ultimately verified primarily through careful comparison with those quantities that can be easily and reliably measured; specifically the pressure variation along the length of the inertance tube and the mass flow rate into the reservoir. These experimental quantities are shown to be in good agreement with the model's predictions over a range of operating conditions.

Design charts are generated with the experimentally verified, distributed component model and are presented for various operating conditions in order to ease the design of inertance tubes for pulse tube refrigerators with kW-level refrigeration power. These design charts enable the designer to select inertance tube geometry that achieves a desired phase shift for a given level of acoustic power.

ACKNOWLEDGEMENTS

I want to thank my advisor, Professor Greg Nellis, and Professor John Pfotenhauer for their support during the entire research project. Their advice was very supportive, full of encouragement and insightful suggestions

My thanks also go to Mr. Edwin Dreier, Orrin Lokken, and Jim Maddocks who supported me setting up the experiments. Special thanks go to Dan Hoch who gave me great advice regarding machining.

My appreciation also goes to my fellow students in the Solar Energy Laboratory. They were a great source of practical help and encouragement during the project.

TABLE OF CONTENTS

LIST OF FIGURES

LIST OF TABLES

NOMENCLATURE

A	Area (m^2)
c	Compliance per unit length (s^2)
c_p	Heat capacity at constant pressure (J/kg-K)
c_v	Heat capacity at constant volume (J/kg-K)
C	Compliance (s^2m) (Chapter 2), heat capacity rate (W/K) (Chapter 3)
C_r	Reservoir compliance (ms^2) (Chapter 2), heat capacity ratio (Chapter 3)
C_2	Geometry factor (-)
D, d	Diameter (m)
$\bar{D}$	Dimensionless diameter (-)
$error$	Error (%)
f_{pin}	Pin correction factor (-)
f_r	Fanning friction factor (-)
F_f^*	Geometry factor (-)
g	Shunt conductance (not applicable)
G	Mass velocity (kg/m^2-s)
h	Specific enthalpy (J/kg), convection coefficient (W/m^2-K) (Chapter 3)
$\dot{H}$	Rate of entropy (J/s)
l	Inertance per unit length ($1/m^2$)
I	Current (A) $\dot{m}_{C[1]}$
I_0	Modified zero order Bessel function first kind (-)

I_1	Modified zero order Bessel function second kind (-)
j	Imaginary number (-), Colburn factor (-) (Chapter 3)
K_0	Modified first order Bessel function first kind (-)
K_1	Modified first order Bessel function second kind (-)
L	Length (m), Inertance (1/m) (Chapter 2)
$\overline{L}$	Dimensionless length (-)
Le	Inertance tube length (m)
$L_{s,r}$	Real pin length (m)
$L_{s,u}$	Uncorrected pin length (m)
m	Mass (kg or g), fin number (-) (Chapter 3)
$\dot{m}$	Mass flow rate(kg/s or g/s)
N_f	Number of fins (-)
Nu	Nusselt number (-)
NTU	Number of transfer units (-)
out	Sensirion sensor output (sccm)
p	Porosity (-)
P	Pressure (Pa)
$\tilde{P}, \overline{P}$	Pressure amplitude (Pa), mean pressure (Pa)
$\tilde{P}_r$	Ratio of pressure variation at reservoir (-)
Pr	Prandl number (-)
$\dot{Q}$	Rate of heat transfer (W)
r	Radius (m), Resistance per unit length ($1/m^2$-s) (Chapter 2)

r_c	Crankshaft radius (m)
R	Specific gas constant (J/kg-K) or resistance (1/m-s)
Re	Reynolds number (-)
s	Length (m)
s_w	Spacing between screen wires (m)
t	Time (s)
$T,\bar{T}$	Temperature, mean temperature (K)
u	Specific internal energy (J/kg)
U	Internal Energy (J)
UA	Overall conductance (W/K)
v	Velocity (m/s)
V	Volume (m^3), Voltage in chapter 2.1 (V)
$\dot{V}$	Volumetric flow rate (m^3/s)
$\dot{W}$	Acoustic power, rate of work (W)
$\bar{W}$	Dimensionless acoustic power (-)
x	Position in x-direction (m)
y	Constant (-)
z	Constant (-)
Z	Impedance, Total impedance (1/m-s)
Z_0	Characteristic impedance (1/m-s)

Subscripts

b	Base
c	Cold
co	Compressor
C	Compliance
ent	Entrance effect into reservoir
f	Fin, final (Chapter 4)
fr	Frontal
h	Hot or hydraulic
He	Helium
HZ	Operating frequency (1/s)
i	Element index (Chapter 2), inlet or inner (Chapter 3), initial (Chapter 4)
ID	Inner diameter (mm)
$length$	Length
L	Inertance
max	Maximum
min	Minimum
n	Number of elements
$N2$	Nitrogen
o	Outlet, outer
OD	Outer Diameter (inch)
p	In parallel

pt	Pulse tube
r	Reservoir
R	Resistance
rg	Regenerator
s	In series (Chapter 2), Screens (Chapter 3)
t	Total
screens	Screens
spacing	Spacing
std	Standard conditions
swept	Swept
w	Wire
W	Water

Greek Symbols

α	Specific surface area (1/m)
α_0	Speed of sound (m/s)
γ	Heat capacity ratio (-)
δ, Δ	Difference in, change in (-)
δ_u	Viscous penetration depth (m)
ε	Heat exchanger effectiveness (-)
η_f	Fin efficiency (-)
η_0	Overall fin efficiency (-)
θ	Phase angle (degrees)

κ	Polytropic exponent (-)
λ_c	Ratio of the crankshaft radius to the length of the connecting rod (-)
λ	Wavelength (m)
μ	Viscosity (kg/m-s)
π	3.14159265359
$\rho, \overline{\rho}$	Density, mean density (kg/m^3)
ω	Angular frequency (1/s)

1 INTRODUCTION

1.1 Motivation

The pulse tube is among the simplest of all cryocoolers and has the advantage over the Stirling cryocooler of having no moving parts in the cold region; resulting in high reliability, long life, and low vibration at the cold tip. However, the thermodynamic efficiency of early versions of the pulse tube was less than the Stirling cryocooler. The Stirling cryocooler generally showed better performance because the phase between the oscillating mass flow and pressure in the expansion space is easily adjustable using the low-temperature displacer. The optimal phase shift produces the maximum refrigeration effect per unit of working fluid mass; the working fluid mass must be processed by the regenerator and most of the losses in the cryocooler are related to the regenerator. Therefore, optimizing the refrigeration effect per unit of working fluid mass corresponds approximately to optimizing the thermodynamic efficiency of the cryocooler.

Figure 1.1 shows the basic pulse tube (a), the orifice pulse tube (b), and the pulse tube with inertance tube (c). The physics of operation that causes the cooling effect in the pulse tube are described based on the orifice pulse tube (b), in this section [1]. Adiabatic compression is assumed for the ideal orifice pulse tube and the cycle is divided into four steps. First (1), the helium gas moves down towards the reservoir end of the pulse tube as the gas is compressed. Then (2) the heated and compressed gas flows into the reservoir because it is at a higher pressure than the mean pressure in the reservoir. Heat is exchanged at the warm end of the pulse tube and in the reservoir with ambient until the pressure decreases to the mean pressure in the pulse tube and the flow stops. Next (3), the gas is expanded in the pulse tube. In the final step (4), the expanded, colder gas moves towards the cold end of the pulse tube (regenerator end). Heat is absorbed from the heat source that is attached to the pulse tube at the cold end. Energy balance considerations reveal that the amount of heat absorbed is (in the ideal approximation) equal to the acoustic power transferred through the pulse tube. The 4th step ends when the average pressure is reached again, the flow stops and a new cycle begins. The regenerator's large heat capacity serves as a thermal memory maintaining the temperature gradient between the compressor and the pulse tube. The pulse tube also must be long enough that the hot gas never reaches the cold end and vice versa. It acts like an insulator between the warm gas at the reservoir end and the cold gas at the regenerator end of the pulse tube. Gas at the midpoint of the pulse tube never leaves the pulse tube and creates a temperature gradient between the hot and warm gas that causes the mentioned insulation effect. The net effect of the gas motion within the pulse tube is to transfer energy in the form of PV work (or acoustic power) from the cold to the warm end while maintaining a thermal insulation between the hot and cold ends.

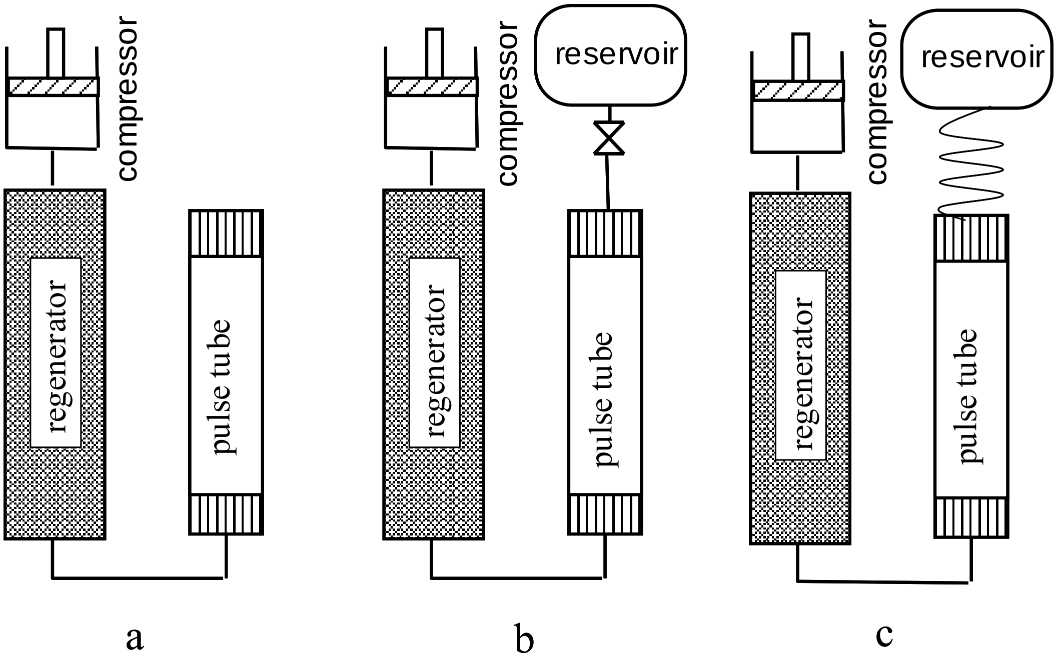

Figure 1.1 Basic pulse tube (a), orifice pulse tube (b), and pulse tube with inertance tube (c)

The introduction of the orifice pulse tube by Mikulin [2] and the double inlet pulse tube by Zhu et al. [3], have allowed pulse tubes configurations to approach, and in some cases exceed [4], the performance of a Stirling cryocooler. The orifice in the orifice pulse tube provided a convenient method of controlling the phase between the mass flow rate and pressure and led directly to the increase in efficiency. A limitation of the orifice pulse tube is that the mass flow rate must always lead the pressure; in the limiting case, the mass flow rate and pressure ratio may be in phase with one another. This limitation does not allow the optimal phase to be achieved in which the pressure would lead the mass flow rate at the inlet to the expansion space.

An alternative means of adjusting the phase between the pressure and mass flow rate is with an inertance tube, as reported by Kanao et al [5]. The inertance tube does not suffer from the same limitation as the orifice; through proper selection of the inertance tube geometry it is possible to force the mass flow rate to either lead or lag the pressure. Therefore, proper implementation of an inertance tube in a pulse tube has the potential to improve the performance of the cryocooler. Inertance is the dynamic characteristic associated with the inertia of a rapidly moving fluid. The inertance, together with the tube's resistance and compliance as well as the compliance of the terminating reservoir, provides a complex impedance at the warm end of the pulse tube. Through proper selection of the inertance geometry it is possible to adjust this complex impedance and therefore achieve the necessary phase between flow and pressure that is consistent with maximum system performance.

The phase shift associated with the inertance tube may be predicted with a lumped model based on analogy with electrical components, as previously suggested by Roach and Kashani [6] or a more detailed model based on either acoustic theory [7], or electrical transmission-line theory. A third model is suggested in this thesis based on dividing the inertance tube into a large number of lumped components. Unfortunately, very little data or measurements exist to verify the predictability of these models. In cooperation with NIST, the pressure-flow characteristics of different inertance tube geometries and using different operating conditions has been measured. These measurements provide a database that allows the verification of the various predictive models for inertance tube behavior. The models themselves are subsequently used to generate design charts to facilitate the selection of the optimal inertance tube for a particular application. Measurements for inertance tubes operating with relatively small (10’s of W) levels of acoustic power have been conducted at NIST whereas measurements for larger (kW) levels of acoustic power have been made at the

Cryogenic Research Lab at the University of Wisconsin, Madison and are described in this thesis.

The next section describes more completely the importance of the phase between the mass flow and the pressure oscillation at the expansion space. The importance of achieving the optimal phase is shown in terms of minimizing the regenerator loss for a given refrigeration effect.

1.2 Inertance tubes in pulse tube cryocoolers

The objective of the regenerator in a pulse tube is to transmit acoustic or PV power from the compressor to the cold end of the pulse tube. The majority of the losses in a pulse tube refrigerator are related to the regenerator; these losses are due to thermal ineffectiveness, power dissipation associated with frictional pressure drop, pressurization of the void volume, and axial thermal conduction. Thermal ineffectiveness and loss of acoustic power due to frictional pressure drop typically dominate the regenerator loss and these scale directly with the amplitude of the mass flow rate that the regenerator is required to process. Based on this discussion, it is clear that the most efficient pulse-tube will provide the largest amount of acoustic power to the cold end for the smallest amount of mass flow rate.

The time-averaged acoustic power $\dot{W}$ through the regenerator is given approximately by equation (1.1) [8].

$$\dot{W} = \tilde{P}\dot{V} = 0.5\left|\tilde{P}\right|\left|\dot{V}\right|\cos\theta = 0.5\left|\tilde{P}\right|\frac{\left|\dot{m}\right|}{\bar{\rho}}\cos\theta = 0.5R\bar{T}\frac{\left|\tilde{P}\right|}{\bar{P}}\left|\dot{m}\right|\cos\theta \qquad (1.1)$$

where $\tilde{P}$ is the oscillating component of pressure, $\dot{V}$ is the volumetric flow rate, θ the phase between pressure and mass flow, $\dot{m}$ is the mass flow rate, $\bar{\rho}$ is the average density, R is the specific gas constant of the operating gas, $\overline{T}$ is the average temperature, $\overline{P}$ is the average pressure, and the line brackets denote the absolute value. The expression after the first equal sign represents the general expression for acoustic power, the cyclic integral of the instantaneous product of pressure and volumetric flow rate at the cold end of the regenerator. The second expression is related to the harmonic approximation of this integral; the pressure and volumetric flow rate are taken to be pure sinusoids and θ is the difference in phase between them. The third expression is obtained by substituting the ratio of the mass flow rate to the nominal or average density for the volumetric flow rate. Finally, the fourth expression is obtained by using the ideal gas to substitute for the average density.

Equation (1.1) shows that the acoustic power is proportional to the mass flow rate that is in phase with the pressure variation. In the context of phasors, the acoustic power is given by the product of the projection of the mass flow vector onto the pressure wave vector and the magnitude of the pressure variation. The acoustic power flow is essentially constant through the refrigerator, but the regenerator losses are proportional to the magnitude of the mass flow in the regenerator. Hence, in order to minimize the ratio of the regenerator losses to the transmitted acoustic power, the phase (θ) should be minimized within the regenerator (not at the inlet to the expansion space). The mass flow rate entering the hot end of the regenerator will tend to lead the mass flow rate leaving the cold end of the regenerator due to the compliance associated with the void volume in the regenerator. The optimally designed pulse tube cryocooler will therefore set the phase between the pressure and mass flow rate to zero near the midpoint of the regenerator. The phase between the mass flow rate and pressure in this study are approximately -30° (mass flow rate leads the pressure) at the hot end of the regenerator and 30° (mass flow rate lags the pressure) at the cold end of the regenerator. In general the phase shift that occurs will depend on the void volume and flow resistance associated with the regenerator. The optimum phase-relations for a pulse tube refrigerator with inertance tube and reservoir is shown in Figure 1.2. Note that the use of the inertance tube allows a negative phase (the pressure leads the mass flow rate) at the hot end of the pulse tube. The mass flow rates in the components of the simplified pulse tube refrigerator (pulse tube, regenerator, and compressor) are presented in phasor notation. The phasor notation shows magnitudes and phase angle of the mass flow rates at various locations in the system relative to the pressure variation (note that the pressure is assumed to be spatially uniform in the system). Therefore, a mass flow phasor that lies on the real axis is in phase with the pressure variation and one that lies on the imaginary axis is 90º out of phase with the pressure.

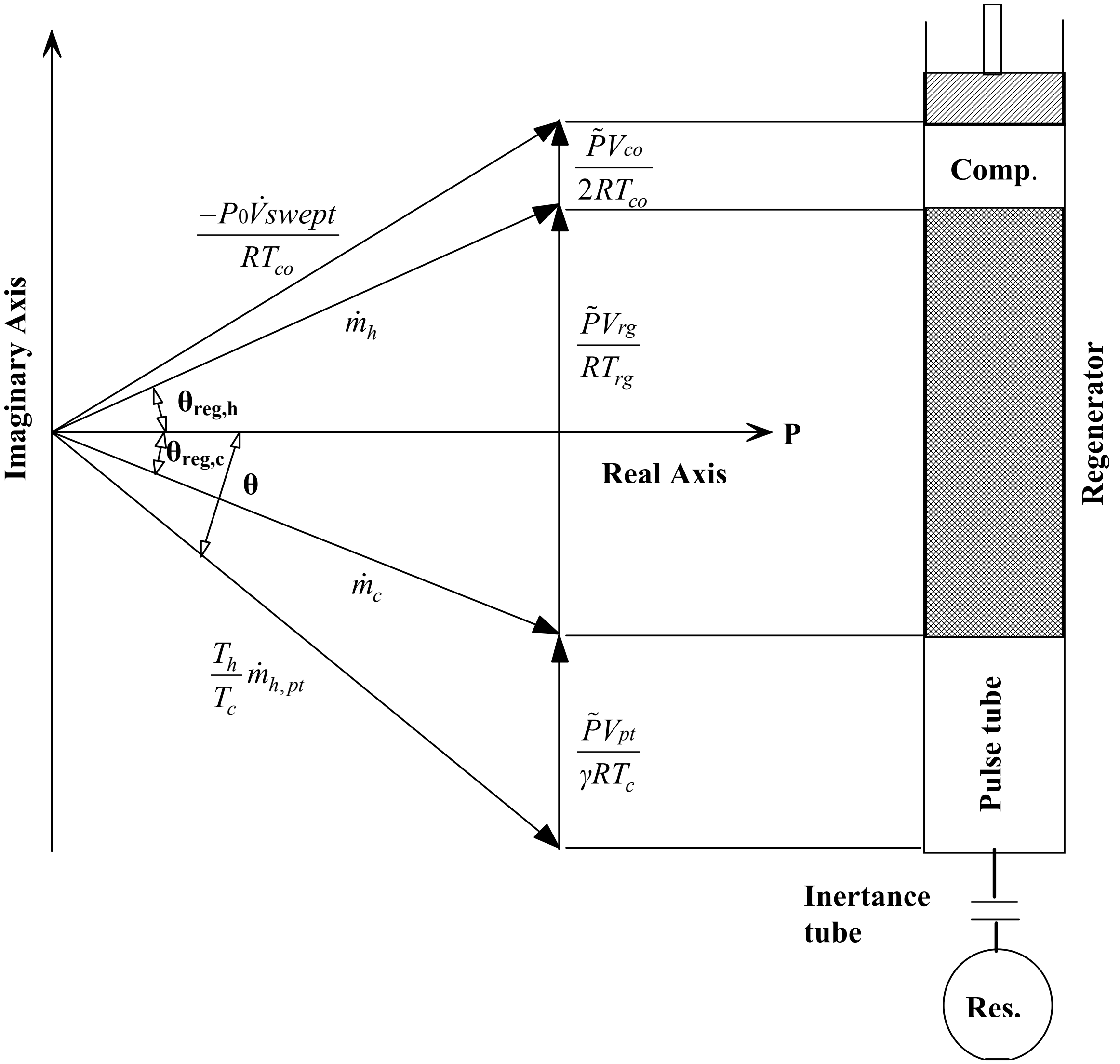

Figure 1.2 Phasor diagram for the optimal phase shift in a pulse tube refrigerator. Note that the optimal phase shift requires a relatively large negative phase at the warm end of the pulse tube that can only be obtained using an inertance tube.

In comparison, the typical phase-relations for a pulse tube refrigerator using a simple orifice rather than an inertance tube is shown in Figure 1.3

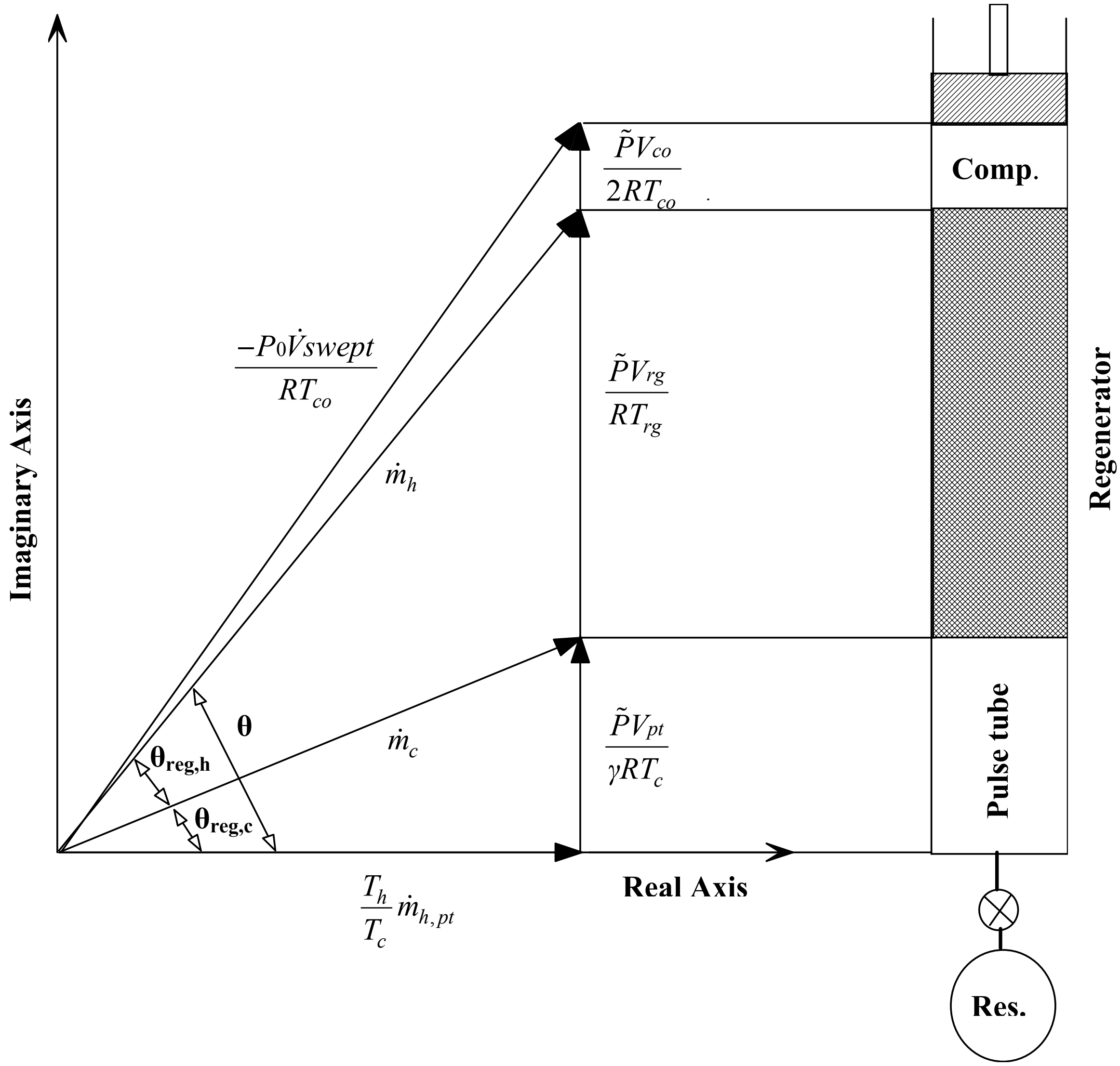

Figure 1.3 Phasor diagram for phase shift that can be achieved with an orifice. Note that the phase at the warm end of the pulse tube is zero and therefore the optimal phase shift, shown in Figure 1.2, cannot be achieved.

Some further discussion of the phasor diagrams shown in Figure 1.2 and Figure 1.3 is warranted. The law of mass conservation in the regenerator and compressor space and the law of energy conservation in the pulse tube may also be represented by the addition of phasors as shown in Figure 1.2 and Figure 1.3 and described in equations (1.2) through (1.9). The mass balance in the regenerator is,

$$\dot{m}_c + \frac{\tilde{P} V_{rg}}{R T_{rg}} - \dot{m}_h = 0 \tag{1.2}$$

where $\dot{m}_c$ represents the mass flow rate at the regenerator's cold end (also the mass flow rate into the pulse tube), $\dot{m}_h$ is the mass flow rate at the regenerator's warm end, and V_{rg} and T_{rg} are the regenerator's volume and average temperature, respectively. The second term in Eq. (1.2) represents the mass accumulated in the regenerator, assuming ideal gas behavior. The mass balance for the compressor space is,

$$\dot{m}_h + \frac{\overline{P} \dot{V}_{swept}}{R T_{co}} + \frac{\tilde{P} V_{swept}}{2 R T_{co}} = 0 \tag{1.3}$$

where $\overline{P}$ is the average pressure in the compressor, $\tilde{P}$ is the oscillating part of the compressor's pressure, $\dot{V}_{swept}$ is the change of the compressor's swept volume with respect to time, V_{swept} the swept volume, and T_{co} is the average compressor temperature. The first two terms of Eq. (1.3) represent the mass flow rate that is exiting or entering the compressor and the third term represents the mass accumulated in the compressor. The energy balance in the pulse tube is not as trivial as the mass balances, so the derivation is presented in the following equations. Figure 1.4 shows schematically the pulse tube's energy balance.

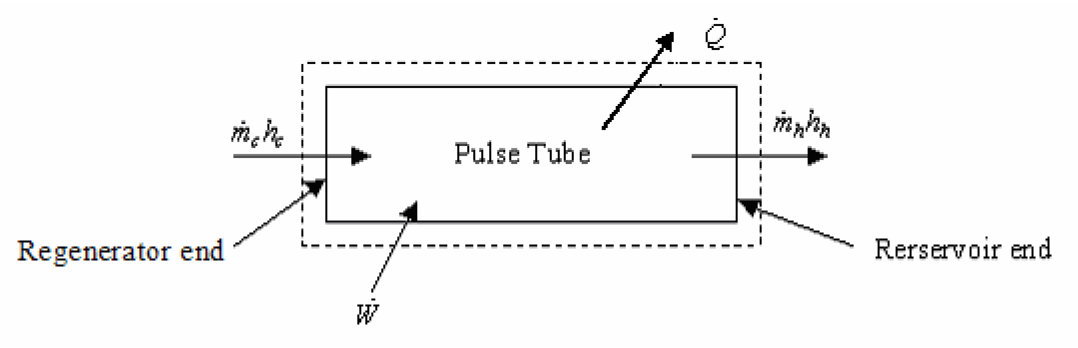

Figure 1.4 Pulse tube's energy balance

The general equation for the energy conservation is given by:

$$\frac{dU}{dt} = \dot{Q} - \dot{W} - \dot{m}_c\, h_c + \dot{m}_h\, h_h \tag{1.4}$$

where dU/dt represents the change of internal energy with respect to time, $\dot{Q}$, $\dot{W}$, and $\Delta\dot{H}$ represent the rate of heat, work, and enthalpy, respectively. If a fixed-boundary control volume associated with the adiabatic portion of the pulse tube is defined, then the rate of work and heat transfer entering the pulse tube is zero; therefore Eq. (1.4) reduces to,

$$\frac{dU}{dt} + \dot{m}_c h_c - \dot{m}_h\, h_h = \frac{d(u\rho V_{pt)}}{dt} + \dot{m}_c h_c - \dot{m}_h\, h_h = 0 \tag{1.5}$$

where u is the specific internal energy, ρ is the density of the gas in the pulse, V_{pt} is the volume of the pulse tube, $\dot{m}$ represents mass flow rate, and h is the specific enthalpy, the indices h and c denote at the hot end and the cold end, respectively. Assuming perfect gas behavior allows the internal energy and enthalpy to be written as,

$$u = c_v T = c_v \frac{P}{\rho R} \tag{1.6}$$

$$h = c_p\, T \tag{1.7}$$

Substituting equations (1.6) and (1.7) into equation (1.5) yields,

$$\frac{c_v \dot{P} V_{pt}}{c_p R} + \dot{m}_c T_c - \dot{m}_h T_h = 0 \tag{1.8}$$

where P is the average pressure in the pulse tube, and T_h and T_c are the pulse tube's hot and cold end temperatures, respectively. Replacing the ratio of the heat capacities by γ and dividing by the cold end temperature (T_c), leads to Eq. (1.9). Note that Eq. (1.9) can be used to understand the relationship between the phasors in Figure 1.2 and Figure 1.3 that correspond to the mass flow rate at the hot and cold ends of the pulse tube but is not strictly valid relative to predicting the performance of the pulse tube.

$$\frac{\dot{P} V_{pt}}{\gamma R T_c} + \dot{m}_c - \dot{m}_h \frac{T_h}{T_c} = 0 \tag{1.9}$$

The phase-relations between the mass flow rates and pressure in Figure 1.2 and 1.3 can be understood by examining equations (1.2), (1.3), and (1.9). Recall that the pressure phasor lies on the real axis. Because the pressure and its time derivative are sinusoidal and the pressure everywhere in the pulse tube is the same, the rate at which mass is accumulated in the volumes represented by the pulse tube, regenerator, and compressor must lag the pressure by 90° and therefore be in the direction of the imaginary axis. Hence, the phasor equivalent of equations (1.2), (1.3), and (1.9) are represented by the vector additions shown in Figure 1.2 and 1.3.

Through proper selection of the geometry of the inertance tube and reservoir, the phase at the warm end of the pulse tube can be set to essentially any value, positive or negative. Figure 1.2 illustrates that an optimal phase will be in the range of $-45^\circ \text{to} -60^\circ$, forcing the mass flow at the warm end of the regenerator to lag the pressure by 30° and the mass flow rate at the cold end of the regenerator to lead the pressure by 30°. Thus the desired 0° phase is created at the midpoint of the regenerator and the magnitude of the average mass flow rate processed by the regenerator (the average of $\dot{m}_h$ and $\dot{m}_c$) is minimized for a given acoustic power. Minimizing the magnitude of the average mass flow rate in the regenerator results in smaller regenerator losses and allow a larger fraction of the acoustic power to be converted to refrigeration power.

Figure 1.3 shows the mass flows in phasor notation when the inertance tube is replaced with an orifice. The orifice coupled to a reservoir allows for only a resistive and capacitive impedance (there is no possibility of an inductive impedance). Therefore, the mass flow rate at the warm end of the pulse tube can never lead the pressure, as it did in Figure 1.2. Rather, the best possibility occurs when the reservoir volume is made infinitely large which forces the mass flow rate at the end of the pulse tube to be in phase with the pressure; this is seen in Figure 1.3 by the fact that the mass flow rate lies on the real axis. It can be clearly seen from Figure 1.3 that the average mass flow rate in the regenerator for the same acoustic power is much higher than in Figure 1.2. This discussion motivates the need for inertance tubes in high efficiency pulse tube systems in order to minimize regenerator losses by providing the optimum phase shift.

1.3 Thesis overview

The objective of this thesis is to provide models that are capable of determining the optimum inertance tube geometry for pulse tubes operating over a range of power levels, frequencies, and pressure ratios. In order to verify the models' predictions, experiments have been conducted at different acoustic power levels and with different inertance tube geometries. The most direct technique for verifying an inertance tube model is the simultaneous measurement of the oscillating pressure and mass flow rate at the inlet to the inertance tube. Unfortunately, there are no flow sensors commercially available that can be used to measure the large, high frequency mass flow rate associated with kW level pulse tubes. A significant amount of effort was directed at measuring this mass flow rate. The techniques that were used included adapting a commercial sensor for this application and indirectly measuring the mass flow rate through application of conservation of mass. While the latter method eventually resulted in some success, the theoretical error associated with the technique was 10-15% and in practice the error was probably closer to 20-25%. This level of uncertainty was not low enough to allow a direct verification of the model. Instead, detailed measurements were made of the pressure at both ends of the inertance tube as well as the pressures along the length of the tube. In addition, the mass flow rate at the interface between the reservoir and inertance tube was measured. These accurately measured quantities were compared with the model predictions over a large range of operating conditions and the agreement was found to be excellent. The agreement between the measured mass flow rate at the inertance tube inlet and the model’s prediction for this quantity was less satisfactory, probably due to the large uncertainty in the mass flow rate measurement.

Chapter 2 describes the different models that have been proposed to predict characteristics of a given inertance tube geometry. These models can be used to find the desired optimum inertance tube geometry (length and diameter) for any operating condition. Chapter 3 provides a model for the after cooler heat exchanger that was required for the experimental setup. The basic experimental setup is described in Chapter 4. The various methods that were used to measure the high, oscillating mass flow are also described in this chapter. Experimental results and the comparison between the model's prediction and the measured data are presented in Chapter 5. Chapter 6 concludes the thesis by presenting design charts that can be used to specify the appropriate inertance tube geometry for some typical operating conditions.

2 INERTANCE TUBE MODELS

In the 1950s Rohman and Grogan derived equations describing the capacity, inductance, and resistance of oscillating gas in pneumatic transmission lines [9]. They also introduced the electrical transmission line analog and described the concept of making the driving force, pressure ($\tilde{P}$), in pneumatic systems analogous to voltage (V) in electrical systems and the mass flow rate ($\dot{m}$) in pneumatic systems analogous to current (I) in electrical systems. The capacitance (known as compliance in a pneumatic system), inductance (known as inertance in a pneumatic system), and the resistance that arise from the gas flow in the tube are made analogous to electrical capacitance, inductance, and resistance, respectively.

Three different models that are capable of predicting the phase shift and mass flow associated with the inertance tube are presented in this chapter. The first is based on electrical transmission line theory. The second uses a single set of lumped electrical components, as suggested by Roach [6]. The final model is presented here for the first time and is derived by splitting a continuous inertance tube into an arbitrary but finite number of lumped components and deriving the impedance based on the combination of these components. This model also has the advantage of including entrance effects at the reservoir end (related to expansion/contraction of the gas) and allowing the characteristics of the lumped components to vary based on the varying conditions that exist along the tube.

2.1 Transmission Line model

Figure 2.1 illustrates the simplified network associated with an electrical transmission line. *G* symbolizes the generator and Z_r the load; r, *l, c,* and *g* denote resistance, inductance, capacitance, and shunt conductance per unit length, respectively. *V* and *I* represent voltage and current and *x* the position.

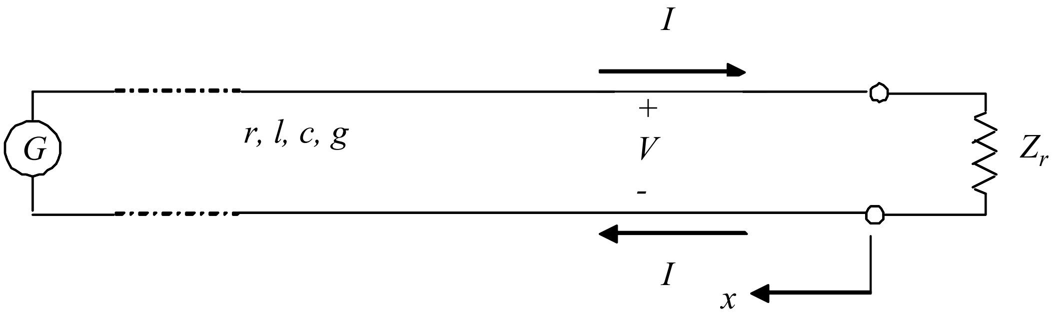

Figure 2.1 Simplified transmission line network

The rate of change of voltage with respect to distance is equal to the product of the local current and a complex constant (z), which is expressed in terms of resistance per unit length and inductance per unit length:

$$\frac{dV}{dx} = zI = (r + j\omega l)I \tag{2.1}$$

where j is equal to $\sqrt{-1}$ and ω the frequency of the system operation. The rate of change of current with respect to distance is the product of voltage and another complex constant (y) that is expressed in terms of shunt conductance per unit length (g) and capacitance per unit length (c).

$$\frac{dI}{dx} = yV = (g + j\omega c)V \tag{2.2}$$

The acoustic analog of voltage is the oscillating component of pressure ($\tilde{P}$) and the analog for current is the mass flow rate ($\dot{m}$). Acoustic equivalents of the electrical resistance, capacitance, and inductance can be found in literature [6, 7]. The resistance per unit length of the flow in the inertance tube arises from viscous drag between neighboring fluid particles and can be expressed as

$$r = \frac{64 f_r \dot{m}}{\pi^3 \bar{\rho} D^5} \tag{2.3}$$

where f_r is the Fanning friction factor, D the tube internal diameter, and $\bar{\rho}$ the mean density of the operating gas. Note that the mass flow rate referred to in Eq. (2.3) is the amplitude of the oscillating mass flow rate; therefore, the resistance is based on the rms value of the mass flow in the tube, accounting for the extra factor of $2/\pi$ in Eq. (2.3) as compared to the definition that may be found in most fluids textbooks. The friction factor is computed according to [10]:

$$f_r = 0.046\, Re^{-0.2} \tag{2.4}$$

where Re is the Reynolds number. This correlation provides an approximation for the flow in smooth tubes for Reynolds numbers greater than 2×10^4. Since the Reynolds number of the average flow in the inertance tube is always greater than the lower boundary of this correlation, equation (2.4) provides a reasonable approximation for the friction factor.

The inertance per unit length results from the inertia of the gas in the tube and becomes significant at high frequencies [9]. The tube's compliance results from the compressibility of the gas [9].

$$l = \frac{4}{\pi D^2} \tag{2.5}$$

$$c = \frac{\pi D^2}{4\gamma R\overline{T}} \tag{2.6}$$

where R denotes the gas constant, $\overline{T}$ the average temperature, and γ the ratio of the specific heat capacities. The reservoir compliance (C_r) is related to its volume (V_r):

$$C_r = \frac{V_r}{\gamma R\overline{T}} \tag{2.7}$$

Rewriting equations (2.1) and (2.2) in terms of the acoustic system yields equations (2.8) and (2.9). Note that there is no acoustic equivalent to the shunt conductance term (g) in Eq. (2.2) that represents leakage along the line in electrical systems.

$$\frac{d\tilde{P}}{dx} = z\,\tilde{P} = \left(\frac{64 f_r \dot{m}}{\pi^3 \overline{\rho}\, D^5} + j\,\omega \frac{4}{\pi\, D^2} \right) \dot{m} \tag{2.8}$$

$$\frac{d\dot{m}}{dx} = y\tilde{P} = \left(j\omega \frac{\pi D^2}{4\gamma R\overline{T}} \right) \tilde{P} \tag{2.9}$$

Two possible solutions for this pair of simultaneous differential equations are [11]:

$$\tilde{P} = \tilde{P}_1 \exp\left(\sqrt{z\,y}\,x\right) + \tilde{P}_2 \exp\left(-\sqrt{z\,y}\,x\right) \tag{2.10}$$

$$\dot{m} = \dot{m}_1 \exp\left(\sqrt{z\,y}\,x\right) + \dot{m}_2 \exp\left(-\sqrt{z\,y}\,x\right) \tag{2.11}$$

For convenience, only the magnitudes of the complex quantities z and y are carried through the following equations. Substituting equations (2.10) and (2.11) into equations (2.8) and (2.9), respectively, and simplifying yields:

$$\tilde{P}_1 \exp\left(\sqrt{z\,y}\,x\right) - \tilde{P}_2 \exp\left(-\sqrt{z\,y}\,x\right) = \sqrt{\frac{z}{y}}\dot{m}_1 \exp\left(\sqrt{z\,y}\,x\right) + \sqrt{\frac{z}{y}}\dot{m}_2 \exp\left(-\sqrt{z\,y}\,x\right) \qquad (2.12)$$

$$\tilde{P}_1 \exp\left(\sqrt{z\,y}\,x\right) + \tilde{P}_2 \exp\left(-\sqrt{z\,y}\,x\right) = \sqrt{\frac{z}{y}}\dot{m}_1 \exp\left(\sqrt{z\,y}\,x\right) - \sqrt{\frac{z}{y}}\dot{m}_2 \exp\left(-\sqrt{z\,y}\,x\right) \qquad (2.13)$$

If equations (2.12) and (2.13) are added and a characteristic impedance (Z_o) is defined, then the solution can be written as:

$$\tilde{P}_1 = \sqrt{\frac{z}{y}}\,\dot{m}_1 = Z_o\,\dot{m}_1 \qquad (2.14)$$

$$\tilde{P}_2 = -\sqrt{\frac{z}{y}}\,\dot{m}_2 = -Z_o\,\dot{m}_2 \qquad (2.15)$$

$$Z_o \equiv \sqrt{\frac{z}{y}} \qquad (2.16)$$

At the reservoir end of the inertance tube (i.e., x= 0), the ratio of the pressure variation ($\tilde{P}_r$) to the mass flow rate ($\dot{m}_r$) is equal to the impedance of the reservoir (Z_r), which is assumed here to be completely capacitive (C_r).

$$Z_r = \frac{1}{j\,\omega\,C_r} = \frac{\tilde{P}_r}{\dot{m}_r} = \frac{\tilde{P}_1 + \tilde{P}_2}{\dot{m}_1 + \dot{m}_2} \tag{2.17}$$

Substituting equations (2.14) and (2.15) into equation (2.17) and simplifying leads to the following expressions for the pressure and mass flow rate, both with respect to axial position x:

$$\tilde{P}(x) = \frac{\tilde{P}_r}{2Z_r}\left[\left(Z_r + Z_o\right)\exp\left(\sqrt{z\,y}x\right) + \left(Z_r - Z_o\right)\exp\left(-\sqrt{z\,y}\,x\right)\right] \tag{2.18}$$

$$\dot{m}(x) = \frac{\tilde{P}_r}{2Z_r\,Z_o}\left[\left(Z_r + Z_o\right)\exp\left(\sqrt{z\,y}\,x\right) + \left(Z_o - Z_r\right)\exp\left(-\sqrt{z\,y}\,x\right)\right] \tag{2.19}$$

The ratio of equations (2.18) and (2.19) at the pulse tube end of the inertance tube (i.e., at $x = Le$, where Le is the length of the inertance tube) represents the impedance of the inertance tube and the reservoir together, as seen by the pulse tube (Z_{pt}). If the exponentials are replaced by hyperbolic functions, then the impedance may be written as:

$$Z_{pt} = Z_o \frac{Z_r + Z_o\tanh\left(\sqrt{zy}\,Le\right)}{Z_o + Z_r\tanh\left(\sqrt{zy}\,Le\right)} \tag{2.20}$$

With known characteristics of the inertance tube and reservoir, it is possible to determine the complex impedance. The angle of this complex impedance (θ) is the phase shift between $\dot{m}$ and $\tilde{P}$. The acoustic power (W) flowing through a pulse-tube is given by equation (2.21).

$$W = \frac{\dot{m}\,\tilde{P}}{2\bar{P}} R\,\bar{T}\cos\theta \tag{2.21}$$

Substituting $\dot{m}$ for the impedance leads to equation (2.22).

$$W = R\bar{T}\frac{\tilde{P}^2}{2\bar{P}\left|Z_{pt}\right|}\cos\theta \tag{2.22}$$

The EES code used to implement the transmission line model is contained in Appendix A.

2.2 Lumped component model

A simple lumped component model for the inertance tube is presented in this section. The lumped model is less rigorous or accurate than the transmission line theory but more physically intuitive and also represents a model that is used by many pulse tube designers. It is therefore valuable to compare experimental data with the lumped component model as well as the more complex models derived in the previous and subsequent sections. The lumped component model treats the inertance tube and the reservoir as a simple network of lumped electrical components shown in Figure 2.2.

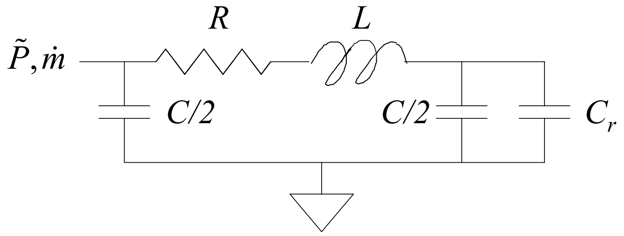

Figure 2.2 Lumped component model

The resistance (*R*), compliance (*C*), and inertance (*L*) of the inertance tube are represented each by a single element. The characteristics of these elements are computed according to:

$$R = \frac{64 f_r \dot{m} Le}{\pi^3 \overline{\rho} D^5} \tag{2.23}$$

$$C = \frac{\pi D^2 Le}{4\gamma R\overline{T}} \tag{2.24}$$

$$L = \frac{4 Le}{\pi D^2} \tag{2.25}$$

The impedance of the network shown in Figure 2.2 is computed according to:

$$Z_{pt} = \left[\left(\frac{1}{j\omega C/2} \right)^{-1} + \left(\frac{1}{j\omega \left(C_r + C/2 \right)} + R + j\omega L \right)^{-1} \right]^{-1} \tag{2.26}$$

The EES code used to implement the lumped component model is contained in Appendix B.

2.3 Distributed component model

The final model of the inertance tube considered here is a lumped component model, similar to the one described in the previous section. However, rather than lumping the resistive, inductive, and capacitive behavior of the inertance tube into single components, this model divides the inertance tube into *n* increments; each increment is represented by a resistance, compliance, and inertance. The model is physically intuitive and realistic. It has the additional advantages of including the entrance effects associated with the expansion/contraction of the gas as it enters/leaves the reservoir and the varying conditions that exist along the tube can be explicitly accounted for by varying the characteristics of the impedance components according to the local conditions. Figure 2.3 shows the lumped component network with 2 increments.

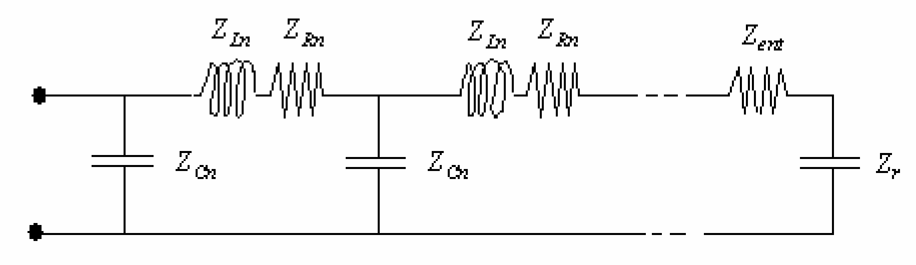

Figure 2.3 Distributed component model with 2 components (i.e., $n = 2$)

The components labeled Z_{Ln}, Z_{Rn}, and Z_{Cn} in Figure 2.3 represent the inertance, resistance, and compliance associated with each tube increment, respectively. These parameters are obtained by dividing the corresponding total values by the number of increments (n). An advantage of this distributed model is that the resistance of each increment may be calculated independently based on the local mass flow rate along the tube. The pressure gradient is nominally proportional to the mass flow rate squared and therefore the resistance, which is a linearization of the slope of the pressure gradient with mass flow rate, must vary according to the local mass flow rate. The distributed model can explicitly account for this effect through an iterative, relaxation procedure wherein the resistance values are updated based on the local mass flow rate.

The component in Figure 2.3 labeled Z_{ent} represents the resistance associated with the contraction/expansion as the gas leaves/enters the reservoir. The component labeled Z_r represents the compliance associated with the reservoir volume. Figure 2.4 illustrates how the circuit shown in Figure 2.3 can be considered as a set of cascaded impedances; the reservoir is represented by the innermost impedance and the total inertance tube/reservoir combination is represented by the outermost impedance. Figure 2.4 suggests the technique that can be used to determine the impedance of the entire network (note that Figure 2.4 shows the first three increments and the *n*' th increment only). The mass flow rates through the components of the network and the local pressures are also indicated in Figure 2.4. Their arrangements was chosen in a manner that allows the Engineering Equation Solver (EES) software to quickly and reliably solve the set of equations that is presented later in this section. The indices *s*, *p*, and *RL* denote in series, in parallel, and the resistance and inertance of one increment lumped together in series, respectively. Integer numbers label the indices in the solution arrays for mass flow, pressure, impedance in series, and impedance in parallel.

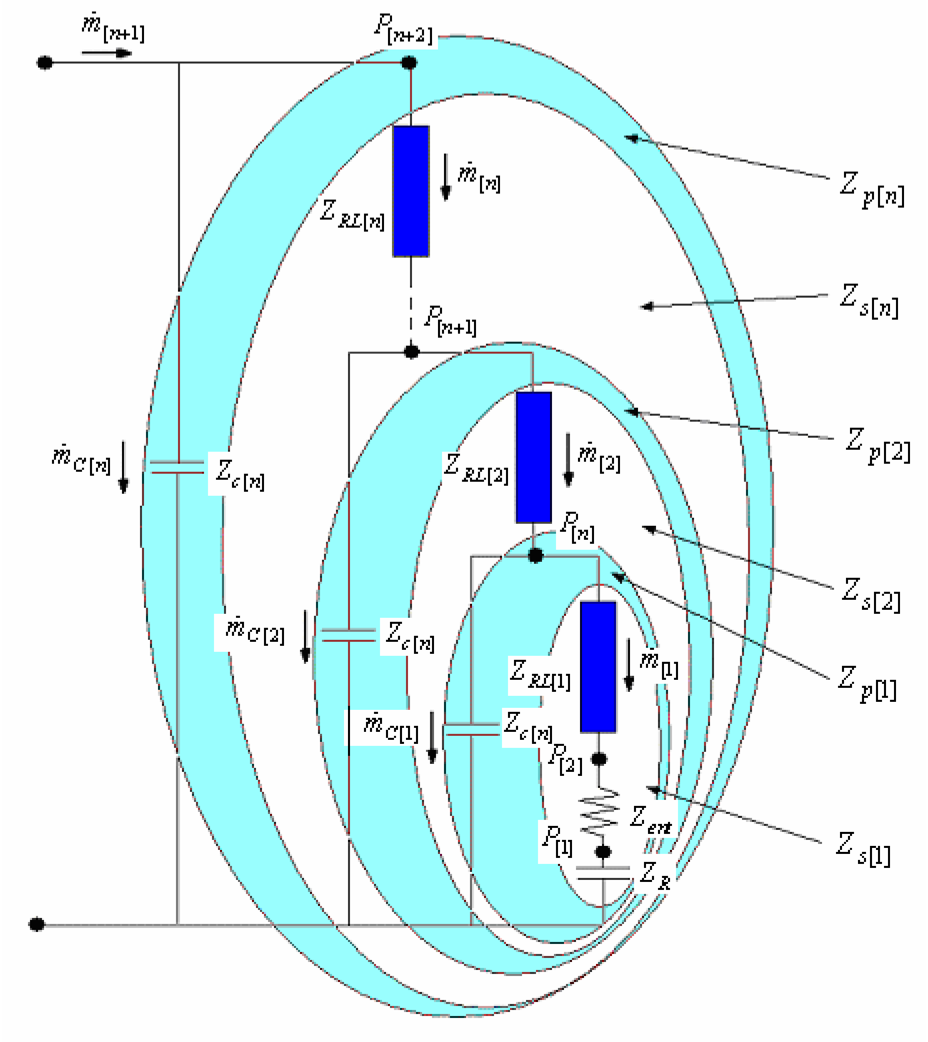

Figure 2.4 Distributed component model with outlined components in series and in parallel.

The equations used to generate the EES code associated with this model are presented in the following section and are contained in Appendix C. Note that the only equations presented here are those that have not already been derived and discussed in previous sections.

The impedance of the compliance and inertance of any segment ($Z_{C,i}$, and $Z_{L,i}$) are given by equations (2.27), (2.28), respectively:

$$Z_{C,i} = \frac{1}{j\omega C / n} \tag{2.27}$$

$$Z_{L,i} = j\omega L / n \tag{2.28}$$

where ω is the operating frequency and n the number of increments used in the model. The resistance of any increment (R_i) is a function of the mass flow rate through that increment, as shown in equation (2.29).

$$Z_{R,i} = R_i = \frac{64 f_{r_i} \dot{m}_i \, L / n}{\pi^3 \overline{\rho} D^5} \tag{2.29}$$

Since the mass flow rate ($\dot{m}_i$) is not constant along the line, the resistance must be computed for each element. The variation in the mass flow also causes the Reynolds number to change and therefore leads to a different friction factor ($f_{r,i}$) in each element.

The resistance associated with contraction or expansion at the reservoir inlet can be significant in some conditions and is determined from the measured pressure drop and the associated mass flow rate into the reservoir, scaled by assuming orifice behavior. This resistance can subsequently be replaced in a design model through the use of an appropriate orifice equation with a reasonable discharge coefficient. The impedance of one increment of resistance and inertance lumped in series ($Z_{RL,i}$) is:

$$Z_{RL,i} = Z_{R,i} + Z_{L,i} \tag{2.30}$$

When the entire network is considered, it can be divided into discrete components of impedance that are connected in parallel and in series, as shown in Figure 2.4 and indicated by $Z_p[1]...Z_p[n]$ and $Z_S[1]...Z_S[n]$. These impedances in array notation are given by equations (2.31) and (2.32).

$$Z_{S[2]} = Z_{RL[2]} + Z_{P[1]}, \qquad Z_{S[3]} = Z_{RL[3]} + Z_{P[2]} \,\ldots\ldots\ldots\, Z_{S[n]} = Z_{RL[n]} + Z_{P[n-1]} \tag{2.31}$$

$$\frac{1}{Z_{P[1]}} = \frac{1}{Z_{C[n]}} + \frac{1}{Z_{S[1]}}, \qquad \frac{1}{Z_{P[2]}} = \frac{1}{Z_{C[n]}} + \frac{1}{Z_{S[2]}} \,\ldots\ldots\ldots\, \frac{1}{Z_{P[n]}} = \frac{1}{Z_{C[n]}} + \frac{1}{Z_{S[n]}} \tag{2.32}$$

The first impedance in series is dependent on the resistance of the reservoir inlet and the reservoir compliance, as shown in equation (2.33).

$$Z_{s[1]} = Z_{ent} + Z_r + Z_{C[n]} \tag{2.33}$$

The total impedance of the network Z is the same as the n'th impedance in parallel ($Z_{p[n]}$). The mass flow rate at the inertance tube entrance ($\dot{m}_{[n+1]}$) is calculated based on the ratio of the pressure amplitude ($\tilde{P}_{[n+2]}$) at the inertance tube inlet (also written as $\tilde{P}$ in previous sections) over the magnitude of the total impedance (Z):

$$\dot{m}_{[n+1]} = \frac{\tilde{P}_{[n+2]}}{|Z|} \tag{2.34}$$

The mass flow and pressure at any position along the inertance tube can be determined using Kirchhoff's Law and the ratios of the pressure drops along the line over the corresponding impedances. Array notation is used again and the mass flows through the resistive and inertance elements are:

$$\dot{m}_{[1]} = \frac{\tilde{P}_{[3]} - \tilde{P}_{[2]}}{Z_{RL[1]}}, \qquad \dot{m}_{[2]} = \frac{\tilde{P}_{[4]} - \tilde{P}_{[3]}}{Z_{RL[2]}} \ldots\ldots\ldots \dot{m}_{[n]} = \frac{\tilde{P}_{[n+2]} - \tilde{P}_{[n+1]}}{Z_{RL[n]}} \tag{2.35}$$

The mass flow rate into the reservoir ($\dot{m}_{[1]}$) is also calculated (to provide enough equations for the number of unknowns) using the pressure variation immediately before the reservoir ($\tilde{P}_{[1]}$) and the capacitive impedance of the reservoir:

$$\dot{m}_{[1]} = \frac{\tilde{P}_{[1]}}{Z_r} \tag{2.36}$$

Another equation describing the mass flow into the reservoir in terms of the pressure drop across the reservoir's entrance resistance (Z_{ent}) is:

$$\dot{m}_{[1]} = \frac{\tilde{P}_{[2]} - \tilde{P}_{[1]}}{Z_{ent}} \tag{2.37}$$

The mass flows through the compliance elements of the line ($\dot{m}_{com[i]}$ through the $Z_{C[i]}$ elements) represent the mass that is stored in the inertance tube and are calculated according to equation (2.38).

$$\dot{m}_{C[1]} = \frac{\tilde{P}_{[3]}}{Z_{C[n]}}, \quad \dot{m}_{C[2]} = \frac{\tilde{P}_{[4]}}{Z_{C[n]}} \ldots\ldots\ldots \dot{m}_{C[n]} = \frac{\tilde{P}_{[n+2]}}{Z_{C[n]}} \tag{2.38}$$

Kirchhoff's Law applied at the nodes where the compliance elements of the tube are coupled with the resistive and inertance elements of the tube in series provides the necessary additional equations required.

$$\dot{m}_{[2]} = \dot{m}_{[1]} - \dot{m}_{C[1]}, \quad \dot{m}_{[3]} = \dot{m}_{[2]} - \dot{m}_{C[2]} \ldots\ldots\ldots \dot{m}_{[n+1]} = \dot{m}_{[n]} - \dot{m}_{C[n]} \tag{2.39}$$

3 HEAT EXCHANGER MODEL AND DESIGN

A compact heat exchanger (HX) is needed to cool the helium gas that exits the compressor at about 320 K before it enters the inertance tube. The cooling medium is water that enters the HX at about 285 K. The surface area on the helium-side is increased using wire screens and the surface on the water-side is augmented with fins. Due to cost constraints, the size and mesh of the screens and the nominal size of the fins were primarily dictated by the material that was on hand from previous experiments. Therefore, in order to design the heat exchanger for the inertance tube experiment, all that remained was to specify the length of the HX and the configuration of the fins for a given set of operating conditions, heat load, and all other geometric parameters. Figure 3.1 shows the basic heat exchanger design and indicates the geometry notation that will be used in later sections.

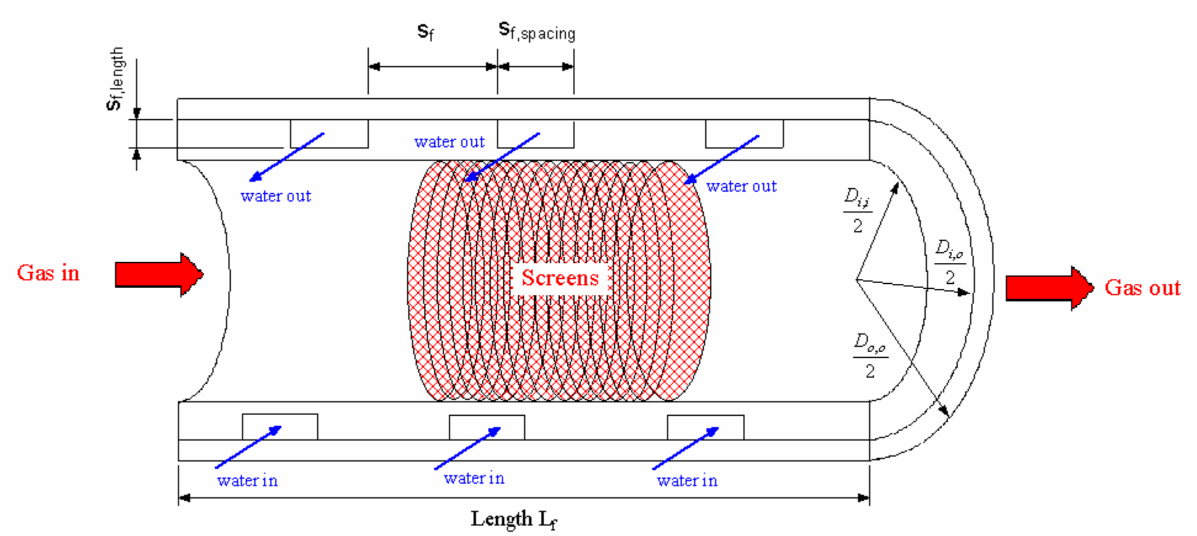

Figure 3.1 Basic heat exchanger design

3.1 Heat exchanger model

3.1.1 Effectiveness NTU-Method

The heat exchanger analysis is based on the effectiveness-NTU method. The number of transfer units (*NTU*) is defined as the ratio of the overall conductance between the helium and the water (*UA*) to the minimum heat capacity rate (C_{min}, either the heat capacity of water or the heat capacity of helium).

$$NTU = \frac{UA}{C_{\min}} \tag{3.1}$$

For a counter-flow arrangement, the required number of transfer units may be expressed in terms of the heat exchanger effectiveness (ε) and the heat capacity ratio (C_r).

$$C_r = \frac{C_{\min}}{C_{\max}} \tag{3.2}$$

$$NTU = \frac{1}{C_r - 1} \ln\left(\frac{\varepsilon - 1}{\varepsilon C_r - 1}\right) \qquad \text{for } C_r < 1 \tag{3.3}$$

$$NTU = \frac{\varepsilon}{1-\varepsilon} \qquad \text{for } C_r = 1$$

The effectiveness is defined as the ratio of the actual heat transfer rate across the HX to the maximum possible heat transfer rate. It is calculated in terms of temperatures and heat capacity rates according to:

$$\varepsilon = C_{He}\left(\frac{T_{He,i} - T_{He,o}}{C_{\min}\left(T_{He,i} - T_{W,i}\right)}\right) \tag{3.4}$$

$$C_{He} = \dot{m}_{He} cp,_{He} \tag{3.5}$$

where C_{He} is the heat capacity rate of helium, $\dot{m}_{He}$ is the mass flow rate of helium and $cp_{,He}$ its heat capacity. Indices *He, W, o,* and *i* indicate helium, water, outlet, and inlet, respectively.

3.1.2 Procedure to determine the HX surface area

A desired helium gas outlet temperature ($T_{He,o}$= 295 K) determines a heat exchanger effectiveness according to Eq. (3.4). The heat capacity rates that are used in Eq. (3.4) are given by experimental operating conditions; the helium inlet temperature ($T_{He,i}$) is determined based on an energy balance, Eqs. (3.6), and (3.7), using the heat exchanger load ($\dot{Q}_{rem}$) which is set to equal the maximum compressor power output (about 2kW):

$$\dot{Q}_{He} = \dot{Q}_{rem} \tag{3.6}$$

$$\dot{Q}_{He} = \dot{m}_{He} cp_{He} \left(T_{He,i} - T_{He,o} \right) \tag{3.7}$$

where $\dot{Q}$ indicates the heat transfer rate. The heat exchanger effectiveness together with the heat capacity ratio define a NTU-number according to equation (3.2). Using this NTU-number together with the minimum heat capacity in Eq. (3.1) gives the required heat exchanger conductance (*UA*). The geometry of the fins and size of the screens as well as the operating conditions are known a-priori and are listed in Table 3.1. Therefore, the conductance uniquely determines the heat exchanger length, as presented in the following sections.

Table 3.1 Operating conditions

Screens	Material	Mesh	Wire Dia.	Hydraulic Dia.	Spacing	Porosity
	Copper	100	114.3µm	209.1µm	254.0µm	0.647
Inner tube with fins	Material	Inner Dia.	Outer Dia.	Fin thickness	Fin length	Fin spacing
	Brass	50.8mm	63.4mm	3.05mm	2.03mm	3.05mm
Other	Water temperature inlet			Heat removal rate		
	285K			2kW		
	Mass flow helium			Mass flow water		
	0.02kg/s			2gallon/min		

3.1.3 Fluid properties

Fluid properties are necessary in order to carry out the subsequent heat transfer calculations. Density, viscosity, conductivity, and the Prandtl Number are obtained with build-in functions in EES for the helium and the water at their mean temperature and the mean compressor charge pressure. The conductivity of the wall material (brass) is determined at the average of the helium and water mean temperature.

3.1.4 Reynolds number

The Reynolds (Re) number is defined as $Re=v\ d_h\ \rho/\mu$ where v is velocity, d_h is the hydraulic diameter, ρ is the density, and μ is the viscosity. For the water flow in the fin passages, the hydraulic diameter is four times the cross-sectional area of the passage over its wetted perimeter. The hydraulic diameter of the fin passage ($d_{h,f}$) is given by equation (3.8) and the Reynolds number of the water flow (Re_w) by equation (3.9),

$$d_{h,f} = 4 s_{f,spacing} \left(\frac{s_{f,length}}{2 s_{f,spacing} + 2 s_{f,length}} \right) \tag{3.8}$$

$$\mathrm{Re}_W = d_{h,f}\, v_W \frac{\rho_W}{\mu_W} \tag{3.9}$$

where $s_{f,length}$ is the fin length, $s_{f,spacing}$ is the spacing between the fins (see Figure 3.1), and v_W is the bulk velocity of the water in the passages. The bulk velocity is determined assuming a total flow rate of 3.6 liters per minute (consistent with using house water) and the cross-sectional area of one fin passage. This implies that the fin passages will be headered so that the flow is in series rather than in parallel.

The Reynolds number for the helium flow ($\mathrm{Re}_{screens}$) is expressed in terms of a mass velocity (*G*), the porosity of the screens (*p*), the screen hydraulic diameter ($d_{h,s}$), and the screen frontal area (A_{fr}). Porosity and hydraulic diameter are obtained from the manufacturer's specification sheets (Table 3.1). The frontal area is the cross-sectional area of the inner tube of the HX ($d^2_{i,i}\,\pi/4$). The mass velocity is calculated according to [12],

$$G = \frac{\dot{m}_{He}}{pA_{fr}} \tag{3.10}$$

and the Reynolds number is given by Eq. (3.11).

$$\mathrm{Re}_{screens} = G\frac{d_{h,s}}{\mu_{He}} \tag{3.11}$$

3.1.5 The water-side heat transfer coefficient

The convection coefficient between the water and the surface of the fins (h_f) is determined using a Nusselt correlation for turbulent flow in tubes according to Petukhov [9]. The friction factor (f_r) that is required for the Nusselt correlation is calculated according to equation (3.12), assuming smooth fin channels.

$$f_r = 1.84\left(\mathrm{Re}_W\right)^{-0.2} \tag{3.12}$$

This equation is valid for Reynolds numbers greater than 20,000. The Reynolds number in the fin passage is about 59,000. The Nusselt number (Nu_f) is given by equation (3.13).

$$Nu_f = \frac{0.125\,\mathrm{Re}_f\,\mathrm{Pr}_W}{1+12.7\left(\frac{f_r}{8}\right)^{0.5}\left(\mathrm{Pr}_W{}^{2/3}-1\right)} \tag{3.13}$$

3.1.6 Helium-side heat transfer coefficient

A correlation for the Colburn factor (j) for steady flow over screens is used to determine the heat transfer coefficient ($h_{screens}$) between the helium gas and the screen matrix. The relationship between j and $Re_{screens}$ is expressed in figures in Kays and London [12]. The heat transfer coefficient is related to the Colburn factor according to:

$$j = \frac{h_{screens}}{Gcp_{He}}\mathrm{Pr}_{He}{}^{(2/3)} \tag{3.14}$$

3.1.7 Heat exchanger areas

This section provides equations for HX surface areas that are used to compute the conductance. The total surface area exposed to water ($A_{f,t}$) is the sum of the fin surface area ($A_{f,o}$) and the fin base area ($A_{f,b}$):

$$A_{f,o} = 2\pi N_f \left(D_{i,o}{}^2 - \left(D_{i,o} - 2s_{f,length} \right)^2 \right) \tag{3.15}$$

$$A_{f,b} = \pi s_{f,spacing} N_f \left(D_{i,o} - 2s_{f,length} \right) \tag{3.16}$$

$$A_{f,t} = A_{f,b} + A_{f,o} \tag{3.17}$$

$$N_f = \frac{L}{s_{spacing} + s_f} \tag{3.18}$$

where N_f is the number of fins, L the heat exchanger length, and the remaining variables are diameters and fin spacing dimensions shown in Figure 3.1.

The surface area of the screens ($A_{screens}$) is the product of the screen volume and the specific surface area α. The specific surface area for square-mesh crossed-rod matrices is given by [12]:

$$\alpha = \frac{\pi}{s_w} \tag{3.19}$$

where s_w represents the spacing between the screen wires. The surface area for heat transfer is given by equation (3.20).

$$A_{screens} = A_{fr} L \alpha \tag{3.20}$$

3.1.8 Fin efficiencies

There is a radial temperature variation in both the water-side fins and the screens on the helium-side due to conduction; this makes the surface area less effective at exchanging heat than it would be for an infinitely conductive solid. This effect is accounted for using fin efficiencies for both sides. The overall finned surface efficiency (η_0) is a function of the fin efficiency (η_f), the total heat transfer area, and the total fin area.

The fin efficiency of the annular fins on the water side is:

$$\eta_{f,f} = C_2 \frac{K_1(m_f r_{f,i}) I_1(m_f r_{f,c}) - I_1(m_f r_{f,i}) K_1(m_f r_{f,c})}{I_0(m_f r_{f,i}) K_1(m_f r_{f,c}) - K_0(m_f r_{f,i}) I_1(m_f r_{f,c})} \tag{3.21}$$

$$C_2 = \frac{2 r_{f,i}}{m_f ({r_{f,o}}^2 - {r_{f,i}}^2)} \tag{3.22}$$

$$m_f = \sqrt{\frac{2h}{k\delta}} \tag{3.23}$$

where I_0 and K_0 are modified, zero order Bessel functions of the first and second kinds, respectively, I_1 and K_1 are modified, first order Bessel functions of the first and second kinds, respectively, C_2 and m_f are given by equations (3.22) and (3.24), respectively, $r_{f,i}$ is the fin inner radius, $r_{f,o}$ is the fin outer radius, and $r_{f,c}$ is the sum of the fin outer radius and half the fin thickness. The overall fin efficiency ($\eta_{0,f}$) for the fins on the water-side is determined by Eq. (3.24).

$$\eta_{0,f} = 1 - \frac{A_{f,o}}{A_{f,t}}\left(1 - \eta_{f,f}\right) \tag{3.24}$$

The screens are treated as an array of pin fins to obtain the screen efficiency. Each screen wire is assumed to behave like a pin fin. Since all wires of one screen are of different length, a mean wire (pin) length is specified. Therefore, the annular screen is approximated with a square of equal area, Figure (3.2).

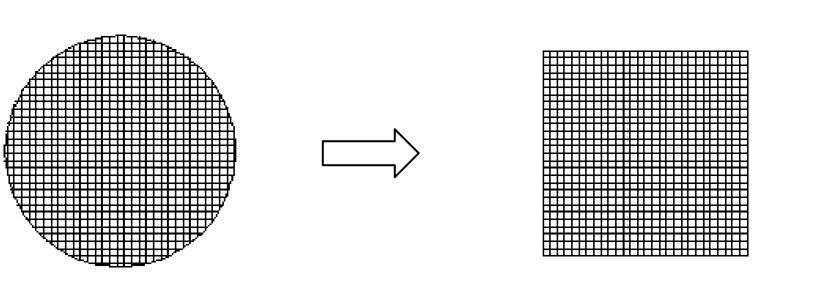

Figure 3.2 Equivalent square screen area.

Assuming that the wires are straight, the pin length ($L_{s,u}$) is half the side length of the square screen. Since the wires are plaited, the real pin length $L_{s,r}$ is the product of $L_{s,u}$ and a correction factor f_{pin} that accounts for the wires not being perfectly straight. This correction factor is determined graphically from Figure 3.3 and is found to be 1.11.

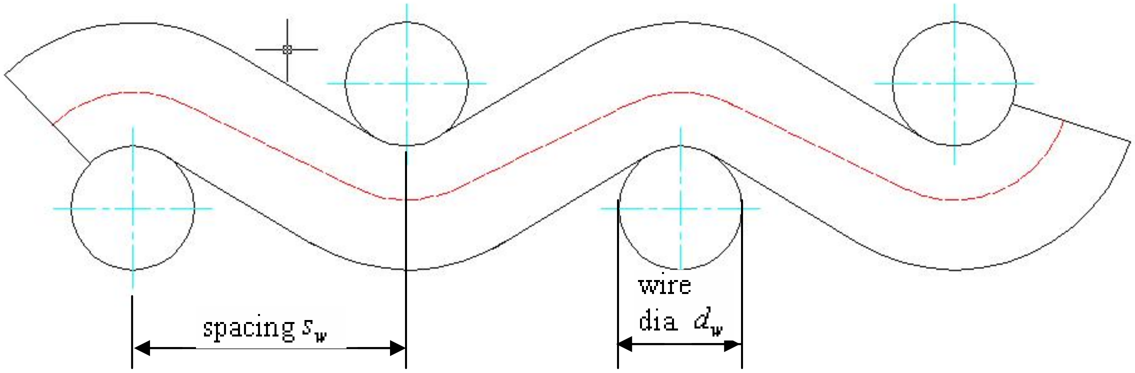

Figure 3.3 Screen mesh

The pin efficiency (screen efficiency) is determined according to:

$$\eta_{f,screen} = \frac{\tanh\left(m_{screen} L_{s,c}\right)}{m_{screen} L_{s,c}} \tag{2.25}$$

where the corrected pin length $L_{s,c}$ is determined according to Eq. (3.26), and the dimensionless factor $m_{screens}$ for pin fins is calculated with Eq. (3.27).

$$L_{s,c} = L_{s,r} + d_w / 4 \tag{3.26}$$

$$m_{screens} = \sqrt{\frac{4 h_{screens}}{k_{screens} d_w}} \tag{3.27}$$

The overall fin efficiency for the screens ($\eta_{0,screens}$) is the fin efficiency of the screens (Eq. 3.21) since the ratio of total fin area to the total heat transfer area is assumed to be unity as there is little base area available (i.e. we are assuming nearly perfect stacking of the screens).

3.1.9 Wall resistance

The resistance associated with heat conduction through the wall that separates the fins from the screens is obtained in terms of a geometry factor (F_f^*) for circular pipes and the thermal conductivity of the pipe material, which is copper.

$$F_f^* = 2\pi L \left(\ln \frac{r_{f,o}}{r_{f,i}} \right)^{-1} \tag{3.25}$$

3.1.10 Total conductance

The total heat conductance can be calculated by equation (3.26) with the coefficients introduced in the previous sections.

$$\frac{1}{UA} = \frac{1}{h_f \eta_{0,f} A_{f,t}} + \frac{1}{k F_f^*} + \frac{1}{h_{screens} A_{screens} \eta_{0,screens}} \tag{3.26}$$

3.1.11 HX length

The required heat exchanger length can be obtained from combining equations (3.1) and (3.26) where equation (3.1) is solved for the product of the total heat transfer coefficient and the surface area of the fins on the water-side. Solving the set of heat exchanger equations with the known operating conditions and the constrained geometry results in a HX length of 56 mm. The EES code used to implement the HX model is contained in Appendix D.

3.2 Heat exchanger design

This section briefly describes the heat exchanger design. The design had to be simple so that it could be fabricated in the machine shop of the Cryogenics Lab at the University of Wisconsin. The subsequent figures show CAD drawings of the heat exchanger.

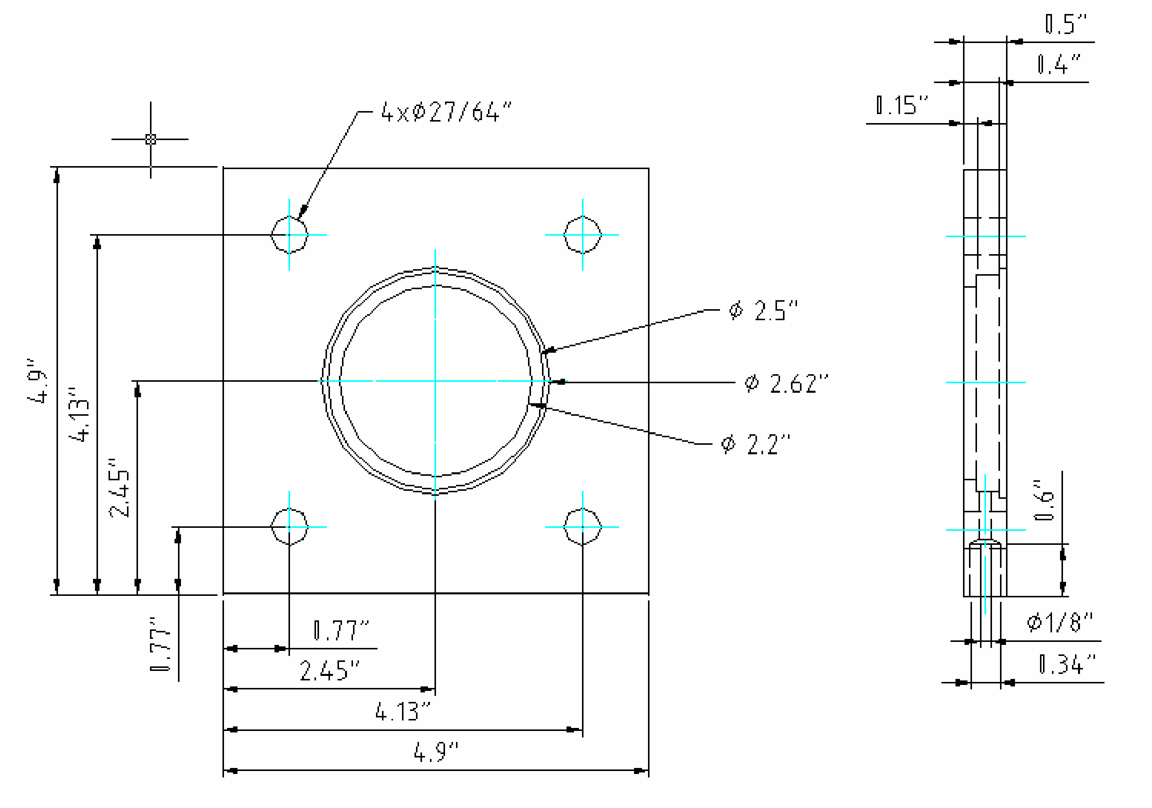

Figure 3.4 Flange detailed drawing.

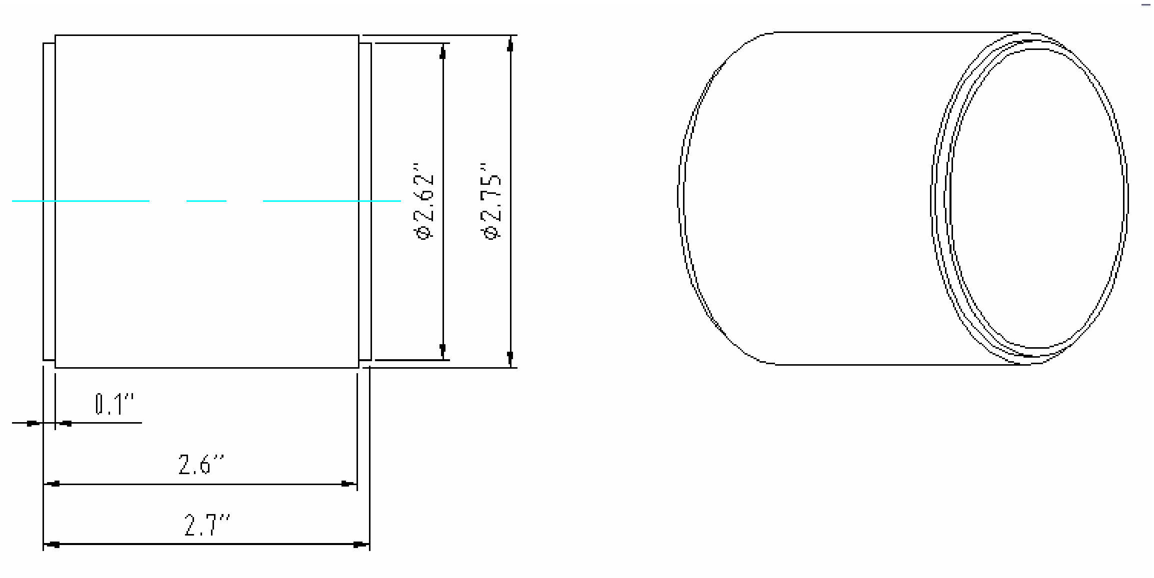

Figure 3.5 Outer tube detailed drawing.

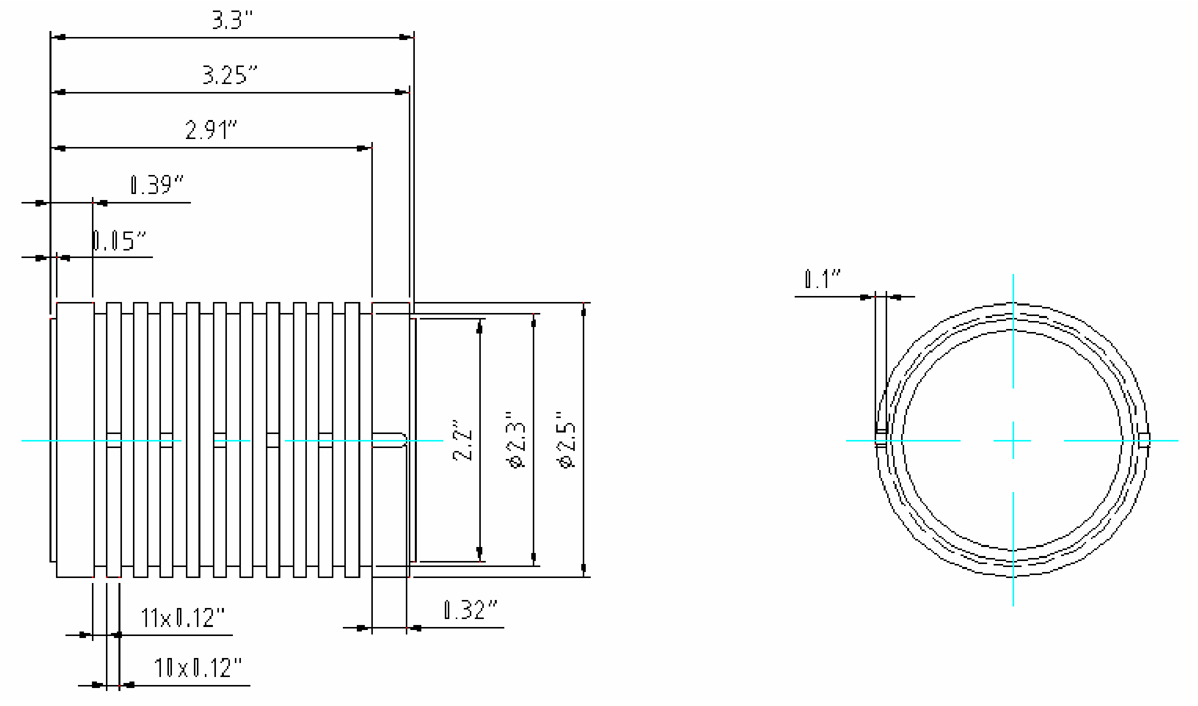

Figure 3.6 Inner tube detailed drawing.

The inner tube is made of bronze and the fins are lathe-cut into the inner tube's shell (Figure 3.1 and Figure 3.6). The fins are connected with mill-cut grooves to allow the water flowing from one fin to the other. The water enters and exits the fins via flanges (Figure 3.4) that are placed on either side of the HX. The outer (Figure 3.5) tube provides a housing for the HX, and the flanges connect the HX with the compressor crankcase and the compressor head. The completely assembled heat exchanger with screens is presented in Figure 3.7.

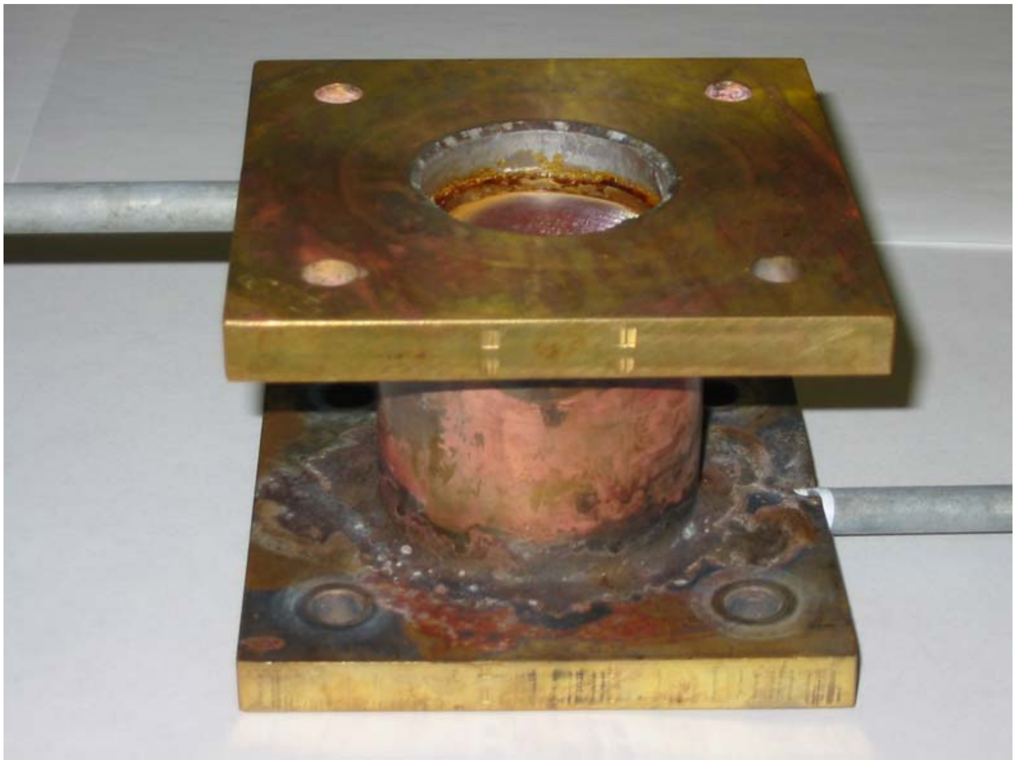

Figure 3.7 Assembled heat exchanger with screens

4 MASS FLOW MEASUREMENTS

The models introduced in chapter 2 can be verified most directly if the time varying mass flow rate and pressure at the inertance tube inlet are measured. These measurements would allow the impedance and phase associated with the inertance tube to be determined. This chapter describes several attempts that were made to measure the oscillating mass flow rate at the inertance tube inlet. The next section presents a description of the basic experimental setup to identify the locations at which the mass flow and pressure are measured in the experiments.

4.1 Basic experimental setup

The basic experimental setup is presented in this chapter. Ju et al. suggested that no pulse tube is necessary in order to measure the inertance effect associated with inertance tubes because they typically operate at or near room temperature [13]. The acoustic power of the driving compressor is then transferred directly to the inertance tube and the experimental setup is very simple. Because the single function of the inertance tube is to modify the phase between the mass flow and pressure in the pulse tube, the primary measurements of interest are the time dependent pressure and mass flow rates at the inlet (the compressor end) of the inertance tube. Thus, the most straightforward measurement approach is to provide one mass flow meter and pressure sensor at the inlet of the inertance tube to determine the phase shift between pressure and the mass flow rate at this location. The mass flow rate into the reservoir can be indirectly calculated based on continuity with an additional pressure sensor in the reservoir, as described in later chapters. The heat exchanger described in the previous chapter cools the gas leaving the compressor in order to keep the gas inside the inertance tube and reservoir close to room temperature. The basic experimental setup is shown in Figure 4.1.

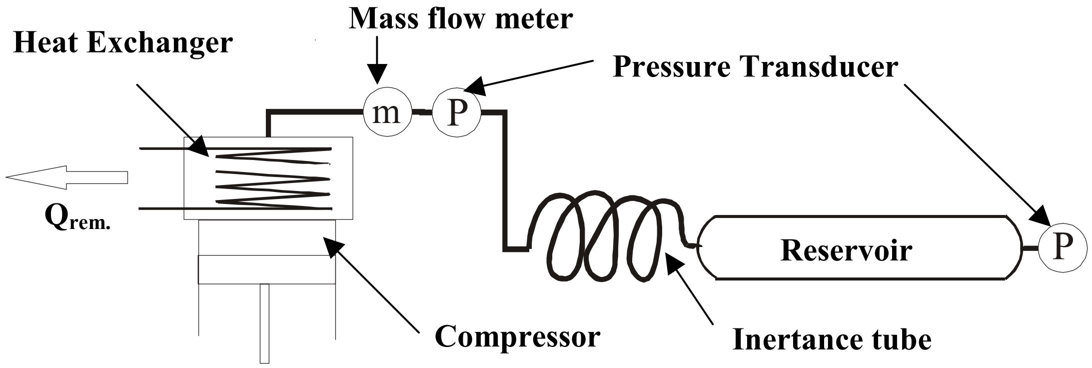

Figure 4.1 Basic experimental setup

4.1.1 Equipment for the experimental setup

This section describes the equipment used in the experiments that are described in this and Chapter 5. The driving compressor is a Corken, model D91, single piston compressor with a swept volume of 0.29 liters, an operating frequency of 400 rpm (6.67 Hz) to 825 rpm (13.75 Hz), a maximum pressure of 350 psia (24.14 bars), and a nominal acoustic power of approximately 2 kW.

The inertance tubes attached to the compressor outlet are copper refrigeration tubes ranging from 5 feet (1.524 m) to 50 feet (15.24 m). Their outer diameters are 1/4 inch (inner diameter, ID, 0.19"), 3/8 inch (0.311" ID), and 1/2 inch (0.436" ID).

The reservoirs attached to the reservoir end of the inertance tube are stainless steel cylinders with either 1 or 2 gallon volume.

The Sensirion mass flow sensor, model ASF 1430, (presented later in this chapter), has a response time of 5 ms, a range from -440sccm to 440 sccm (standard cubic centimeters per minute), an over pressure resistance of 2 bars, and an accuracy of 1%.

The mass flow meter used to calibrate the Sensirion sensor for helium is an Aalborg, model GFM 673, mass flow meter with a range of 0 to 500 sclm (standard liters per minute), a maximum operating pressure of 500 psig (34.5 bars), an uncertainty of $\pm 1.5\%$ of full scale.

The voltmeter used to measure the output voltage of the Aalborg mass flow is a Hewlett Packard digital multimeter, model 34401A; its accuracy is 0.0015% of full scale.

The pressure transducers used to measure the pressure in the compression space, in the inertance tube, and in the reservoir are Endevco pressure transducers, model 8510B-55; their range is from 0 to 500 psig (34.5 bars), their response time is 0.005 ms, and their sensitivity is 0.6 ± 0.2 mV per psi.

The output voltage (0-300 mV) of the pressure transducers is acquired with a National Instrument data acquisition device, model 6034E; its sampling rate is 200 kHz and the absolute accuracy at an input of -0.5 to0.5 V is 0.448 mV.

The remainder of this chapter describes different methods that were investigated and/or applied in an attempt to measure the oscillating mass flow rate at the compressor exit.

4.2 Laminar flow meter

Laminar flow elements have been widely used for measuring steady mass flow rates due to their simplicity and acceptable accuracy. However, under high frequency, oscillating flow conditions the laminar flow element introduces resistive capacitive, and inertial impedances. This can lead to overestimating the flow amplitude by a factor of 1.1-1.6 and can lead to an error in phase of $20^{\circ}-60^{\circ}$ [7]. Therefore, the use of a laminar flow meter was not considered further for this project.

4.3 Hot film anemometry

Hot film or hot wire anemometers are capable of accurately measuring oscillating mass flow rates at high frequencies. The anticipated compressor operating frequency for the experimental apparatus is 10.81 Hz and the average operating pressure is 10 bar; these constraints are related to the compressor. The resulting maximum mass flow rate of the compressor under these conditions is about 15 g/s. Unfortunately there is no hot film anemometer commercially available that is capable of measuring mass flow rate at this combination of high pressure, frequency, and flow. After a vendor search, the most relevant commercially available hot film anemometer was identified. The unit is model ASF 1430 manufactured by Sensirion and its specifications are described in the previous section.

4.3.1 Sensirion hot film mass flow sensor model ASF 1430

The Sensirion hot film mass flow sensor model ASF 1430 has a response time of 5 ms; its range is from -440 to +440 sccm (standard cubic centimeter per minute) and its overpressure resistance is 2 bars with respect to ambient. Therefore, the ASF 1430 specifications suggest that the sensor meets the experimental requirements for response time but not range and operating pressure. However, the ASF 1430 can satisfy all three requirements after a few modifications are applied. Figure 4.2 shows the sensor with the housing cap removed.

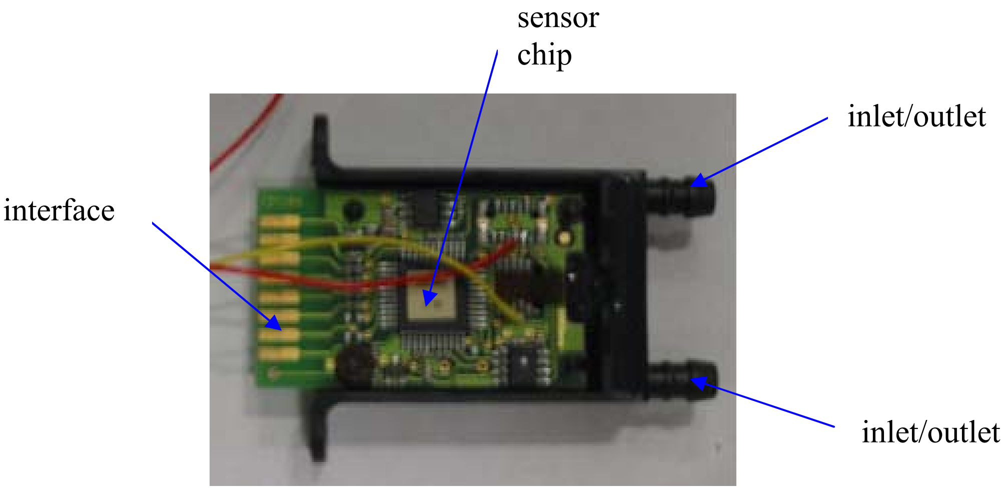

Figure 4.2 Sensirion mass flow sensor with the housing cap removed

4.3.1.1 Overpressure and flow range modification

In order to make the mass flow sensor robust to the pressures that are expected in the inertance tube experiment, the entire sensor is placed in a hermetic pressure case that is pressurized to the mean operating pressure (10 bars). In order to increase the range of the sensor, only a small portion of the flow to be measured is passed through the sensor. The remainder of the gas passes through the bypass tube, as shown in the schematic presented in Figure 4.3.

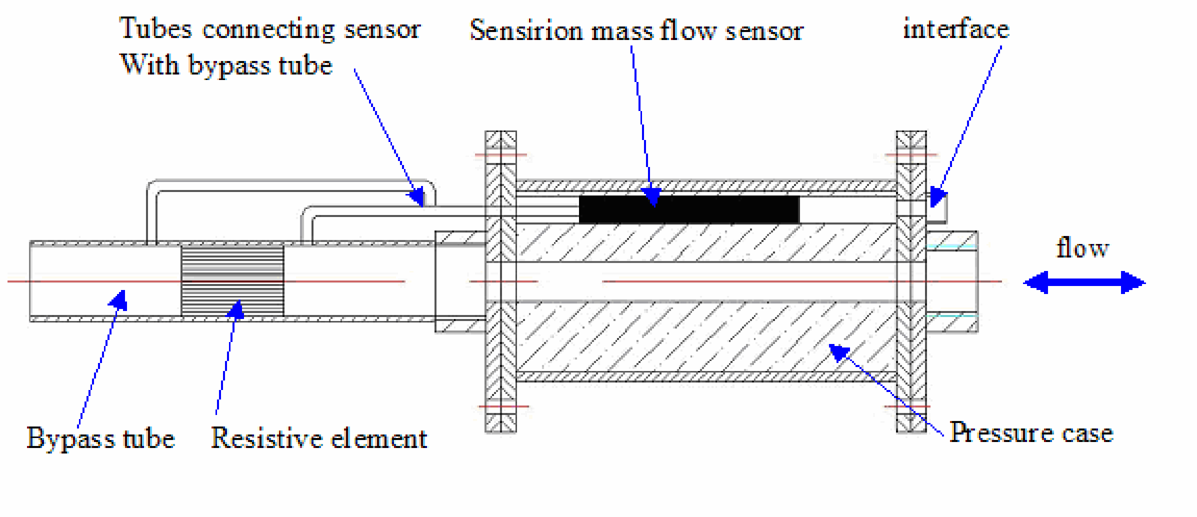

Figure 4.3 Sensirion mass flow meter packaged for operation at high pressure and interfaced with a bypass tube to increase its flow range

The internal volume of the sensor and the external volume (its plastic housing) are both exposed to the charge pressure, making the pressure difference between any parts of the sensor near zero even as it operates at the elevated pressure. Since the method of measuring mass flow rates with a hot film anemometer is nearly independent of pressure, the sensor in the casing can operate to the burst pressure of the casing. The range of the sensor can be conveniently adjusted by inserting resistive elements, such as honeycombs, into the bypass tube. The higher the pressure drop across the honeycomb, the higher is the flow through the tubes connecting the sensor with the bypass tube. Figure 4.4 shows the packaged Sensirion mass flow sensor.

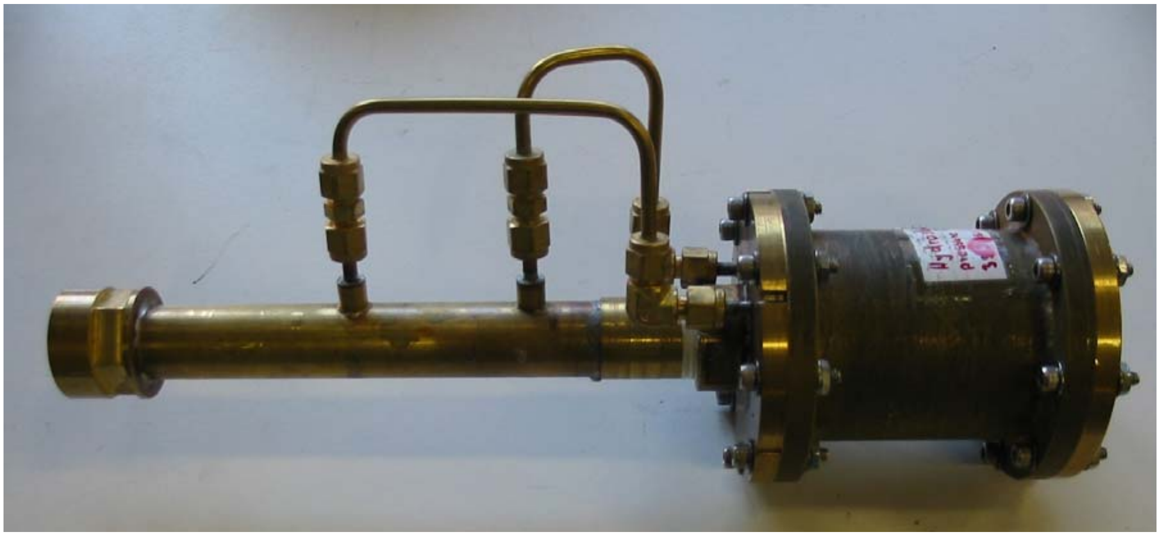

Figure 4.4 Packaged Sensirion mass flow sensor

4.3.1.2 Calibration of the Sensirion mass flow sensor in the pressure case

The presence of the bypass tube makes it imperative to calibrate the mass flow sensor prior to its use. It would be prudent to do this in any case. The mass flow sensor is calibrated using a steady helium flow and a calorimetric reference flow meter with a range of 500 sclm (standard cubic liter per minute). Two pressure transducers are used to measure the total pressure drop across the series connection of the packaged Sensirion mass flow sensor and the reference flow meter. Figure 4.5 shows the calibration setup.

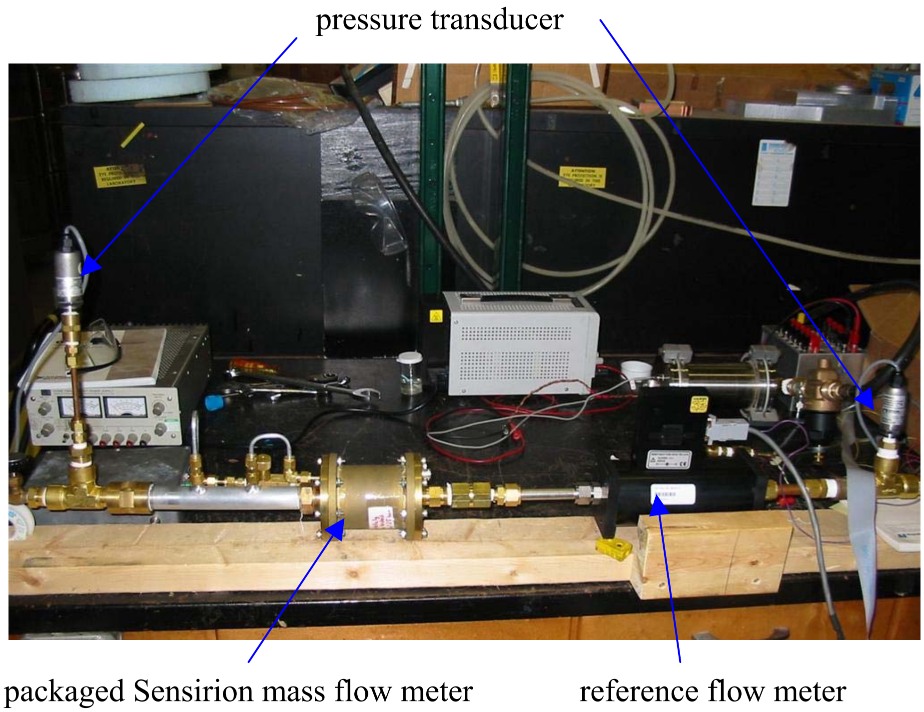

Figure 4.5 Calibration setup

The sensor was calibrated at 5 and 10 bars with helium flow rates of up to 500 sclm. Figure 4.5 shows the sensor output (in sccm) as a function of the reference flow meter output in sclm.

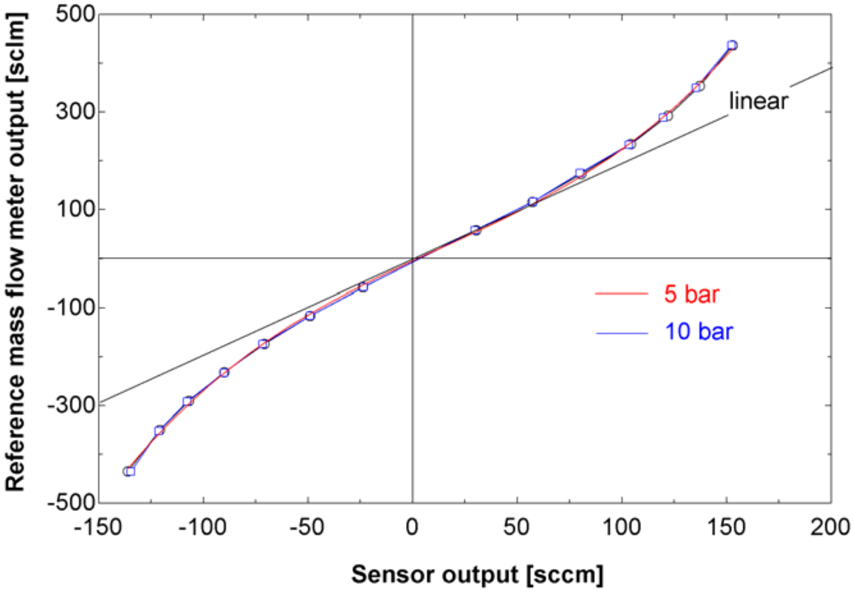

Figure 4.6 C Calibration curve for the packaged Sensirion mass flow sensor

As expected, the Sensirion sensor is found to be insensitive to operating pressure. In order to describe a function that converts the sensor's reading into a mass flow rate (kg/s), a third order polynomial curve fit (Eq. 4.2) was determined for the calibration curve presented in Figure 4.6. The reference flow meter is calibrated for use with nitrogen by the manufacturer and scales directly with the true mass flow at standard conditions (101.325 kPa, 15 deg C), i.e. its output is proportional to the heat capacity rate at standard conditions ($\dot{m} c_P$). In order to obtain the mass flow rate of helium through the reference flow meter, it is necessary to scale by the ratio of the specific heat capacity of nitrogen to the specific heat capacity of helium, as shown in Eq. (4.1)

$$\dot{m}_{N2} c_{P,N2} = \dot{m}_{He} c_{P,He} \tag{4.1}$$

The indices *N2* and *He* denote nitrogen and helium, respectively. The final calibration curve for the mass flow sensor is given by Eq. (4.2),

$$\dot{m}_{He} = \rho_{N2,std} \frac{cp_{N2,std}}{cp_{He}} \left(8.01*10^{-5} - 3.31*10^{-5} out + 2.92*10^{-8} out^2 - 8.03*10^{-10} out^3 \right) \quad (4.2)$$

where "out" is the sensor's output in sccm, all other units are in SI units. Note that the sensor is interfaced with the data acquisition system through its own, manufacturer supplied sub-program that converts the sensor’s digital output to flow rate, in sccm.

4.3.1.3 Preliminary testing with an inertance tube

The packaged mass flow sensor (i.e., the sensor installed in the pressure case and interfaced with a bypass tube) is attached to the compressor head and the outlet of the sensor is connected to an inertance tube in order to examine its behavior under oscillating flow conditions. (Note, in following sections the sensor installed in the pressure case an interface and bypass tube will be referred to as "system"). Figure 4.7 shows the mass flow rate and pressure measured using an operating frequency of 6.3 Hz with a 6 feet, 1/2" OD inertance tube with a wall thickness of 0.032" and a 3.4 liter reservoir.

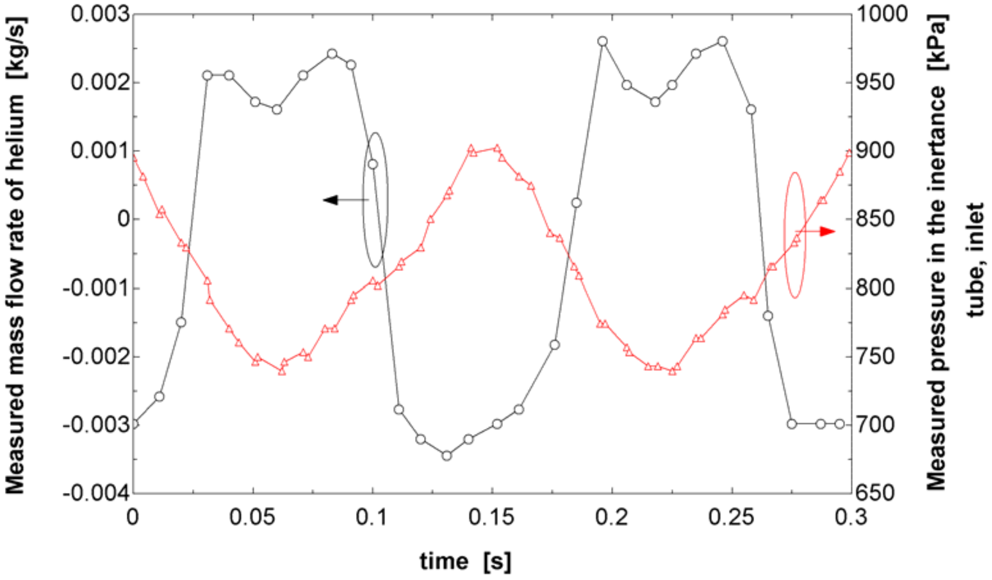

Figure 4.7 Measured pressure and mass flow rate as a function of time at the inlet to the inertance tube under oscillating flow conditions

The pressure at the inlet to the inertance tube in Figure 4.7 shows a nearly sinusoidal behavior whereas the mass flow exhibits a ”chopped” shape. The shape of the mass flow rate in Figure 4.7 puts in question the ability of the system to measure the true mass flow under these oscillating conditions, despite the manufacturer’s stated response time. Possibly the addition of the bypass tube added some fluid compliance and resistance that leads to undesirable dynamic effects. Therefore, the next section provides a method to test the validity of these measurements.

4.3.1.4 Validity check of the oscillating mass flow rate measurements

To check the validity of the packaged Sensirion mass flow rate sensor under oscillating flow conditions a test was carried out in which the outlet of the packaged sensor is capped. Ideally, the sensor should report zero mass flow rate in this condition since no mass is leaving the system. The calibrated sensor's reading is shown in Figure 4.8.

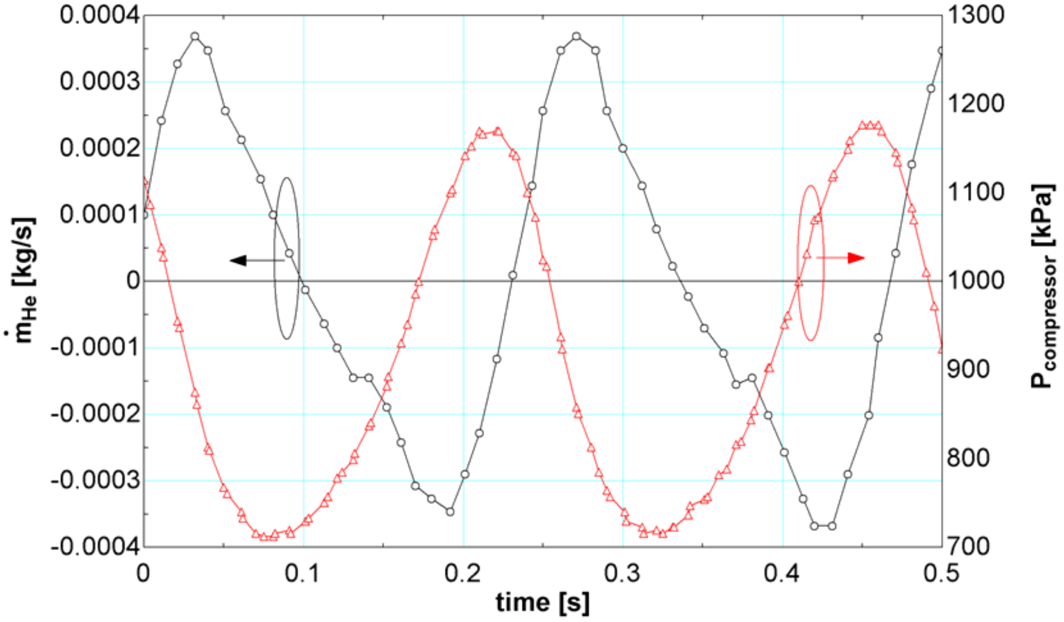

Figure 4.8 The packaged sensor's measured helium mass flow rate and the pressure in the compressor as a function of time under capped conditions

It can be seen from Figure 4.8 that the reported magnitude of the mass flow is about 11% of the mass flow magnitude shown in Figure 4.7 when an inertance is connected to the pressure case. Note that the operating frequency at which the validity check was conducted is only 4.2 Hz. . If the measured mass flow rate increases linearly with the compressor frequency then the magnitude of the mass flow rate at 10 Hz will be 0.00057 kg/s or about 15% of the mass flow magnitude shown in Figure 4.7. Defining the error of the mass flow measurement as the percentage fraction of the reported mass flow magnitude at plugged conditions compared to the mass flow magnitude when the inertance is connected (which neglects all other sources of uncertainty), the error in the mass flow rate measurement would be 15%.

The rather high error determined from this validity check and the questionable "chopped-off" sinusoid shown in Figure 4.7, prompted the consideration of a different method for measuring the mass flow rate at the inertance inlet.

4.4 The isothermal mass conservation method

An alternative to directly measuring the mass flow rate is described in this section. The indirect technique used in this case combines measurements of pressure and volume, along with the ideal gas law and the principle of mass conservation to calculate the mass flow rate. Assuming ideal gas behavior for the working gas (helium), the mass flow rate into the inertance tube is the first derivative of the sum of the total mass contained under the piston (referred to as volume 1), the volume between the piston and the heat exchanger (referred to as volume 2), the volume in the heat exchanger (referred to as volume 3), and the volume between the heat exchanger and the inertance tube (referred to as volume 4). The volume beneath the piston must be included in this calculation due to the large rate of leakage through the piston rings. The mass flow rate into the inertance tube is computed by differentiating the calculated contained mass in the four volumes (1-4) with respect to time.

$$\dot{m} = -\sum_{i=1}^{4} \frac{d}{dt}\left(\frac{P_i V_i}{RT_i}\right) \tag{4.1}$$

Assuming isothermal compression and thus neglecting the temperature derivative term, leads to:

$$\dot{m} = -\frac{1}{R\overline{T}}\frac{d}{dt}\left(V_1 P_1 + V_2 P_2 + V_3 P_3 + V_4 P_4\right) \tag{4.2}$$

where $\overline{T}$ is the average room temperature. Volumes 1 and 2 are changing with respect to time and therefore must be known as a function of time. A reed relay is mounted to the driving compressor pulley in order to measure the time at which the piston reaches its top dead center position. Using the signal from this relay and assuming sinusoidal piston motion, it is possible to determine the instantaneous values of volumes 1 and 2 with respect to time. The instantaneous pressures under the piston, above the piston, and above the HX are measured using Endevco pressure transducers. The pressure in the heat exchanger (P_3) is assumed to be the average of the pressures above and below the HX. The experimental setup is shown in Figure 4.9.

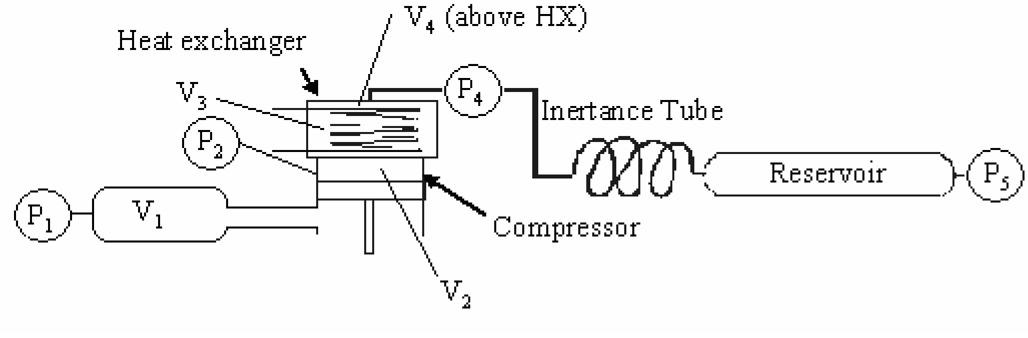

Figure 4.9 Experimental setup to measure the mass flow rate using the isothermal mass conservation method. Note that P denotes the location of a pressure transducer.

In order to estimate the uncertainty inherent in the assumption of isothermal compression, a simple error analysis was conducted. The largest errors are produced when the temperature excursions relative to their average values is largest which occurs for an adiabatic compression process. The maximum mass flow exiting the compressor is

$$\dot{m}_{\max} = \frac{V_{swept}\bar{P}}{R\bar{T}}\omega \tag{4.3}$$

where V_{swept} is the compressor's swept volume, $\bar{P}$ and $\bar{T}$ are the mean pressure and temperature, R is the specific gas constant of the operating gas, and ω is the operating frequency (in rad/s). The maximum error of the mass flow ($d\dot{m}$) is

$$d\dot{m} = \frac{V_{swept}\bar{P}\,\delta T}{R\,\bar{T}^2}\omega \tag{4.4}$$

where δT is the difference between the temperature at the conclusion of the adiabatic compression process temperature and the mean temperature:

$$\delta T = \bar{T}\left[\left(\frac{\bar{P}+\tilde{P}}{\bar{P}}\right)^{\left(\frac{\kappa-1}{\kappa}\right)} - 1\right] \tag{4.5}$$

$\tilde{P}$ is the pressure amplitude and κ the polytropic exponent (1.67 for adiabatic compression of helium). The maximum percent error is the ratio of the maximum error of the mass flow to the maximum mass flow:

$$error_{\dot{m}} = \frac{d\dot{m}}{\dot{m}_{\max}} * 100\% = \left[\left(\frac{\bar{P}+\tilde{P}}{\bar{P}}\right)^{\left(\frac{\kappa-1}{\kappa}\right)} - 1\right] * 100\% \tag{4.6}$$

For a typical operating condition (10 bar mean pressure a pressure amplitude of 1.5 bar), the maximum error according to this analysis is 5.8%.

To check the accuracy of the isothermal mass conservation method experimentally, the inertance tube is removed and a small volume (660 ml) is attached to the compressor outlet and included in the mass balance. The purpose of this small volume is to avoid a high pressure ratio that would otherwise occur in the system. Ideally, the measured contained mass in this case is constant. To account for errors arising from the assumption of isothermal compression, volume 1 is reduced by about 10% relative to its actual volume (0.97 liters) in order to minimize the variation of contained mass. At an operating frequency of 10.81 Hz, the contained mass is found to vary by 0.8%, equivalent to 0.03 g. Note that the small volume associated with this test resulted in a high pressure ratio, relative to what is typically found in a pulse tube, of 1.47.

When an inertance tube is connected, the contained mass oscillates by 0.15-0.30 g at 1.0 MPa. This value varies somewhat depending on the inertance tube size. The ratio of the uncertainty in the contained mass (0.03g) to its measured fluctuation during testing (0.15-0.30g) represents a maximum error in the mass flow rate measurement that is 10-20%. It should be noted that most measurements presented in the chapter 5 are obtained with lower pressure ratios (between 1.27-1.44 for the 7.9mm ID tube and between 1.12-1.28 for the 11.1mm tube), and therefore slightly smaller errors are likely for these data because of the lower temperature fluctuation, as indicated by Eq. (4.6).

4.5 The polytropic mass conservation method

Two additional issues associated with the indirect method of determining mass flow rates have been considered to further reduce discrepancies between the calculated and actual mass flow rates. These include approximating the piston movement according to the compressor's actual kinematics of the crank mechanism (as opposed to a sine wave) and replacing the isothermal assumption with the assumption that the compression process is polytropic.

An expression for the compressor's swept volume above the piston (V_2) with respect to time that is more accurate than a pure sinusoidal approximation is given by equation (4.7) [14]

$$V_2 = A_2 r_c \left(1 - \cos \omega t + \frac{\sqrt{1 - \lambda_c{}^2 \sin^2 \omega t}}{\lambda_c} \right) \tag{4.7}$$

where A_2 is the piston cross-sectional area, λ_c is the ratio of the crankshaft radius (r_c) to the length of the connecting rod, and ω is the compressor frequency. The swept volume below the piston (V_2) is given by:

$$V_1 = -A_1 r_c \left(1 + \cos \omega t - \frac{\sqrt{1 - \lambda_c{}^2 \sin^2 \omega t}}{\lambda_c} \right) \tag{4.8}$$

where A_1 is the cross-sectional area under the piston (note that A_1 plus the cross-section of the connecting rod equals A_2).

To check the accuracy of the polytropic compression assumption and to find the most suitable polytropic exponent (n), a small volume is attached to the compressor outlet.

The temperature in the compression / expansion spaces is not constant; rather it scales according to equation (4.9),

$$T = \overline{T}\left(\frac{P}{\overline{P}}\right)^{\frac{n-1}{n}} \tag{4.9}$$

where T and P are the instantaneous temperature and pressure in the compression / expansion spaces, respectively, $\overline{T}$ and $\overline{P}$ are the average temperature and pressure. Two polytropic exponents are introduced, one to characterize the compression process under the piston and another for the process in the volume above the piston. The heat loss through convection below the piston is negligible due to the relatively fast compression and expansion processes. Therefore, the polytropic exponent is assumed to be 1.67 (as appropriate for helium undergoing an adiabatic compression). The polytropic exponent above the piston may be less than 1.67 due to the influence of the heat exchanger. The most appropriate polytropic exponent for this space is determined experimentally by minimizing the fluctuation of the sum of the contained mass in all of the volumes (1-4). Figure 4.10 shows the fluctuation of contained mass in the volumes assuming a polytropic exponent of 1.52 when the compressor is operating at 15.27 Hz.

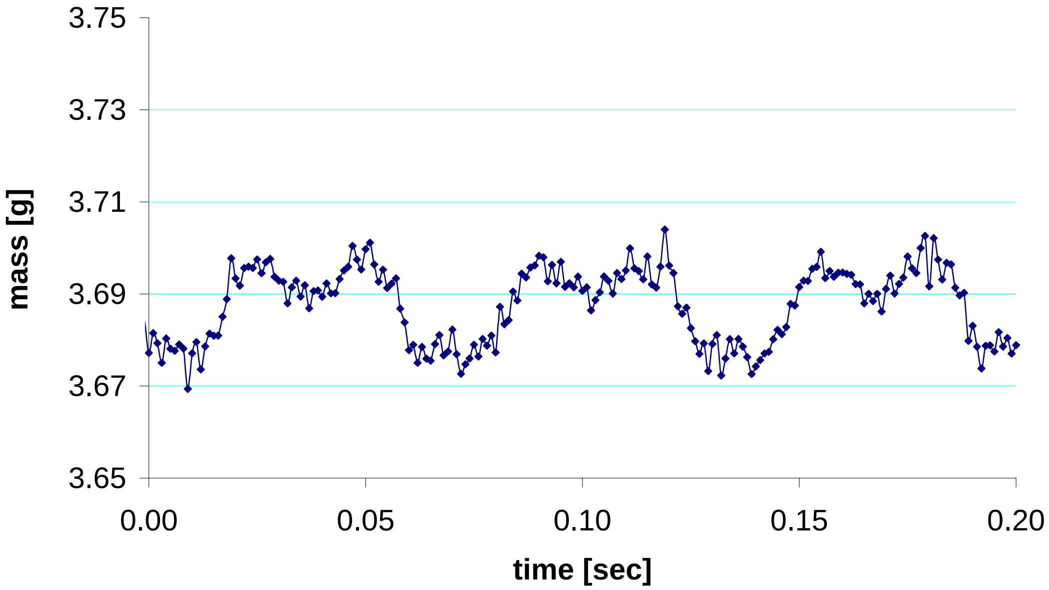

Figure 4.10 Fluctuation in contained mass calculated using a polytropic exponent of 1.52 for the compression volume with a small volume attached to the compression space.

A fluctuation of 0.017 g (0.46% of the contained mass) results when a polytropic exponent of 1.52 is applied to the compression space above the piston. Note that this represents an acceptable error in the mass flow rate.

In a subsequent test, the small volume is removed and the compressor's outlet is plugged, resulting in a large pressure ratio of 2.76. The same polytropic exponents are applied (1.67 and 1.52) and the contained mass over time is plotted again (Figure 4.11).

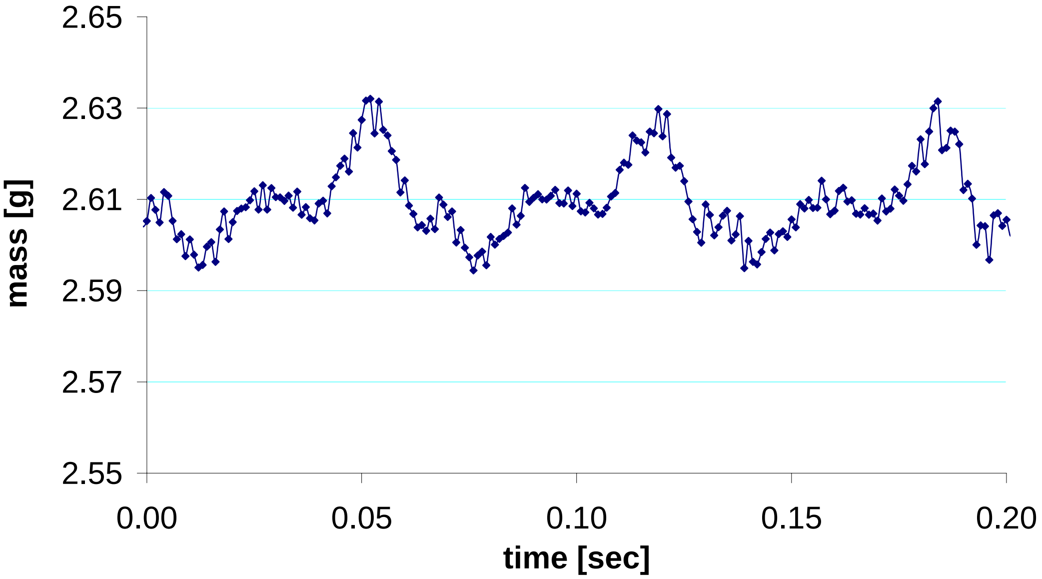

Figure 4.11 Contained mass when the compressor outlet is plugged calculated using a polytropic exponent for the compression space

The fluctuation of contained mass at this relatively high pressure ratio is still only 0.019g (0.73% of the contained mass) which is acceptable in terms of a mass flow rate error. The two tests presented above suggest that the polytropic exponent method used with the polytropic exponent of 1.52 can be used to calculate the mass flow rate with sufficient accuracy for further experiments. The mass conservation method with the assumed polytropic compression / expansion shows little fluctuation in contained mass when the compressor is plugged as well as when a small volume is attached to the expansion space. To determine if this method is also capable of determining the correct mass flow rate when mass flow is leaving the compressor, reservoirs of different sizes are attached directly to the compressor outlet. The mass flow rate out of the compressor must agree with the mass flow rate into the reservoir. The pressure measured in the reservoir can be used to calculate the magnitude of the mass flow into the reservoir, providing a verification of the mass flow measurement leaving the compression space.

The mass flow rate into the reservoir can be measured much more easily than the mass flow rate at the inlet to the compressor due to the relative simplicity associated with the reservoir. Figure 4.12 shows the system represented by the reservoir: T_i, P_i, and m_i are the initial temperature, pressure, and contained mass, respectively. Δm is the mass flow that enters or exits the reservoir between an initial and final state. W and Q represent the net amount of work and heat, respectively transferred to the gas in the reservoir.

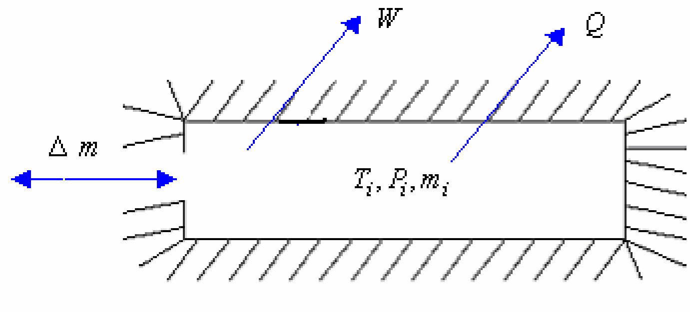

Figure 4.12 Thermodynamic system represented by the reservoir

Applying the first law of thermodynamics to the reservoir for a process that moves from an initial state to a final state and assuming ideal gas behavior, an adiabatic boundary, and that the gas enters always at the initial temperature T_i yields:

$$0 = (m_i + \Delta m) c_v T_f - m_i c_v T_i - \Delta m c_p T_i \tag{4.10}$$

Solving for the change in mass results in:

$$\Delta m = m_i \frac{T_i - T_f}{T_f - \kappa T_i} \tag{4.11}$$

where κ is the ratio of the constant pressure to constant volume specific heat capacity rates, T_i is the initial temperature (assumed equal to room temperature), and m_i can be determined from the equation of state for ideal gas. T_f can be calculated with Eq. (4.9) where κ is assumed to be 1.67 (adiabatic compression of the helium gas). The magnitude of the mass flow rate into the reservoir is the product of the angular frequency (ω) and the maximum change of contained mass (Δm) over a cycle. This technique is used to compute the mass flow rate into the reservoir in this and the subsequent chapter.

Figure 4.12 shows the experimental setup used to check the agreement of the mass leaving the compressor against the mass flow entering the reservoir. A 7.84 liter reservoir is attached to the compressor outlet and the compressor is operated at 15.27 Hz.

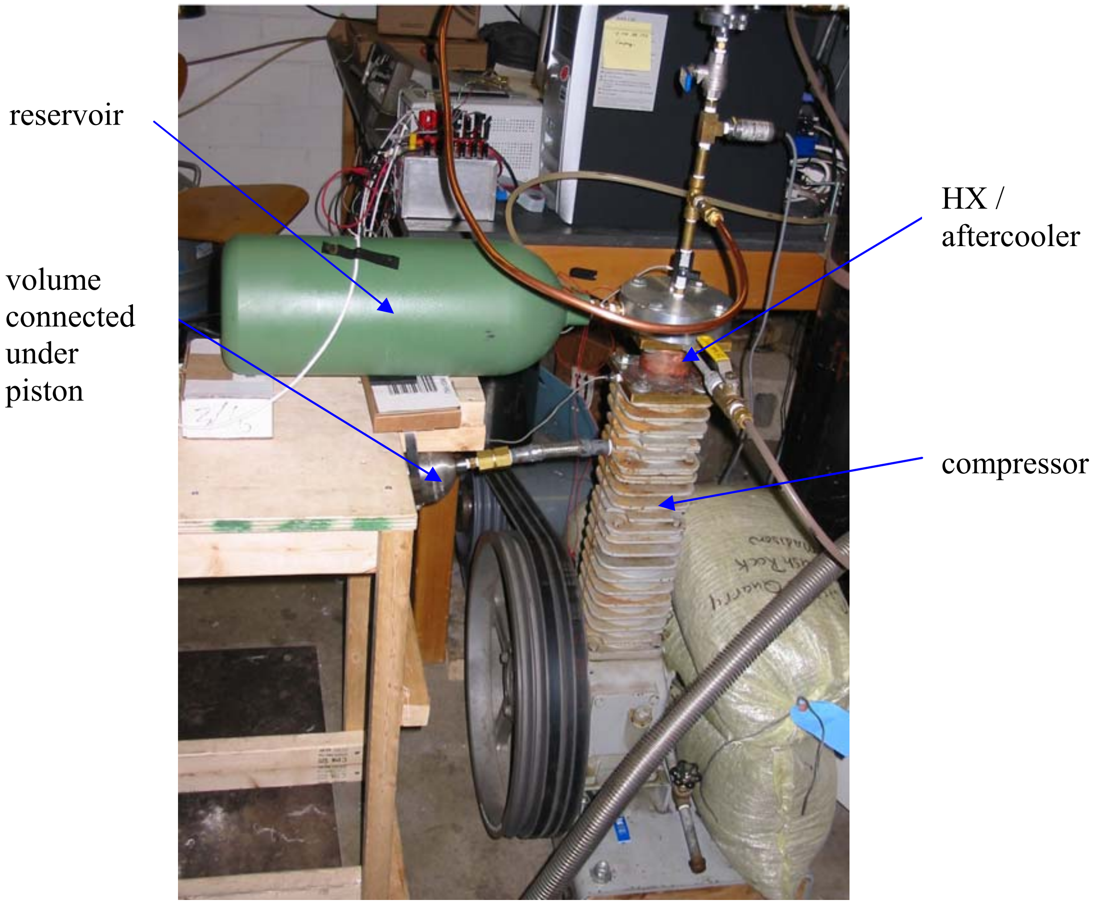

Figure 4.13 Experimental setup used to verify the mass flow rate measured using the polytropic mass conservation method

Table 4.1 summarizes the measurements of the mass leaving the compression space and entering the reservoir as well as other constants that are used in the calculation.

Table 4.1 Summary of the results of the mass flow consistency check

	Polytropic exponents			**Mass flows**		**Error**
Reservoir volume	below piston	above piston	reservoir	leaving compressor	into reservoir	
(liter)				(g/s)	(g/s)	(%)
0.66	1.67	1.52	1.67	15.44	13.43	15
7.84	1.67	1.52	1.67	22.19	20.35	9

The difference between the two calculated mass flows is 9% and 15% for the large and small reservoir, respectively. To summarize this chapter, careful experimental verification showed that none of the three mass flow rate measurement techniques were found to be capable of measuring the high pressure, frequency, and large mass flows to better than 15-20%. Although this level of uncertainty may be reasonable given the level of difficulty associated with this measurement, it is not sufficient to verify the distributed component model. Experimental data is presented in the next chapter that is evaluated using these methods for determining the mass flow into inertance tubes. Ultimately, the distributed component model is verified by comparison of the predicted mass flow rate in to the reservoir and pressure along the length of the inertance tube against measurements of these values.

5 EXPERIMENTS

The experimental results of the measured inertance effect are presented and compared with the models' predictions in this chapter. In the first section, measurements are made at 10.8 Hz operating frequency and the mass flow rate at the inlet to the inertance tube is predicted using the isothermal mass conservation technique. The comparison between the model prediction and measured data is not very good. The uncertainty in the mass flow rate measurements is assumed to be responsible for this poor agreement.

In the second section, measurements are presented at a compressor operating frequency of 15.3 Hz. The mass flow rate at the inlet to the inertance tube is predicted using the polytropic exponent mass conservation technique. The comparison between the predicted and measured inlet mass flow rate was found to be better but still not satisfactory. However, the model was found to be capable of accurately predicting the time varying mass at every location in the inertance tube and the mass flow rate into the reservoir with good accuracy. Therefore, the discrepancy between the predicted and measured mass flow rate at the inlet to the inertance tube is certainly related to the uncertainty in the measurement of this mass flow rate rather than any fundamental problem with the model.

5.1 Experiments at 10.81 Hz compressor operating frequency

The first set of experiments is conducted at a compressor operating frequency of 10.8 Hz and the mass flow rate is evaluated using the isothermal mass conservation method that was discussed in section 4.4.

5.1.1 Experimental setup

Figure 5.1 shows the experimental setup used for the inertance measurements. Three pressure transducers are mounted to the compressor; one below the piston, one above the piston, and one at the compressor outlet. An additional (4th) pressure transducer is located in the reservoir. The pressure transducer's characteristics are described in Chapter 4.1.1.

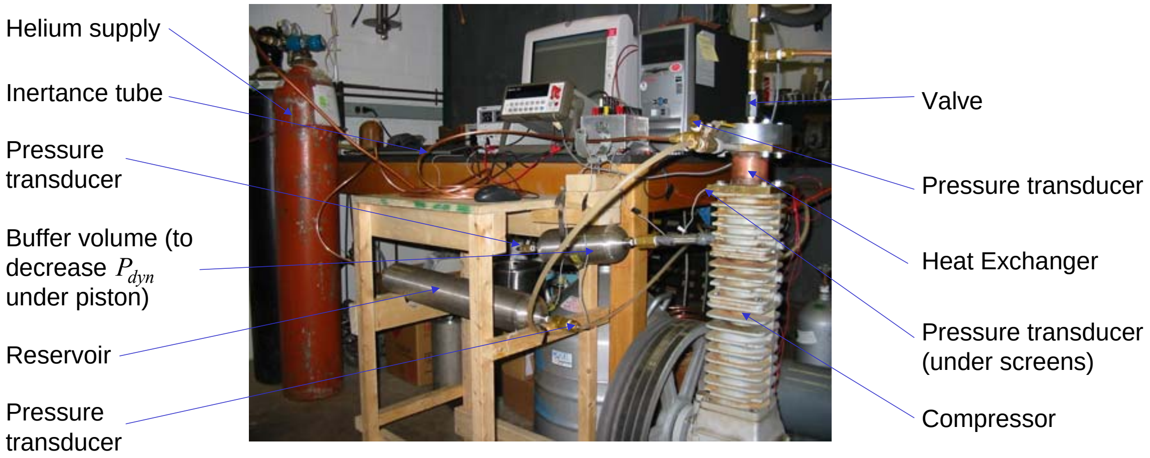

Figure 5.1 Experimental setup used to measure the inertance tube inlet mass flow rate using the isothermal mass conservation technique

Table 5.1 summarizes the operating conditions and volumes used for this experiment. Note that volume 1 refers to the sum of the swept and void volume under the piston, volume 2 to the sum of the swept and void volume above the piston, volumes 3 to the void volume in the heat exchanger's screens and volume 4 to the volume between the heat exchanger and the compressor outlet. The term 'contained' volume refers to the combination of volumes V1, V2, V3, and V4.

Table 5.1 Specification of the operating conditions and volumes associated with the 10.8 Hz experiments

Frequency	Temperature	Sample frequency	Volumes						
			V 1 swept	V 1 void	V 2 swept	V 2 void	V 3	V 4	Reservoir
(Hz)	(K)	(Hz)	(liter)	(liter)	(liter)	(liter)	(liter)	(liter)	(liter)
10.81	295	1000	0.972	0.2718	0.29	0.0612	0.0475	0.127	3.78

5.1.2 Data reduction

The data recorded from the pressure transducers and the reed relay (top dead center position of the compressor piston) must be reduced in order to obtain the contained mass in the volumes and from this the mass flow rate entering the inertance tube. This was accomplished using an Excel spreadsheet. The calculations are carried out for every data point; a sampling rate of 0.5 ms was used. The instantaneous values of volumes 1 and 2 are the sum of an un-swept volume and an instantaneous swept volume, respectively. The swept volumes are obtained using a sinusoidal approximation of the compressor piston kinematics. The time at which the piston hits its top dead center position is recorded by the reed relay that is mounted to the compressor wheel. The contained mass in all volumes is calculated assuming helium obeys the ideal gas law. The product of the maximum fluctuation of the contained mass and the angular frequency of the compressor yields the magnitude of the mass flow. The pressure at the inertance tube inlet and the contained mass in the compressor can be overlaid in order to determine the phase between the mass flow and the pressure graphically. Figure 5.2 shows an example of such a graph produced by a typical run. Note that the product of the contained mass and the angular frequency is the measured magnitude of the mass flow rate and that the mass flow rate is 90° out of phase from the contained mass

(mass flow rate is the derivative of contained mass). Stated differently, the contained mass curve (the blue symbols in Fig. 5.2) must be shifted by 90º to the right in order to get the phase between the mass flow rate and the pressure (the red symbols in Fig. 5.2).

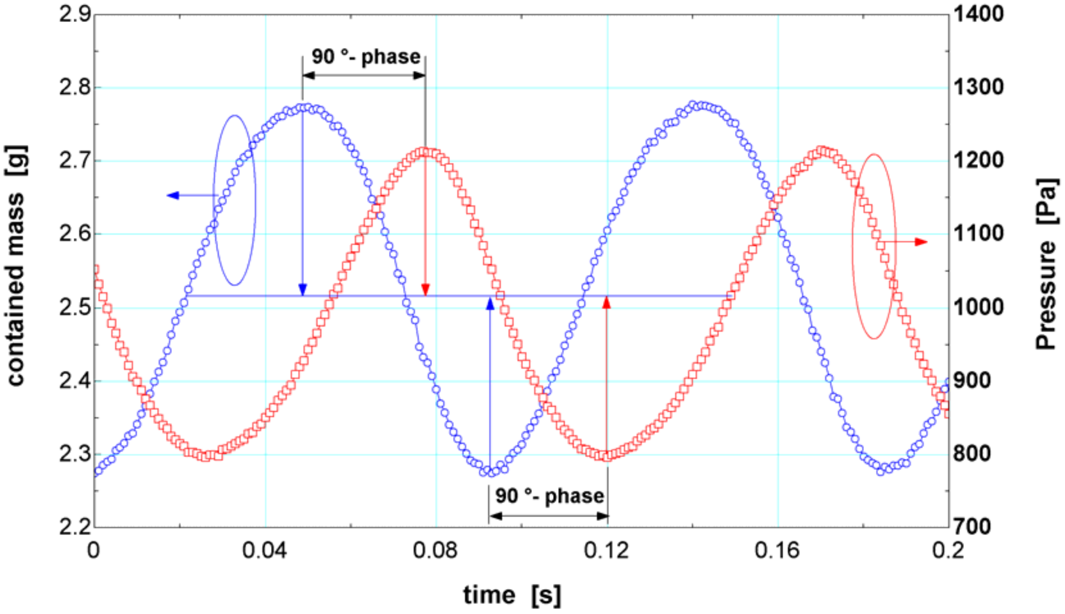

Figure 5.2 Contained mass in volumes 1 through 4 and pressure at the inertance tube inlet as a function of time for a typical run. Note that the magnitude of the mass flow rate can be determined from the product of the amplitude of the contained mass and the angular frequency of the compressor and the phase between the mass flow rate and pressure is related to the phase between the contained mass and the pressure.

Initially the phase between the pressure and the contained mass was determined by measuring the time separating the peak pressure from the peak contained mass. The time increment from valley to valley was also measured and these values were averaged and converted into a phase difference (in degree). To obtain the phase between mass flow rate and pressure, the phase between contained mass and pressure is subtracted from 90º. Note that the subtraction from 90º is equivalent to approximating the contained mass variation with a sinusoid and differentiating with respect to time. The phase shift between the pressure and the mass flow rate in Figure 5.2 is very close to zero after subtracting the 90º.

5.1.3 Experimental results

Table 5.2 summarizes all measured phase angles and acoustic powers calculated according to Eq. (2.21). Each measurement was repeated five times and the average of these 5 trials is reported in Table 5.2. The variation between the five trials represents the precision if not the accuracy of the experiment. The precision of the phase angle measurements is approximately ±3 degrees and precision (or repeatability) of the acoustic power measurements was 1-4%. Three different inertance tube diameters (1/4" OD, 3/8" OD, and 1/2"OD or 4.83 mm ID, 7.90 mm ID, and 11.07 mm ID) were tested at lengths ranging from 5' to 50' (1.52 m to 15.24 m).

Table 5.2 Summary of the phase and acoustic power measurements taken at the 10.8 Hz compressor frequency. Note that each reported measurement is the average of 5 trials.

	Phase [deg]						Accoustic Power [W]					
Length [m]	**4.83 mm ID**		**7.90 mm ID**		**11.07 mm ID**		**4.83 mm ID**		**7.90 mm ID**		**11.07 mm ID**	
	1 MPa	**2 MPa**	**1 MPa**	**2 MPa**	**1 MPa**	**2 MPa**	**1 MPa**	**2 MPa**	**1 MPa**	**2 MPa**	**1 MPa**	**2 MPa**
1.52	-14.1	-15.1	-9.1	-11.3	-53.2	-55.2	1190	2379	746	1388	207	368
3.05	-15.1	-16.4	-3.9	-2.6	-29.6	-30.9	1049	2099	882	1626	339	606
4.57	-20.9	-22.5	-3.9	-3.6	-8.9	-10.2	985	1990	965	1800	422	760
6.10	-23.8	-26.1	-4.0	-4.3	-0.7	0.4	977	1862	1021	1923	459	839
7.62	-30.4	-30.2	-11.6	-6.8	3.5	4.6	890	1678	1046	1986	525	973
9.14	-33.1	-32.9	-13.3	-8.5	4.4	8.6	842	1579	1049	2042	584	1072
10.67	-35.2	-35.7	-14.6	-11.4	6.0	8.4	818	1631	1028	2078	638	1178
12.19	-37.9	-38.1	-19.2	-7.4	5.4	9.3	755	1426	1013	2117	704	1307
13.72	-40.8	-40.4	-21.3	-17.2	3.1	9.7	753	1515	980	2034	754	1419
15.24	-43.1	-43.1	-35.2	-19.0	2.6	9.8	723	1450	769	2050	792	1495

Note that here a negative phase angle corresponds to the mass flow rate leading the pressure, whereas this sign convention is reversed in sections 5.2 and 5.3.

5.1.4 Comparison with the transmission line and lumped component models

The experimental data for the 3/8" OD and 1/2" OD tube is compared with the transmission line model and the lumped component model in this section. Figures 5.3 and 5.4 present the predicted and measured phase and acoustic power, respectively, as a function of the inertance tube length operating with a 1/2" OD tube and a mean pressure of 20 bars. Figures 5.5 and 5.6 present the same information for the 3/8" OD tube.

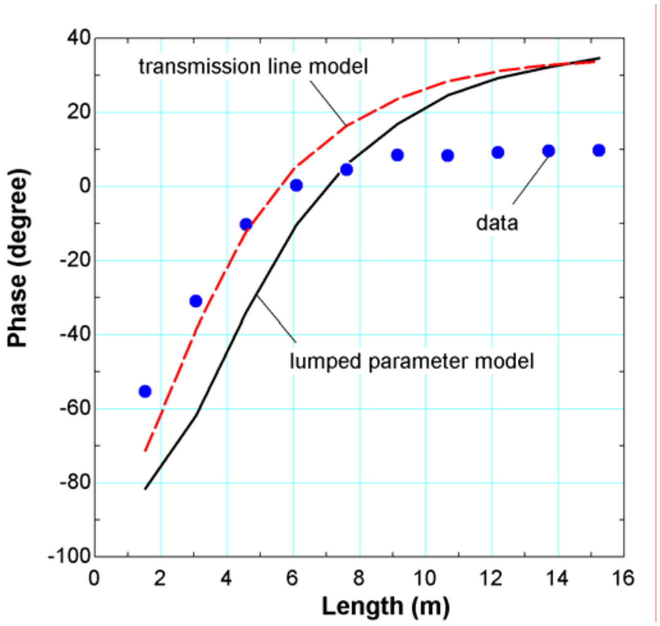

Figure 5.3 Experimentally measured and predicted phase between the mass flow rate and pressure as a function of length for the 1/2" OD (11.07mm ID) tube operating at 10.8 Hz and 20 bar.

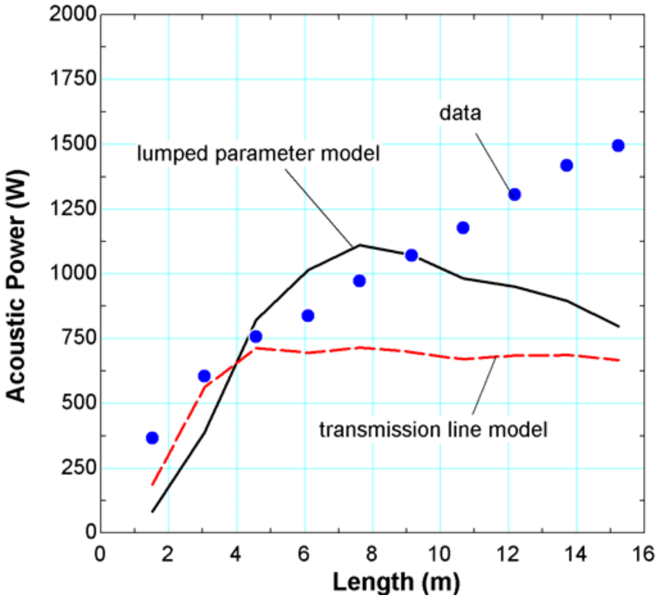

Figure 5.4 Experimental and predicted acoustic power as a function of length for the 1/2" OD (11.07mm ID) tube operating at 10.8 Hz and 20 bar.

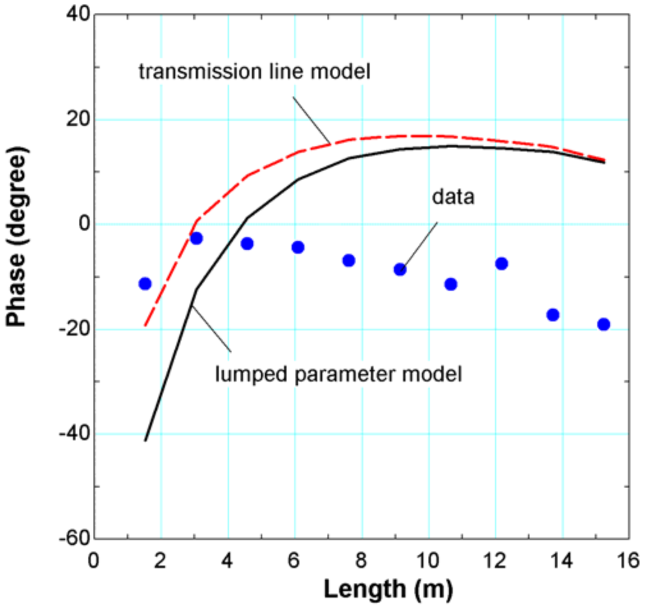

Figure 5.5 Experimentally measured and predicted phase between the mass flow rate and pressure as a function of length for the 3/8" OD (7.09mm ID) tube operating at 10.8 Hz and 20 bar.

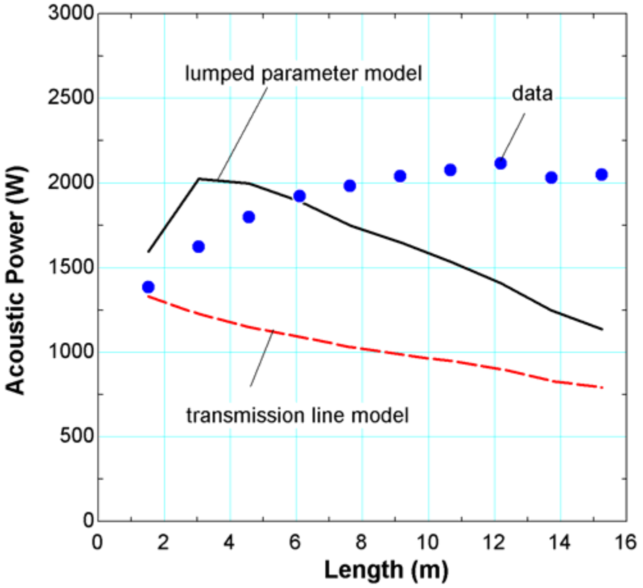

Figure 5.6 Experimental and predicted acoustic power as a function of length for the 3/8" OD (7.09mm ID) tube operating at 10.8 Hz and 20 bar.

The measured phase and acoustic power for the 1/2" OD short tube shows some agreement with the models' predictions. However, at longer lengths the measurements disagree with the predictions, in some cases both qualitatively as well as quantitatively. The measurements for the 3/8" OD tube show little agreement with the predictions for all lengths.

The most likely source of the disagreement lies in the mass flow rate measurement rather than in shortcomings associated with the model. Experimental results presented later in this chapter show that the model is capable of very accurately predicting the time varying pressure at every location in the inertance tube as well as the time varying mass flow rate at the inlet to the reservoir. As described in section 4.4, the mass flow rate measurement using the isothermal conservation of mass technique relies on a calibration step in which the volume under the piston is adjusted in order to minimize the change in contained mass for a test condition in which the inertance tube is removed and the outlet port capped. The calibration step is carried out only for one specific set of operating conditions and, in particular, for a relatively high pressure ratio. Since the pressure ratio changes dramatically as the inertance tube length is adjusted, the accuracy of the mass flow rate measurement likely suffers away from this calibration condition.

One interesting observation that resulted from this set of experiments is that there is a significant entrance effect at the inlet to the reservoir. Figure 5.7 illustrates the pressure as a function of time measured at the inertance tube inlet, exit, and within the reservoir for a typical experimental condition. The entrance effect is shown in Figure 5.7 by the large difference between the pressure measured at the exit of the inertance (just before the reservoir) and the pressure measured in the reservoir itself. This measured pressure difference persists even when the transducers are swapped and is therefore not an artifact of a poor calibration or a floating transducer output. The resistance associated with the entrance effect causes a large pressure drop that is not accounted for in either the transmission line model or the lumped component model. It was this observation that eventually motivated the distributed component model, described in chapter 2.

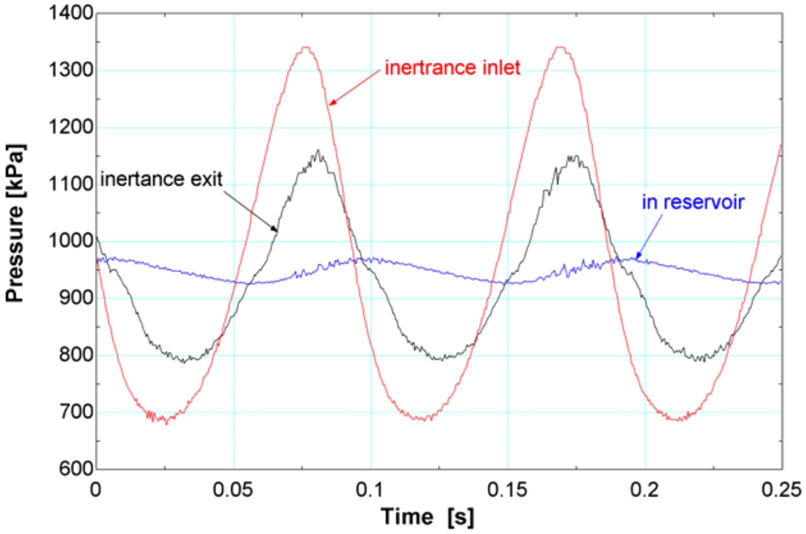

Figure 5.7 Pressure as a function of time measured at the inlet and exit of the inertance tube and inside the reservoir. Note the significant entrance effect indicated by the large difference between the pressure at the inertance tube exit and in the reservoir.

5.2 Experiments at 15.3 Hz compressor frequency

Once the entrance effect at the reservoir inlet was identified, the fittings that connect the inertance tube to the reservoir were bored through so that they matched the inner diameter of the inertance tube and provided a smooth transition from the tube to the reservoir. A second set of experimental data was collected. The 1 gallon reservoir was exchanged with a 7.84 liter reservoir and the frequency was elevated to 15.3 Hz in order to obtain a more dramatic phase shift that approaches the optimal phase described in Chapter 1.

In an attempt to achieve better accuracy measurement of the mass flow rate at the inlet to the inertance tube, the polytropic mass conservation method described in section 4.5 was developed and implemented. The same experimental setup presented in section 5.1 was used; the differences included the with the exception of the larger reservoir volume and the addition of a pressure transducer immediately ahead of the reservoir. This additional pressure transducer together with the one in the reservoir allows the calculation of the resistance associated with the transition between the inertance tube and the reservoir. The resistance is defined as the ratio of the pressure drop to the magnitude of the mass flow rate. The mass flow rate into the reservoir can be determined using mass conservation on the reservoir, as described previously in section 4.5. The experimental results are summarized in Table 5.3. Note that the phase angle convention has changed. A positive phase corresponds to the mass flow leading pressure. This convention is consistent with Lou's and Radebaugh's [7].

Table 5.3 Summary of phase and mass flow rate measurements using a compressor frequency of 15.3 Hz

	Phase [deg]		**Mass flow [g/s]**	
Length [m]	**7.90 mm ID**	**11.07 mm ID**	**7.90 mm ID**	**11.07 mm ID**
	1 MPa	**1 MPa**	**1 MPa**	**1 MPa**
1.52	-1.2	-13	22.09	23.55
3.05	3	-19	20.98	24.00
4.57	8.8	-17.8	19.40	23.69
6.1	12.4	-15.4	18.25	23.18
7.62	18.4	-11.8	17.50	22.94
9.14	22.6	-7	17.31	22.43
12.19	29.2	2.8	16.47	21.09
15.24	33.4	15.6	16.03	19.50

Figures 5.8 and 5.9 present the measured and predicted phase and the mass flow rate, respectively, as a function of length for the 1/2" OD inertance tube. The predicted values are associated with the distributed component model. Figures 5.10 and 5.11 present the same information for the 3/8"OD tube.

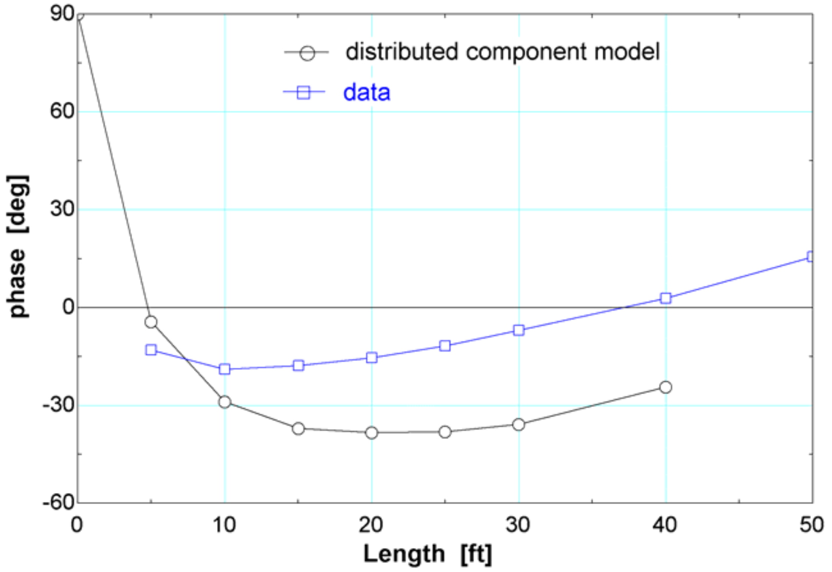

Figure 5.8 Experimentally measured and predicted phase between the mass flow rate and pressure as a function of length for the 1/2" OD (11.07 mm ID) tube operating at a compressor frequency of 15.3 Hz

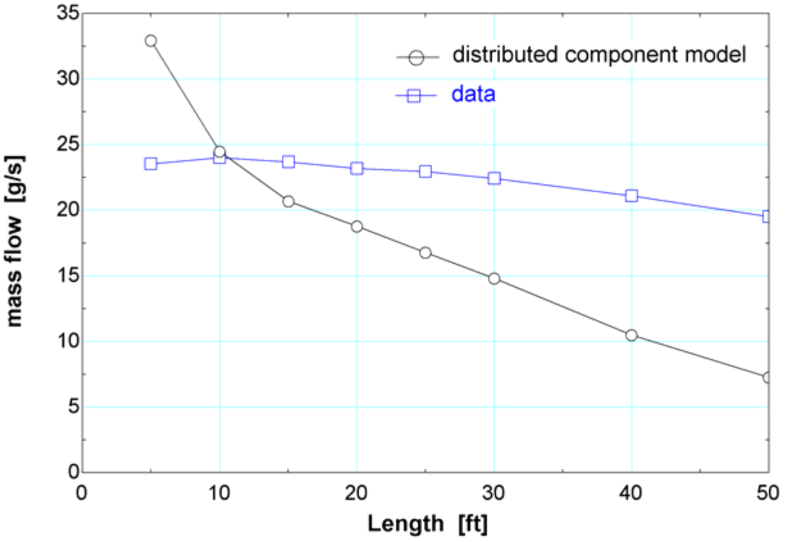

Figure 5.9 Experimental and predicted mass flow rate as a function of length for the 1/2" OD (11.07mm ID) tube operating at a compressor frequency of 15.3 Hz

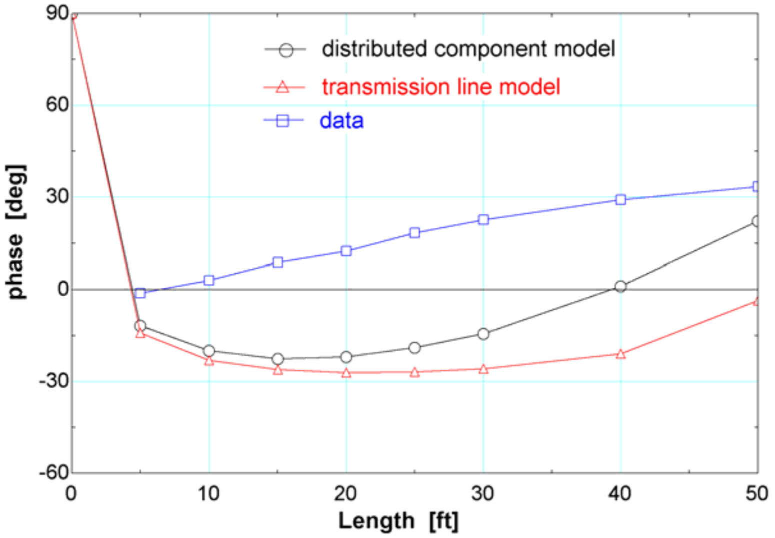

Figure 5.10 Experimentally measured and predicted phase between the mass flow rate and pressure as a function of length for the 3/8" OD (7.09 mm ID) tube operating at a compressor frequency of 15.3 Hz

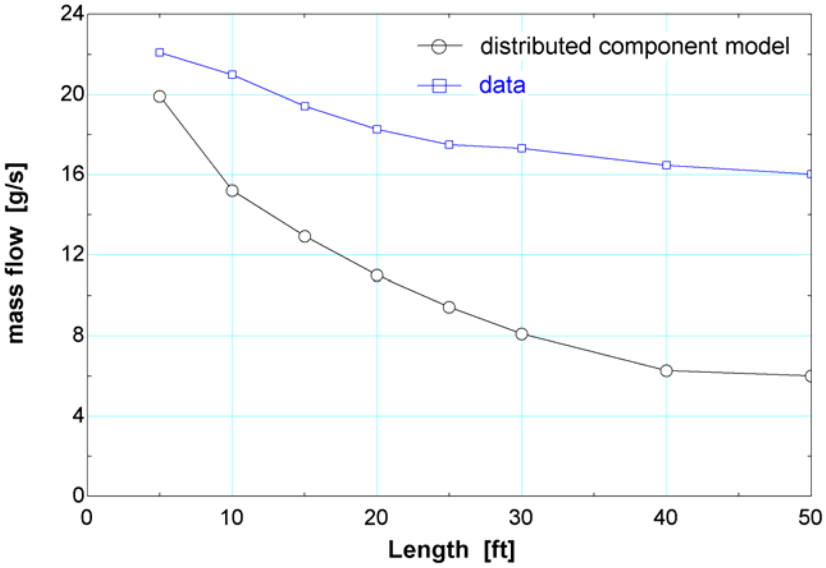

Figure 5.11 Experimental and predicted mass flow rate at the inertance inlet as a function of length for the 3/8" OD (7.09mm ID) tube operating at a compressor frequency of 15.3 Hz

Figure 5.12 shows the experimentally deduced (sinusoidal approximation) and predicted mass flow rates for a 20 feet, 1/2"OD inertance tube. Error bars indicate the estimated error according to the discussion in section 4.5 (about 10% absolute error for the mass flow).

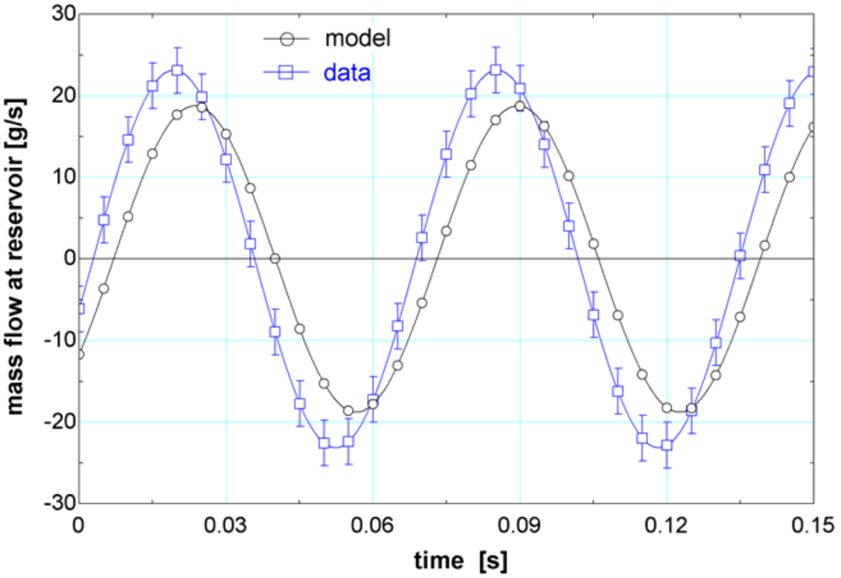

Figure 5.12 Experimental and predicted mass flow rate at the inertance tube inlet

The predicted mass flow curve in Figure 5.12 cannot be matched with the experimental data, even if an experimental error of 10% is assumed. The disagreement between predicted and measured phase and mass flow grows with longer inertance tubes (Figures 5.8-5.11). Very little improvement in terms of agreement was observed between the predictions and measurements for the data taken at 15.3 Hz versus the data taken at 10.81 Hz described in the previous section, even with the inclusion of the entrance effect in the model and the use of the more accurate polytropic mass conservation method.

This motivated further investigation into where the model and experimental data agree and where they disagree. Eventually it was found that good agreement is evident between the predicted and measured mass flow rate as a function of time into the reservoir as well as the predicted and measured pressures at any location along the inertance tube.

Figures 5.13 shows the mass flow rate into the reservoir as a function of time as well as the predicted mass flow rate into the reservoir. The agreement between data and model is very good for this quantity. Figures 5.14 illustrates the measured pressure at the inertance tube inlet and halfway through a 20 ft long inertance tube (at x=10 ft). The model prediction for the pressure at x=10 ft is also shown. Again note the good agreement between model and experiment not only in terms of magnitude but also phase indicating that the model is capable of predicting both the resistive as well as the compliant and inertive elements of the tube's behavior. Figure 5.15 illustrates the pressure at the inertance tube inlet and the predicted and measured pressure in the reservoir. Again, both the magnitude and the very substantial phase shift are accurately predicted.

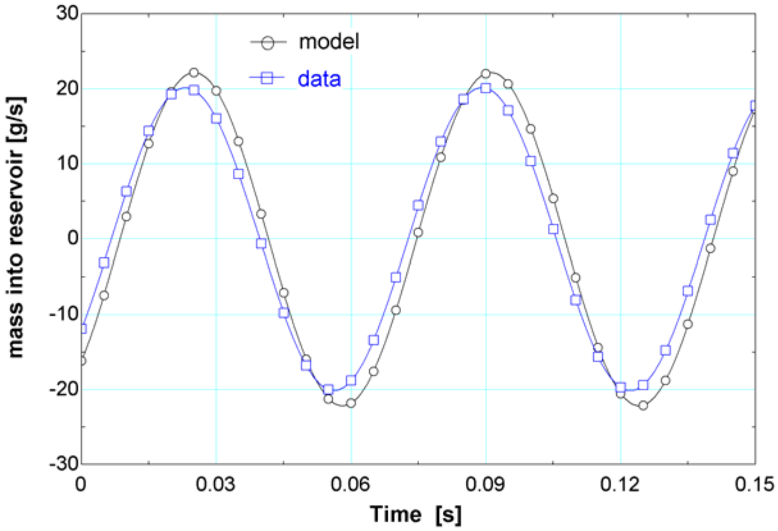

Figure 5.13 Experimental and predicted mass flow into the reservoir as a function of time for a 20 feet, 1/2 OD inertance tube

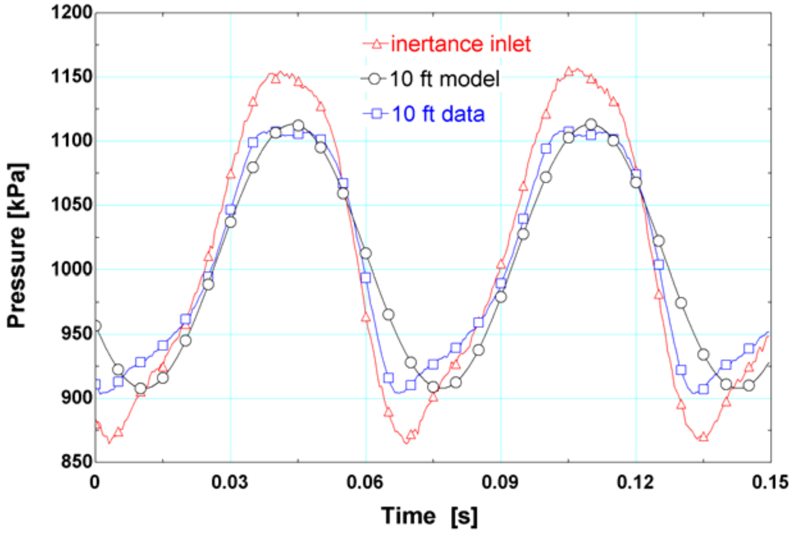

Figure 5.14 Measured and predicted pressure halfway along (i.e., at x=10 feet) a 20 foot long inertance tube as a function of time for a ½" OD inertance tube. Also shown is the measured pressure variation at the inertance tube inlet.

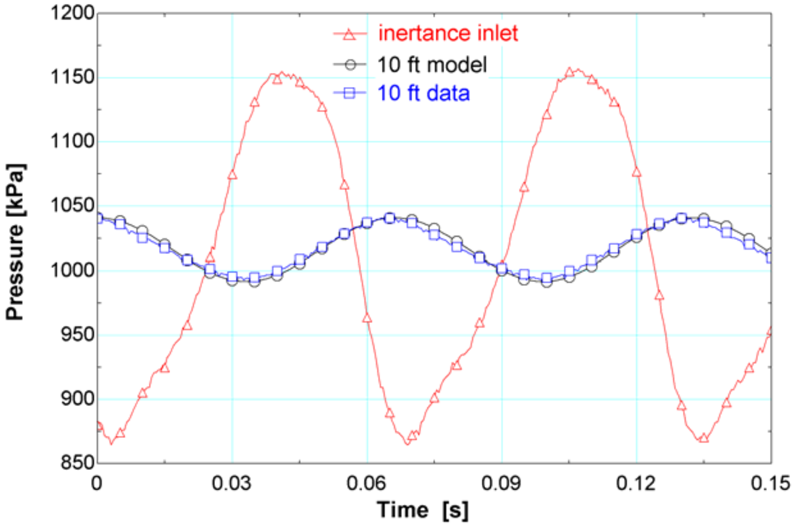

Figure 5.15 Measured and predicted pressure in the reservoir for a 20 foot long, ½" OD inertance tube. Also shown is the measured pressure variation at the inertance tube inlet.

The good agreement between the data and the predictions of pressures and the reservoir mass flow calls into question the validity of measuring the mass indirectly when an inertance tube is attached to the compressor, although it was shown in Chapter 4 that this indirect method works when no inertance tube is attached. The model is capable of predicting pressures along the inertance tube over a range of inertance tube lengths. Figures 5.16 shows the measured and predicted pressure half-way through a 10 foot long, 1/2" OD inertance tube. Figure 5.17 illustrates the same information for the pressure in the reservoir for the 10 ft tube. Figures 5.18 and 5.19 illustrates the measured and predicted pressure at x=10 ft and x=25 ft for a 40 ft long inertance tube. Finally, Figure 5.20 illustrates the measured and predicted pressure in the reservoir for the 40 ft tube.

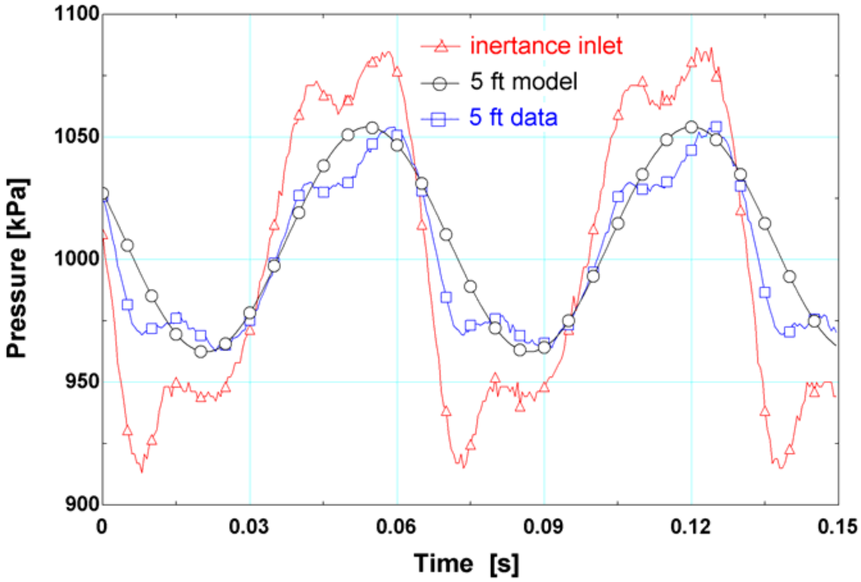

Figure 5.16 Measured and predicted pressure at the mid-point (i.e. at x=5 ft) for a 10 ft, ½" OD inertance tube

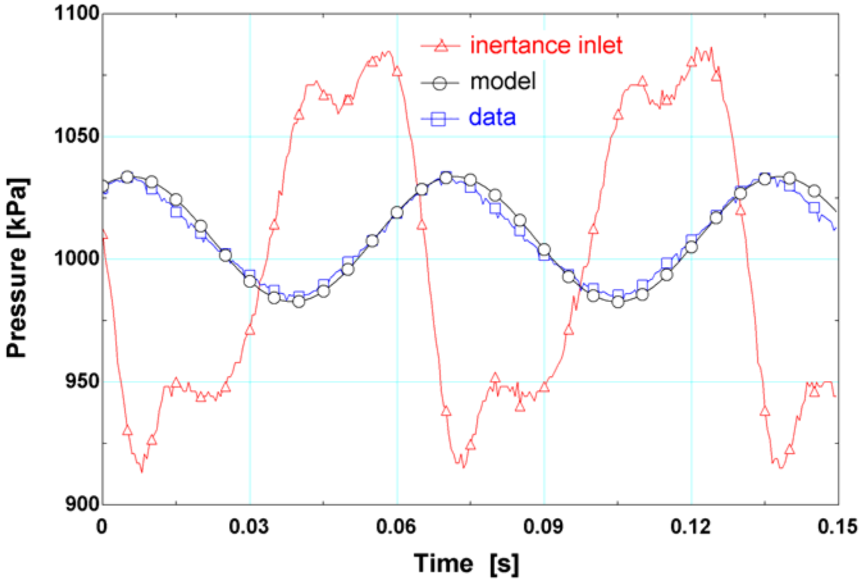

Figure 5.17 Measured and predicted pressure in the reservoir for a 10 feet, ½"OD inertance tube

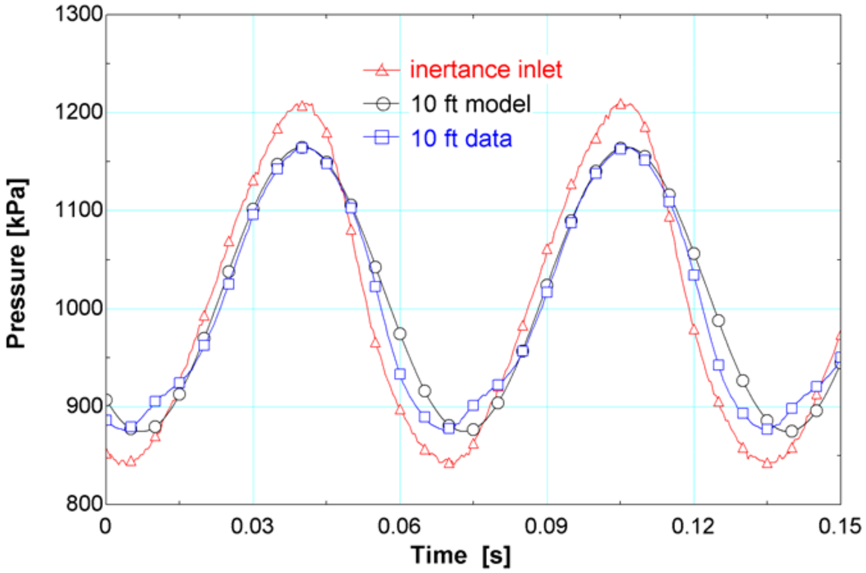

Figure 5.18 Measured and predicted pressure at x=10 ft for a 40 ft long, ½" OD inertance tube

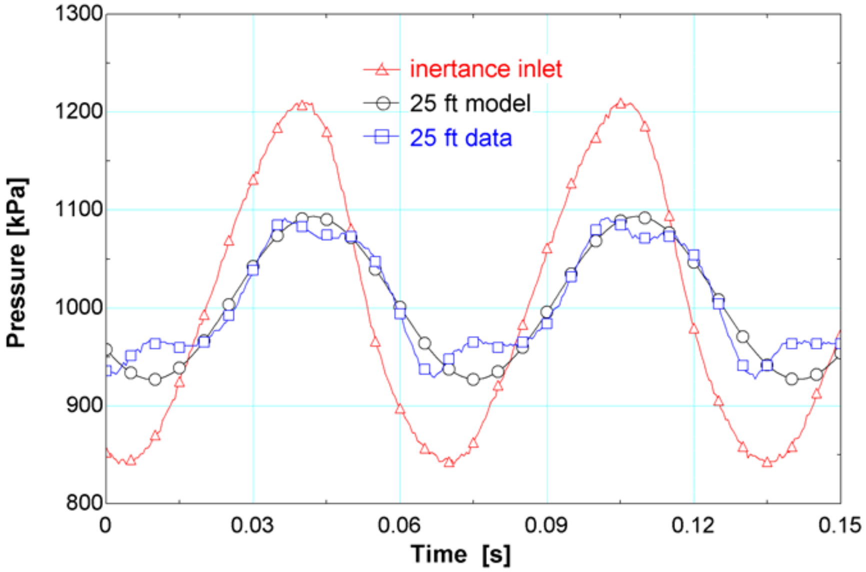

Figure 5.19 Measured and predicted pressure at x=25 ft for a 40 feet, ½" OD inertance tube

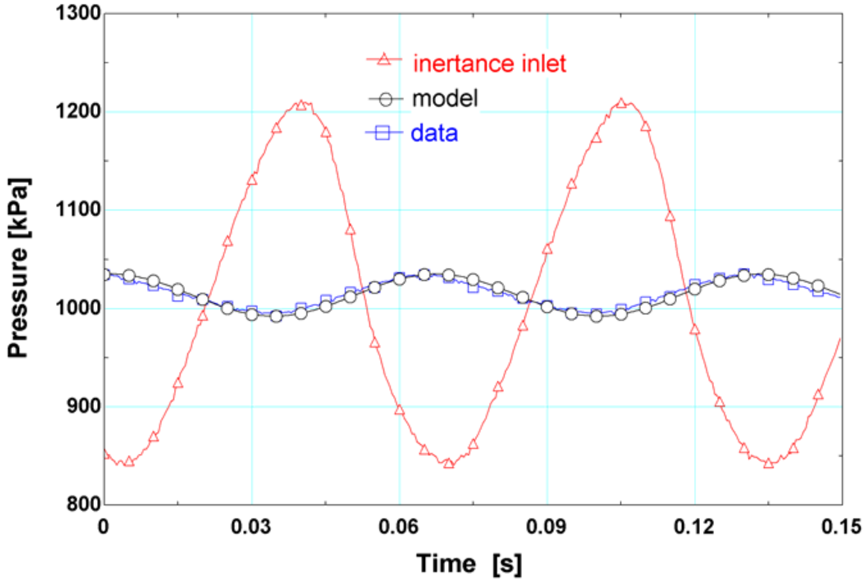

Figure 5.20 Measured and predicted pressure in the reservoir for a 40 ft long, 1/2" OD inertance tube

5.2.1 Phase and mass flow into the reservoir

It is most convenient to verify the inertance tube models by measuring the mass flow rate and its phase relative to the pressure at the inertance tube inlet because the pulse tube designer knows the desired conditions there. However, it is difficult to measure the mass flow at this location, as discussed in Chapters 4 and 5. The best option for this measurement is the polytropic mass conservation method. However, section 5.2 showed that even the polytropic mass conservation method., which shows acceptable accuracy when no inertance tube is connected to the compressor, seems to fail at predicting the mass flow correctly at the inertance inlet under most experimental conditions. However, the mass flow rate into the reservoir can be predicted using the thermodynamic technique discussed in section 4.5. The simplicity of the reservoir system, as compared to the compressor with its moving piston, leakage, etc. makes this measurement much more straightforward and accurate. The phase of the mass flow rate into the reservoir compared to the pressure at the inertance tube inlet can be obtained by subtracting 90º from the phase between the pressure in the reservoir and the pressure at the inertance tube inlet. The mass of gas in the reservoir is proportional to the reservoir pressure (by assumption) and therefore the mass flow rate is 90º out of phase relative to this pressure. Since the distributed component model can predict phase, pressure, and mass flow in the reservoir as well as anyplace else in the inertance tube, it is sufficient to compare the experimental data to the predictions for the reservoir mass flow rate and phase in order to verify the model. Figures 5.21 through 5.24 show the predicted and measured phase and magnitude of the mass flow rate into the reservoir as a function of length for a 3/8" OD and ½" OD inertance tube.

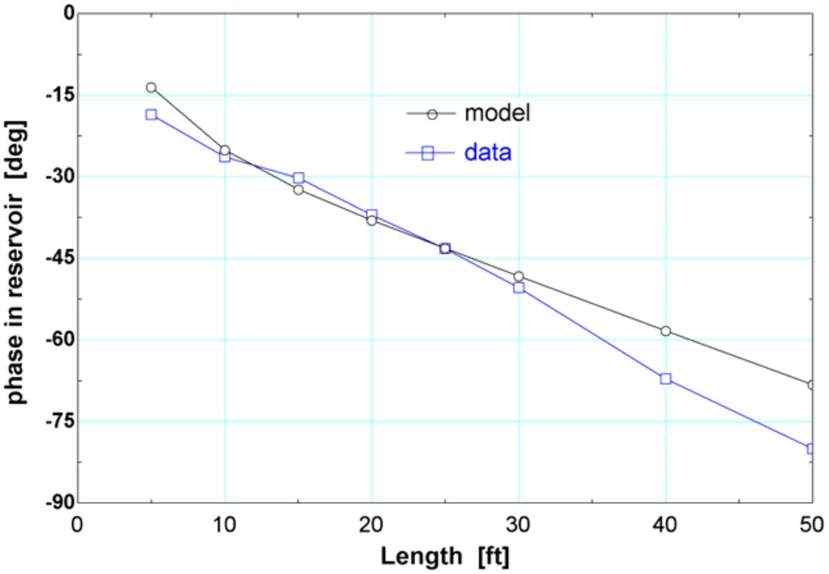

Figure 5.21 Measured and predicted phase between the mass flow rate into the reservoir and the inlet pressure as a function of length for a 3/8"OD tube

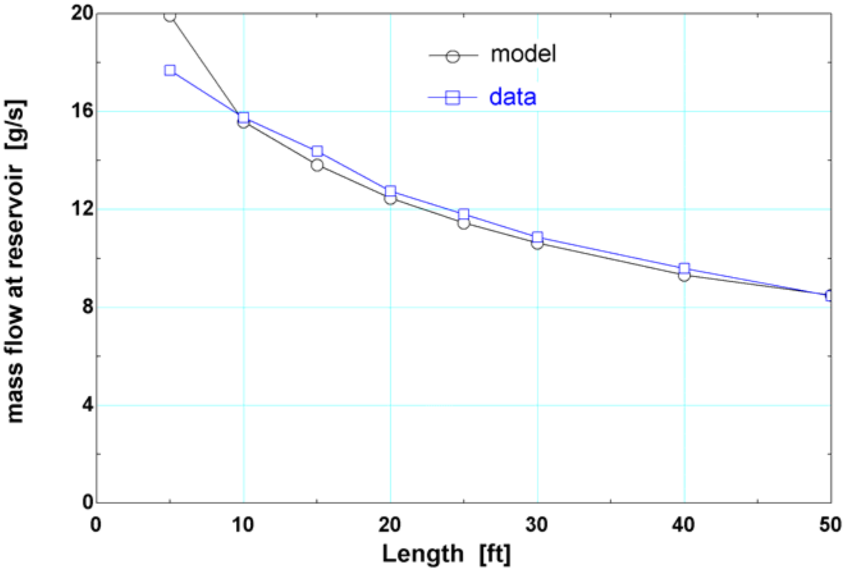

Figure 5.22 Experimental and predicted magnitude of the mass flow rate into the reservoir as a function of length for a 3/8"OD tube

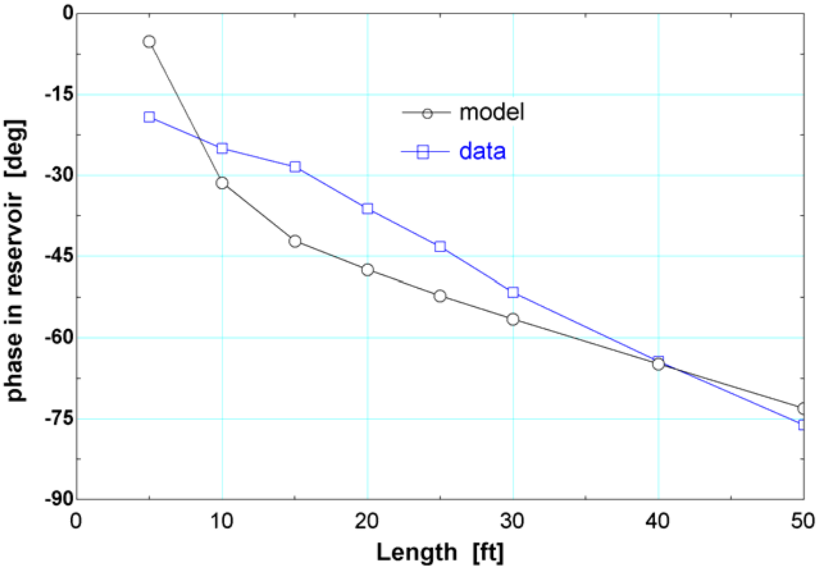

Figure 5.23 Measured and predicted phase between the mass flow rate into the reservoir and the inlet pressure as a function of length for a 1/2"OD tube

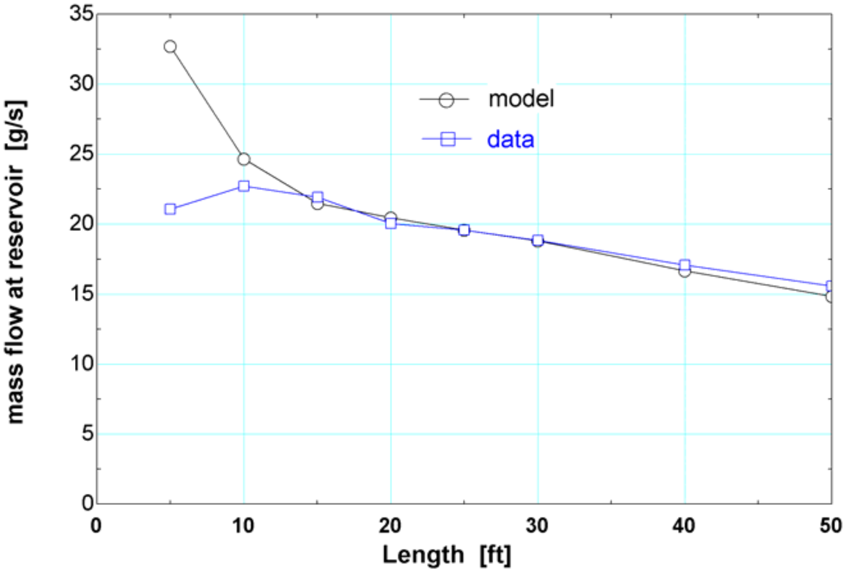

Figure 5.24 Measured and predicted magnitude of the mass flow rate into the reservoir as a function of length for a 1/2"OD tube

Excellent agreement between the predicted and measured mass flow rate into the reservoir is seen for both the 1/2"OD and 3/8"OD tubes at tube lengths over 10 ft. The prediction of the phase is also good; the maximum deviation between predicted and measured phase is 15 degrees.

6 MODELING RESULTS

The good agreement between the predicted and measured time varying mass flow rate in the reservoir and between the measured and predicted time varying pressures along the inertance tube over a range of inertance geometries is considered validation of the distributed component model. In this section, the model is further verified by comparison with the published results of a transmission line theory model. As these published results were experimentally verified, the good agreement between the distributed component model and published transmission line predictions can be taken as further verification of the model. The distributed component model is subsequently used to develop design charts; convenient graphical representation of modeling results that can be used by a pulse tube designer to determine the length and diameter of an inertance tube that will provide a given acoustic power and a desired phase shift. The design charts are presented in dimensional form for several, typical operating conditions.

6.1 Comparison of the distributed component model against published results

Lou et al. [7] present a verified inertance tube model based on transmission line theory with experimental data that is obtained from experiments performed at low acoustic powers (1-40 W) and high frequencies (30-90 Hz). It is worthwhile to compare the predictions of the distributed component model with his model's predictions. Groups, including the dimensionless diameter ($\bar{D}$),

$$\bar{D} = \frac{D}{\delta_u} \tag{6.1}$$

where δ_u is the viscous penetration depth given by the square root of the kinematic viscosity (v) over the operating frequency (ω), the dimensionless length ($\bar{L}$),

$$\bar{L} = \frac{L}{\lambda} \tag{6.2}$$

where L is the length of the inertance tube, λ is the wavelength given by the ratio of the speed of sound (α_0) to the operating frequency, and the dimensionless acoustic power ($\bar{W}$),

$$\bar{W} = \frac{W}{A\,\bar{P}\,\alpha_0} \tag{6.3}$$

where A is the cross sectional area of inertance tube, $\bar{P}$ is the mean pressure, and W is the acoustic power determined by Eq. (2.21).

Figure 6.1 illustrates the phase angle between the mass flow rate and pressure at the inlet to the inertance tube (negative mass flow phase corresponds to pressure leading the mass flow) as a function of the dimensionless length for two different dimensionless diameters assuming an infinite reservoir volume and a pressure ratio of 1.1. Note that Lou plotted the phase of the impedance versus the dimensionless length [7]. The phase of the impedance has the opposite sign as the phase between pressure and mass flow.

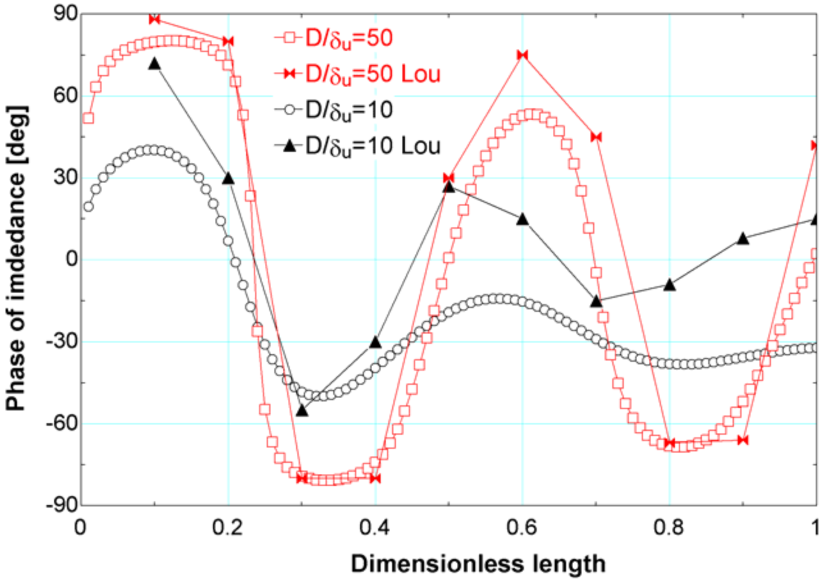

Figure 6.1 Comparison of the phase predicted by the distributed component model with the transmission line model predictions published by Lou et al.

For short dimensionless lengths these two models agree well whereas there is some discrepancy at long dimensionless lengths and small dimensionless diameters. This discrepancy is likely related from the transmission line model's inability to adjust the local resistance based on the local mass flow rate. Figure 6.2 shows the dimensionless acoustic power as a function of the dimensionless length for two different dimensionless diameters assuming an infinite reservoir volume a pressure ratio of 1.3.

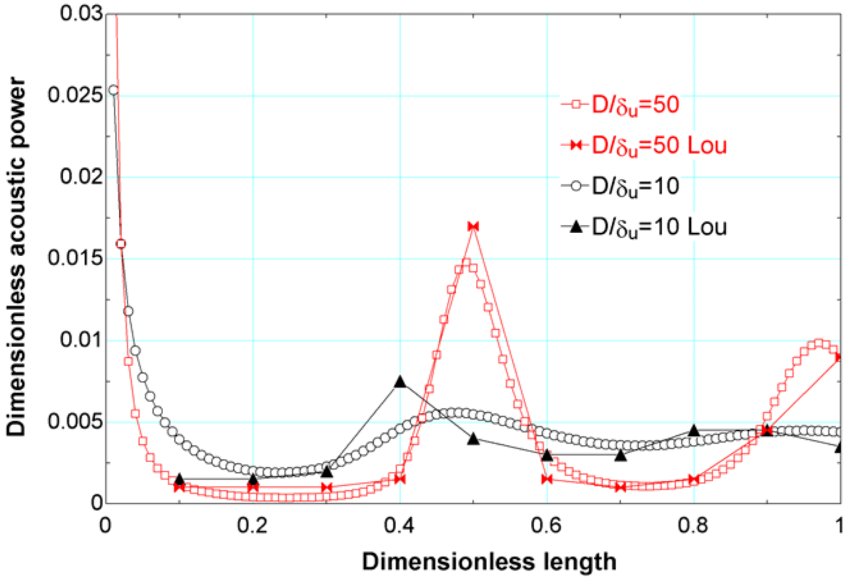

Figure 6.2 Comparison of the dimensionless acoustic power predicted by the distributed component model with the transmission line model predictions published by Lou et al.

6.2 Development of design charts

The goal of a design chart for an inertance tube is to present the pulse tube designer with a convenient, graphical technique of quickly selecting the two unknown parameters (inertance tube diameter and length) from the two parameters that are typically known (acoustic power and phase). The distributed model provides a means of relating these variables; for a given set of operating conditions, the acoustic power and phase may be predicted given any values of inertance tube length and diameter. Figure 6.3 and 6.4 show the phase of the mass flow rate with respect to pressure at the inlet to the inertance tube and the acoustic power, respectively, as a function of the inertance tube length for several values of inertance tube diameter. These figures were generated using a frequency of 30 Hz, a pressure ratio of 1.1, and a mean pressure of 25 bars.

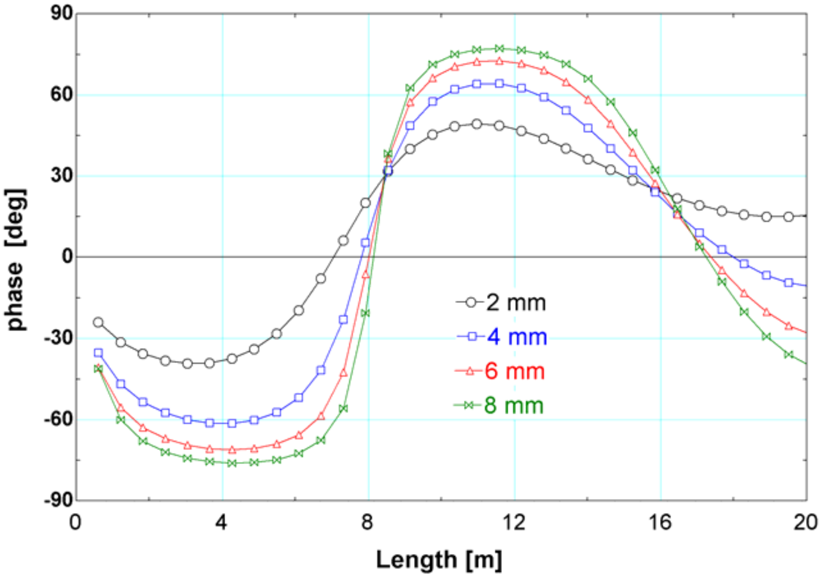

Figure 6.3 Phase as a function of inertance length for various diameters at 30 Hz, a pressure ratio of 1.1, and a mean pressure of 25 bars

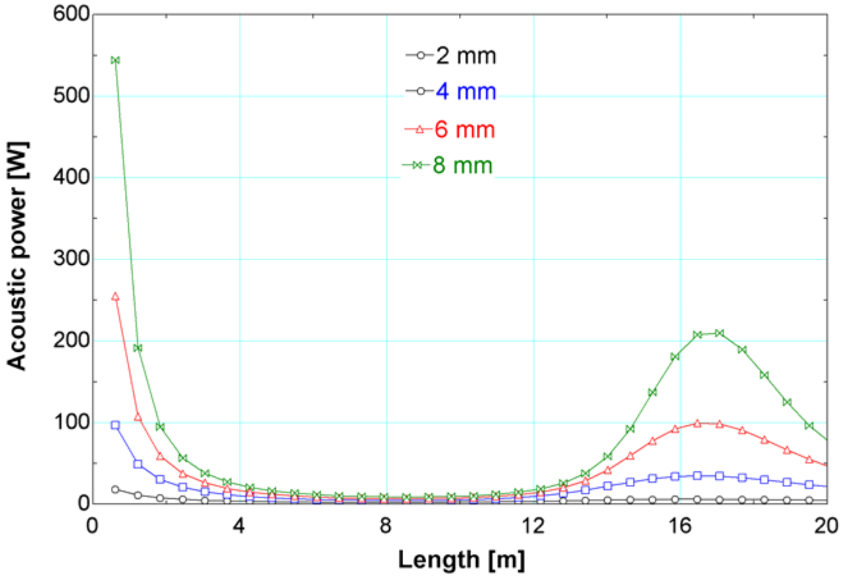

Figure 6.4 Acoustic power as a function of inertance length for various diameters at 30 Hz, a pressure ratio of 1.1, and a mean pressure of 25 bars.

Figures 6.3 and 6.4 can be used to select an inertance tube geometry for a desired phase shift and a given acoustic power. However, they are not convenient. For example, if the desired phase shift is -60° and the acoustic power is about 18 W, Figure 6.3 provides 3 different possible diameter/length combinations that satisfy the phase requirement: 4 mm at 10 ft, 6 mm at 22 ft, and 8 mm at 24 ft. These geometries must be evaluated in Figure 6.4 to determine which combination provides the correct acoustic power; it can be seen that only the 4 mm at 10 ft combination provides the desired acoustic power. Considerable iteration between Figures 6.3 to 6.4 might be necessary when interpolation between diameters and lengths is required in cases where the desired phase and acoustic power don't line up precisely with the curves.

A more convenient presentation format would show both acoustic power and phase information on the same figure. Figure 6.5 illustrates contours of constant length and constant diameter in the space of acoustic power (plotted on a logarithmic scale) and phase. Diameters (inner diameter) ranging from 2 mm to 24 mm in 2mm increments are plotted in Figure 6.5 as the lighter curves and lengths ranging from 2 ft to 70 ft are shown by the heavy, solid curves. Numbers on the constant length curves indicate the length in feet.

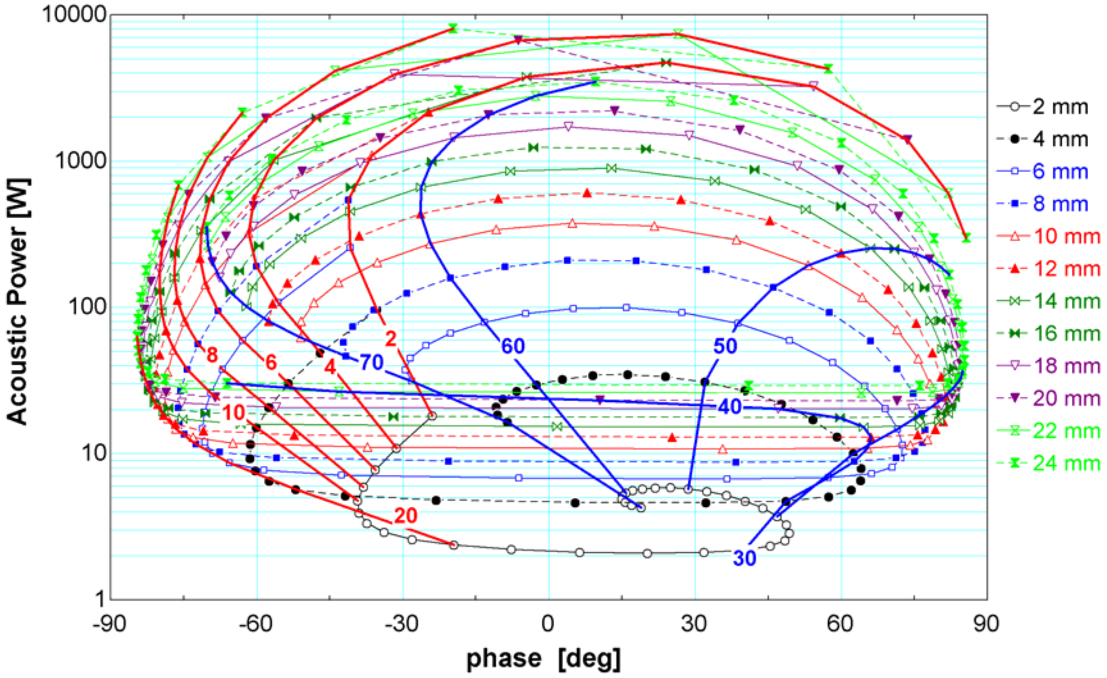

Figure 6.5 Contours of constant length and constant diameter shown in the space of acoustic power and phase (assuming an operating frequency of 30 Hz, a pressure ratio of 1.1, and a 7.8 liter reservoir volume).

There are a few interesting things to notice in Figure 6.5. The cyclic nature of the phase as a function of the length (see Figure 6.3) shows up in Figure 6.5 in the fact that the constant length contours progress back-and-forth across the figure as length is increased. As a result of this oscillating behavior there are regions of acoustic power and phase that are unattainable to the pulse tube designer; a very low power pulse tube, for example one requiring 5 W of acoustic power, could not expect to achieve a phase less than about -45 degrees. Smaller power pulse tubes would be even more limited in terms of their phase. While there are some combinations of acoustic power and phase that are unattainable for any inertance tube geometry, there are others that can be obtained using more than one geometry. For example, Figure 6.5 shows that both a 4 ft long, 4 mm diameter inertance tube and a 70 ft long, 9 mm diameter inertance tube will yield an acoustic power of approximately 30 W and a phase of approximately -50 degree. It seems likely that the shorter/smaller inertance tube would be more attractive.

To facilitate using the design chart, Figure 6.6 and 6.7 shows an expanded view of the range of phase angle that is most relevant for pulse tube designs. Inner diameter contours are shown from 2 mm to 30 mm in 2 mm increments. The smallest diameter corresponds to the smallest acoustic powers; with increasing diameter, the acoustic power increases. Relevant lengths are spaced in 2 feet increments. Figure 6.6 focuses on short tube lengths and Figure 6.7 on long lengths. Lines of constant lengths and diameters seem to mesh a surface that corresponds to half of an oblate ellipsoid of revolution.

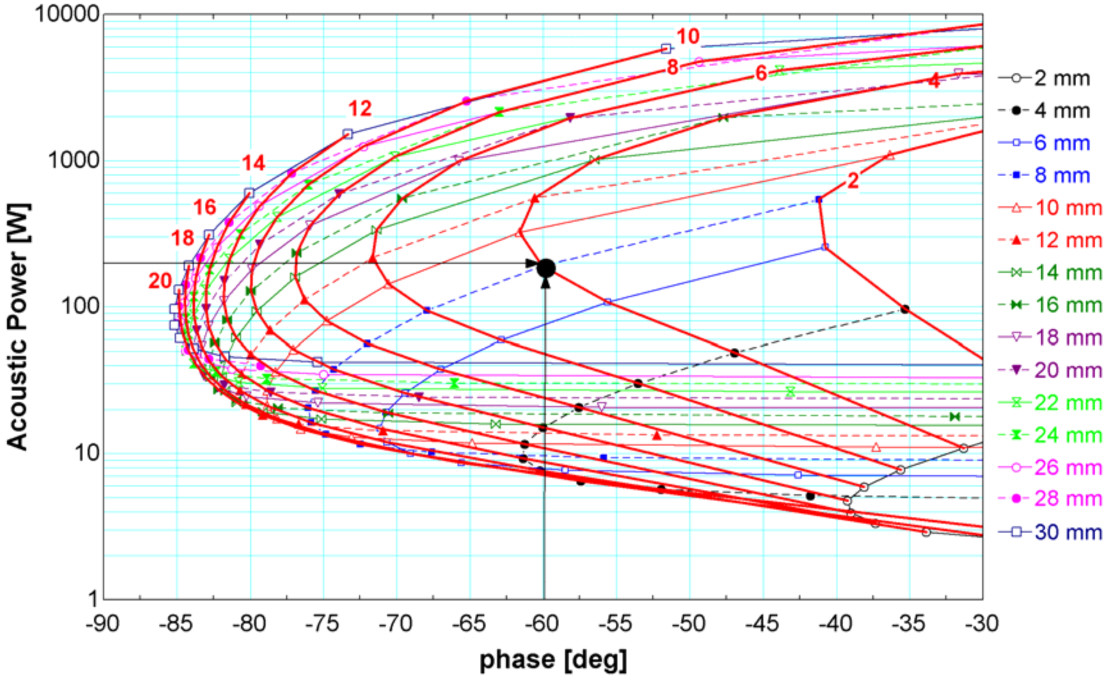

Figure 6.6 Inertance tube design chart at 30 Hz and 1.1 pressure ratio and 7.8 liter reservoir volume for short inertance tubes

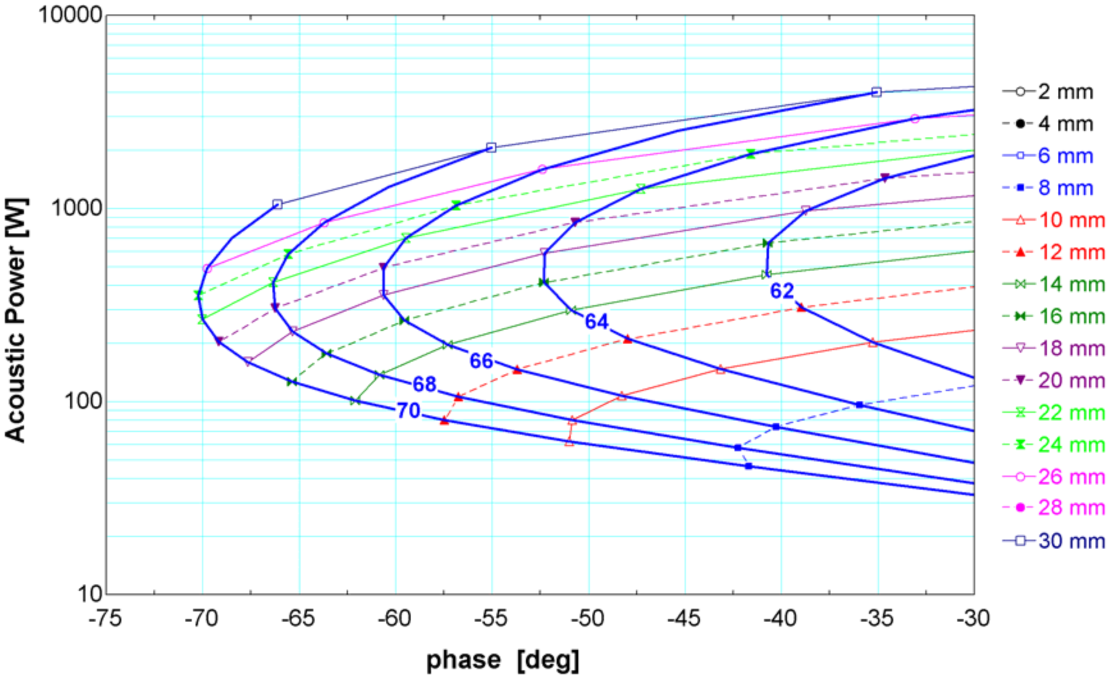

Figure 6.7 Inertance tube design chart at 30 Hz and 1.1 pressure ratio and 7.8 liter reservoir volume for long inertance tubes

An example how to use the design chart is also indicated in Figure 6.6. If the acoustic power is 200 W and the desired phase is -60°, the intersection of the constant acoustic power line (200 W) and the constant phase line (-60°) can be used to obtain the required length and diameter of the inertance tube. In this example an inertance tube of 4 feet length and 8 mm inner diameter should be used.

More design charts are presented in the next section for frequencies of 30 Hz, 40 Hz, and 50 Hz and pressure ratios ranging from 1.1 to 1.4.

6.3 More design charts

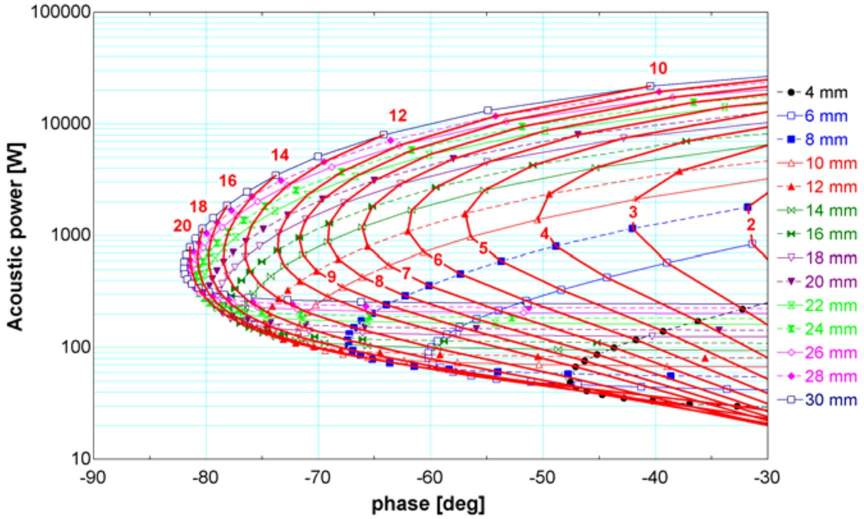

Figure 6.8 Inertance tube design chart at 30 Hz and 1.2 pressure ratio and 7.8 liter reservoir volume for short inertance tubes. Bold lines represent various lengths

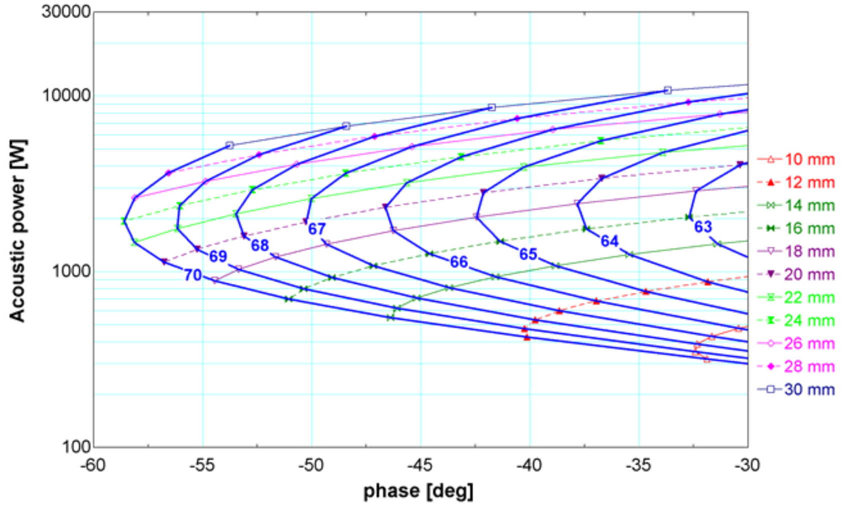

Figure 6.9 Inertance tube design chart at 30 Hz and 1.2 pressure ratio and 7.8 liter reservoir volume for long inertance tubes. Bold lines represent various lengths

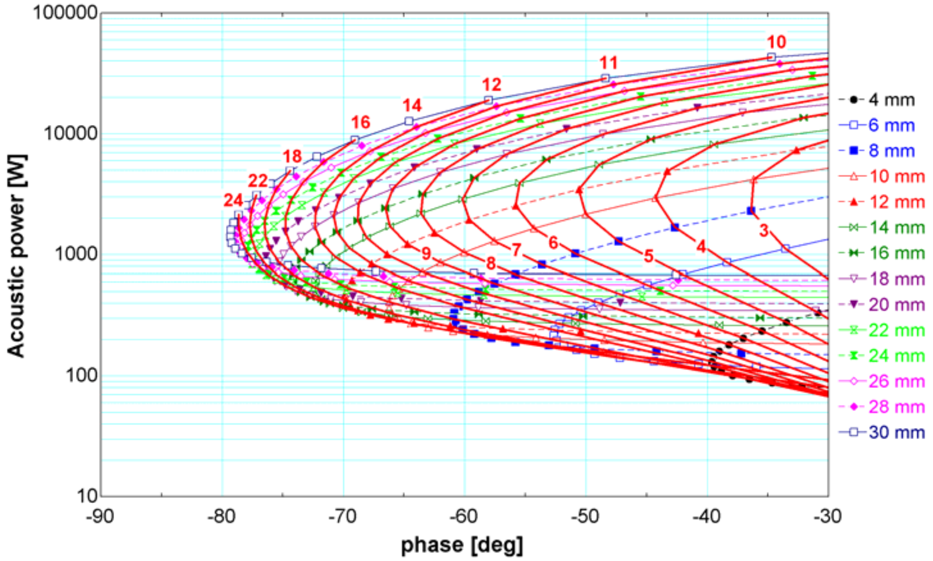

Figure 6.10 Inertance tube design chart at 30 Hz and 1.3 pressure ratio and 7.8 liter reservoir volume for short inertance tubes. Bold lines represent various lengths

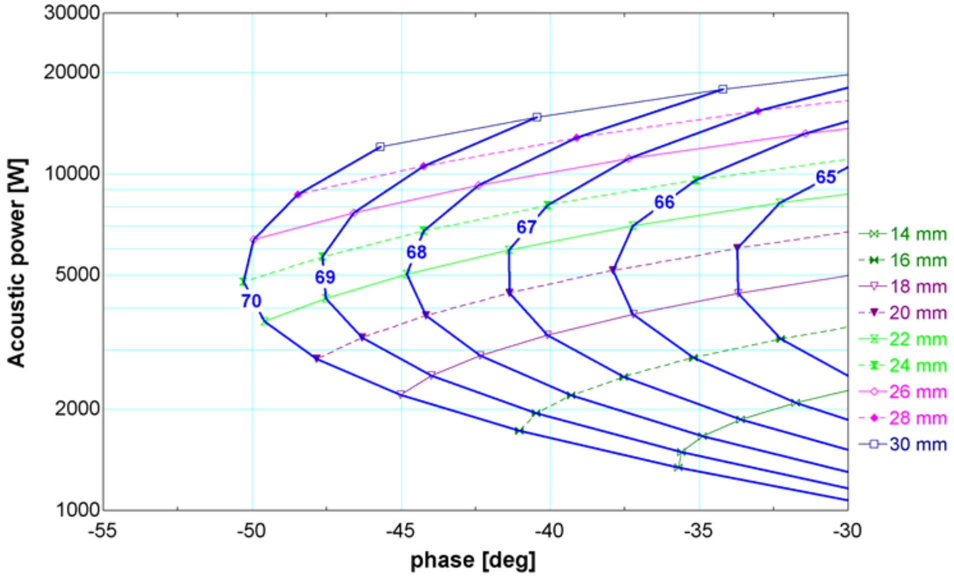

Figure 6.11 Inertance tube design chart at 30 Hz and 1.3 pressure ratio and 7.8 liter reservoir volume for long inertance tubes. Bold lines represent various lengths

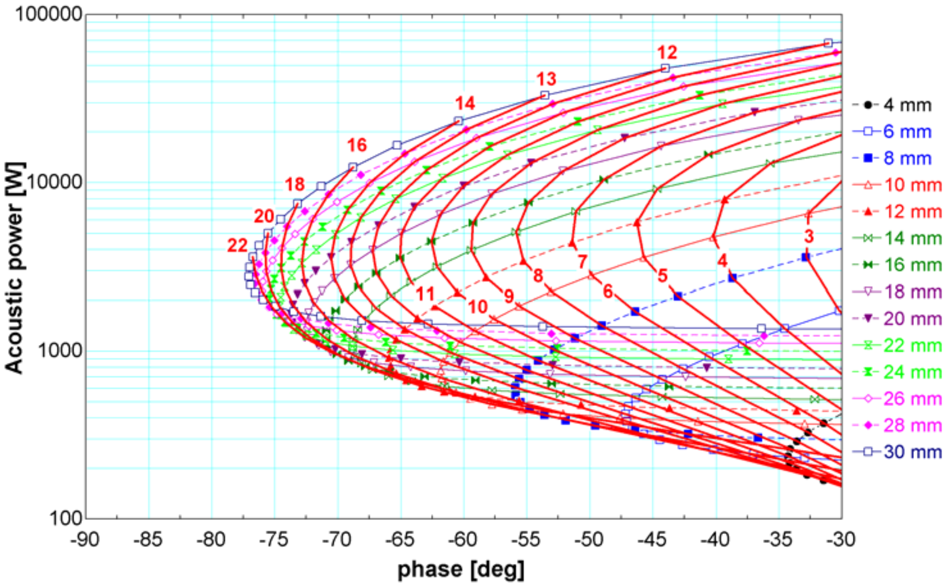

Figure 6.12 Inertance tube design chart at 30 Hz and 1.4 pressure ratio and 7.8 liter reservoir volume for short inertance tubes. Bold lines represent various lengths

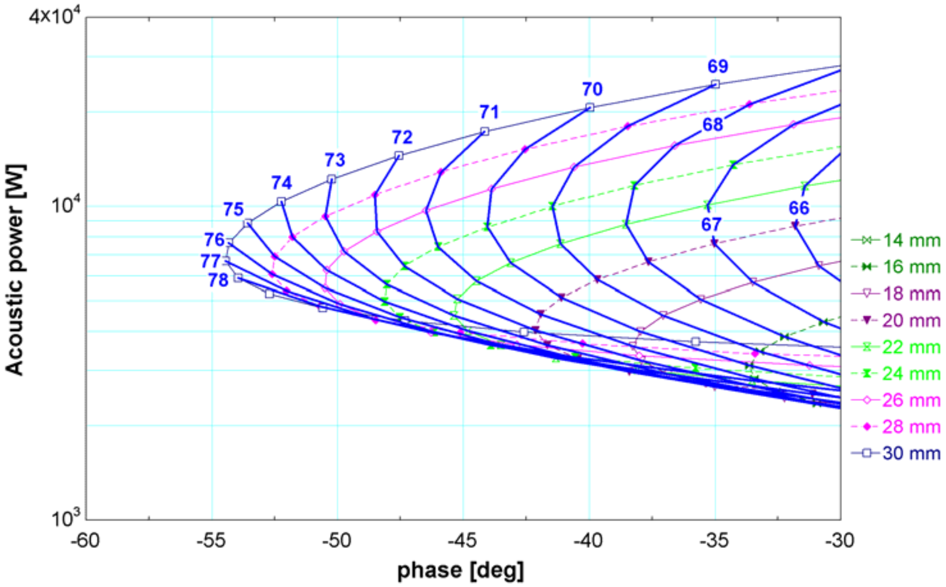

Figure 6.13 Inertance tube design chart at 30 Hz and 1.4 pressure ratio and 7.8 liter reservoir volume for long inertance tubes. Bold lines represent various lengths

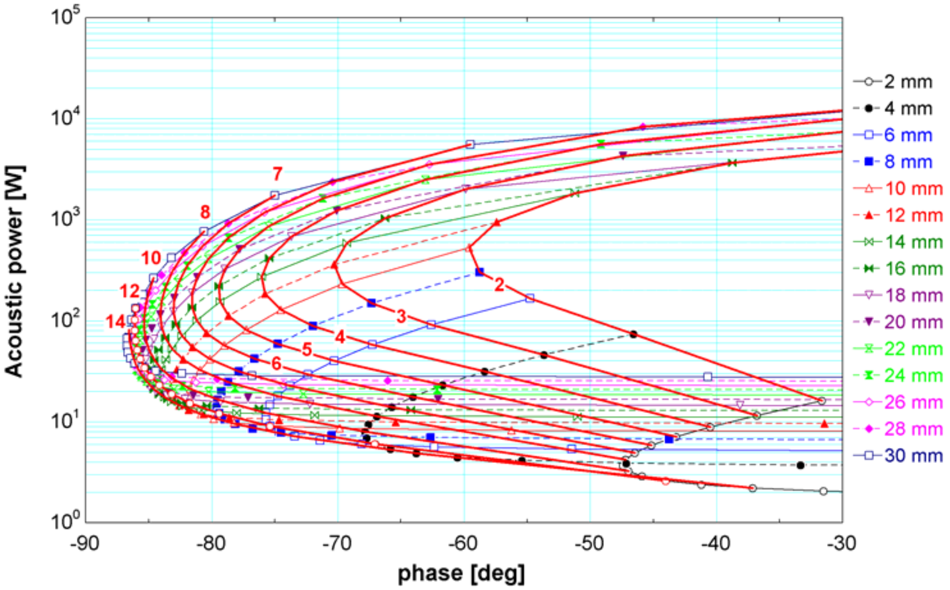

Figure 6.14 Inertance tube design chart at 40 Hz and 1.1 pressure ratio and 7.8 liter reservoir volume for short inertance tubes. Bold lines represent various lengths

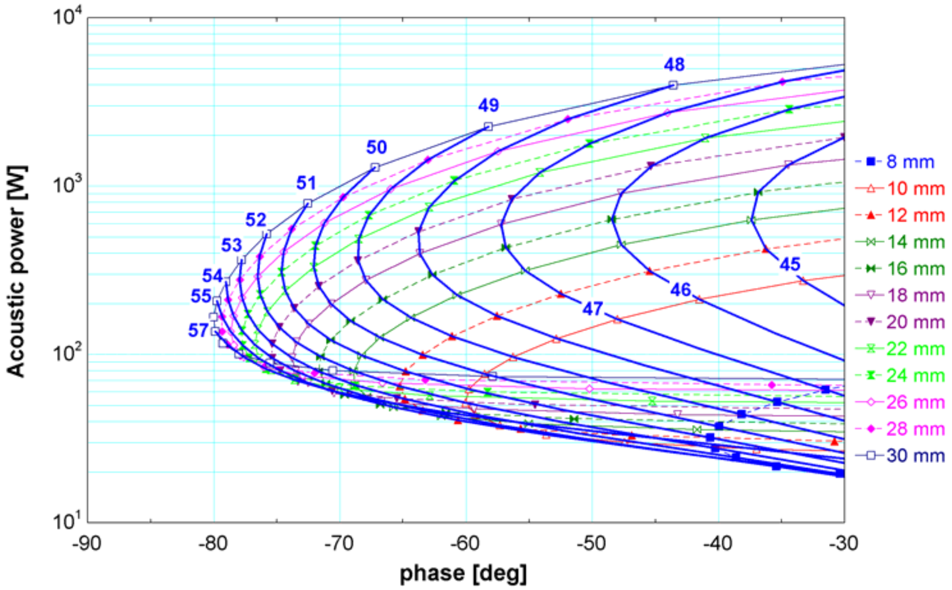

Figure 6.15 Inertance tube design chart at 40 Hz and 1.1 pressure ratio and 7.8 liter reservoir volume for intermediate inertance tubes. Bold lines represent various lengths

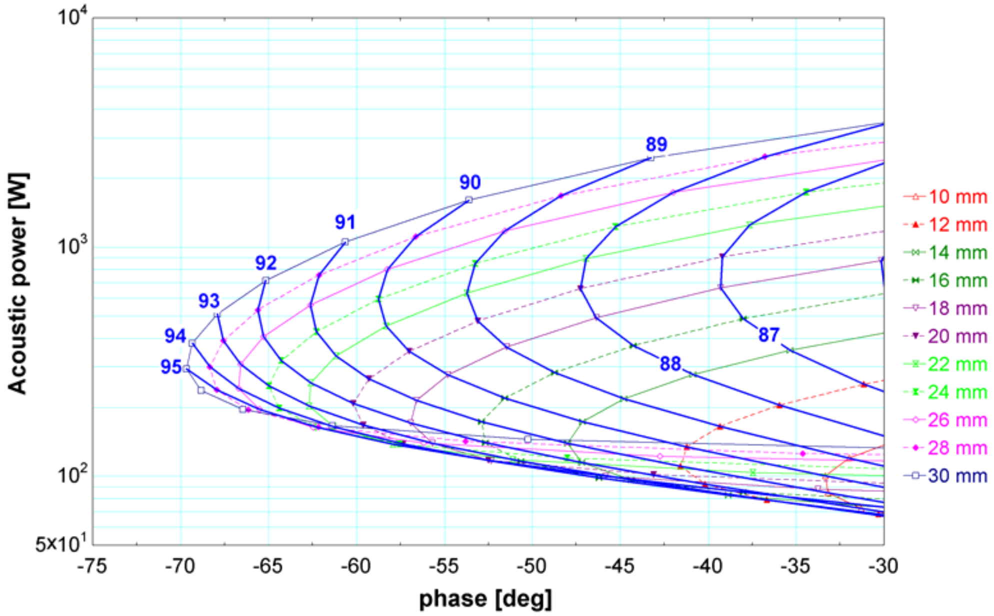

Figure 6.16 Inertance tube design chart at 40 Hz and 1.1 pressure ratio and 7.8 liter reservoir volume for long inertance tubes. Bold lines represent various lengths

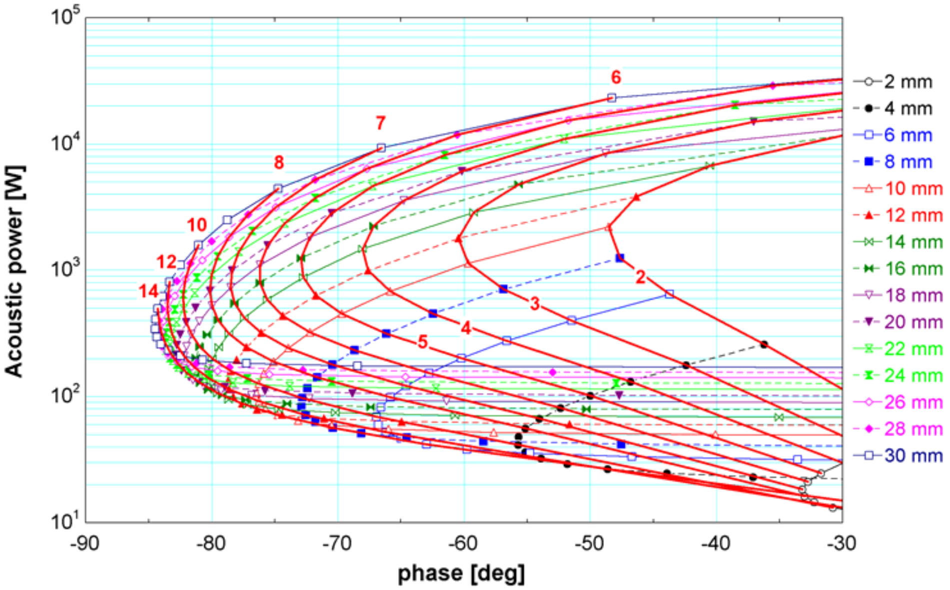

Figure 6.17 Inertance tube design chart at 40 Hz and 1.2 pressure ratio and 7.8 liter reservoir volume for short inertance tubes. Bold lines represent various lengths

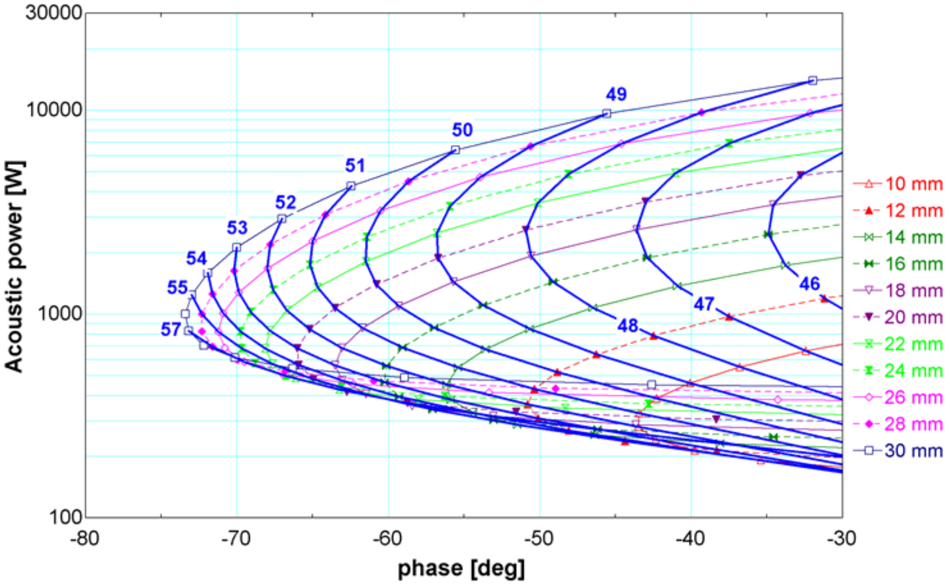

Figure 6.18 Inertance tube design chart at 40 Hz and 1.2 pressure ratio and 7.8 liter reservoir volume for intermediate inertance tubes. Bold lines represent various lengths

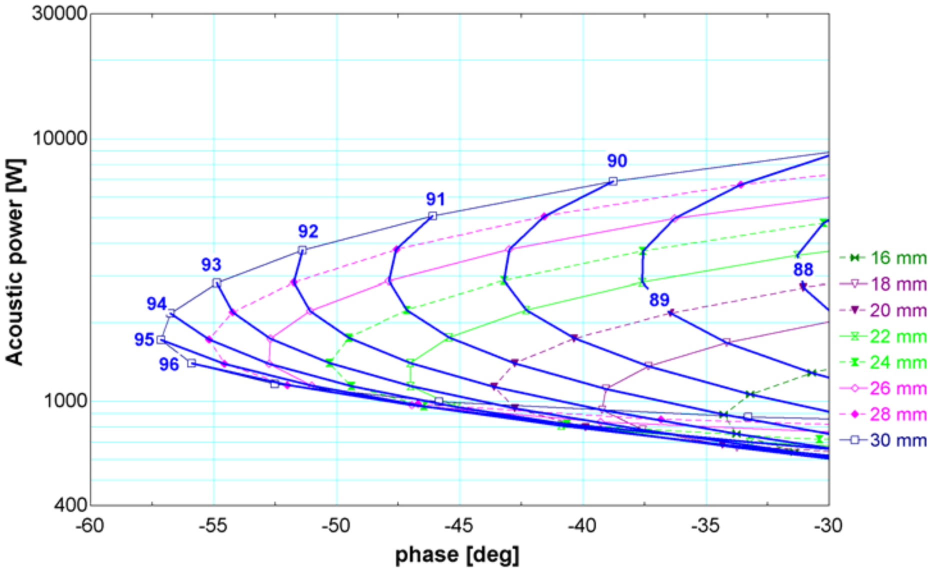

Figure 6.19 Inertance tube design chart at 40 Hz and 1.2 pressure ratio and 7.8 liter reservoir volume for long inertance tubes. Bold lines represent various lengths

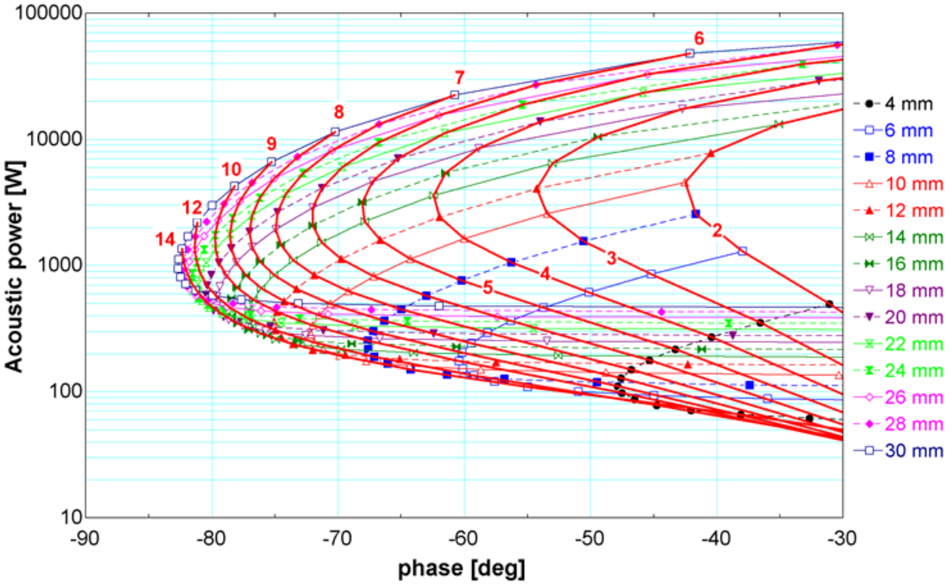

Figure 6.20 Inertance tube design chart at 40 Hz and 1.3 pressure ratio and 7.8 liter reservoir volume for short inertance tubes. Bold lines represent various lengths

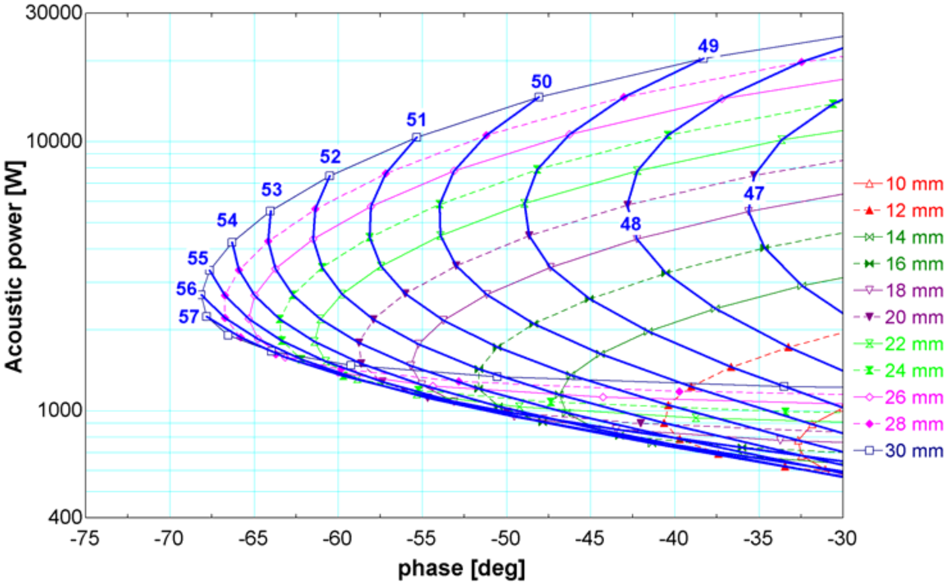

Figure 6.21 Inertance tube design chart at 40 Hz and 1.3 pressure ratio and 7.8 liter reservoir volume for intermediate inertance tube. Bold lines represent various lengths

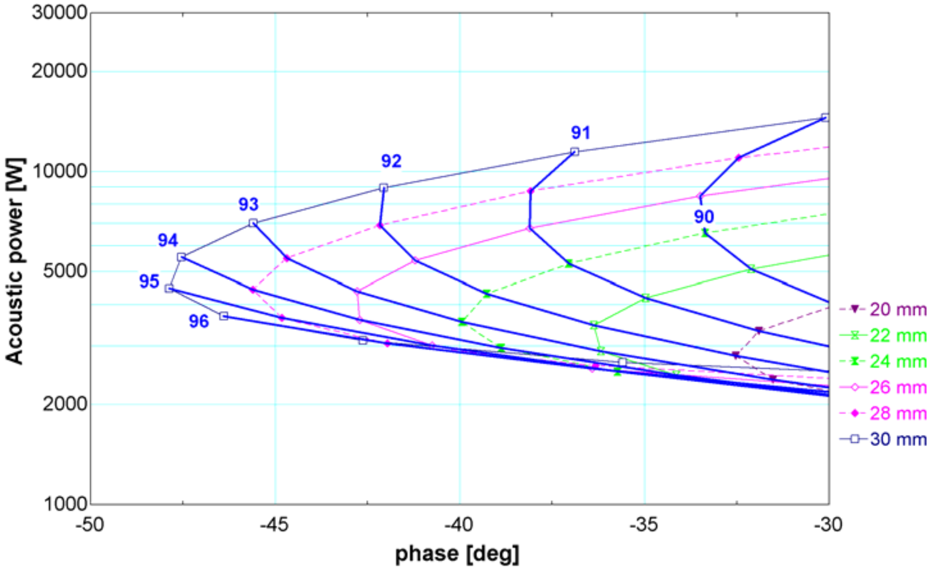

Figure 6.22 Inertance tube design chart at 40 Hz and 1.3 pressure ratio and 7.8 liter reservoir volume for long inertance tubes. Bold lines represent various lengths

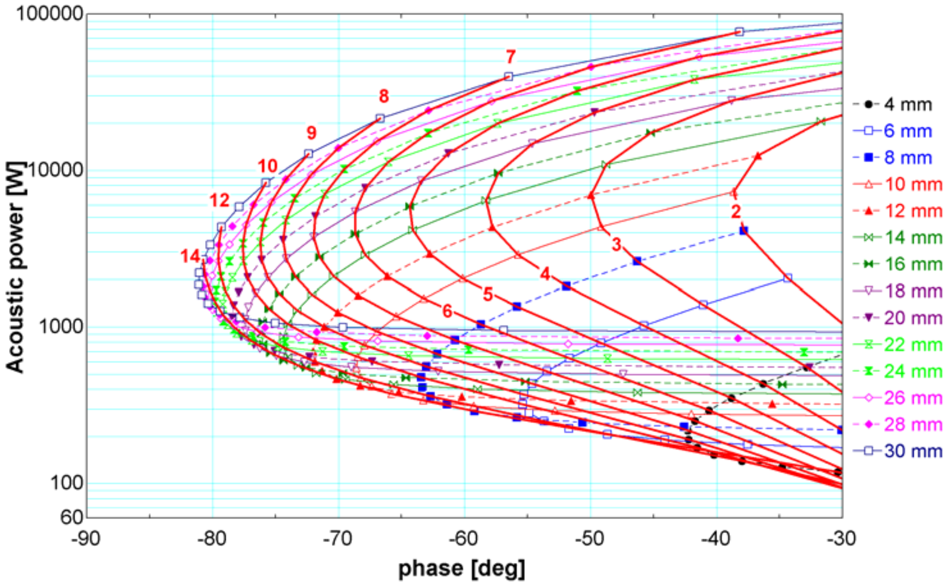

Figure 6.23 Inertance tube design chart at 40 Hz and 1.4 pressure ratio and 7.8 liter reservoir volume for short inertance tubes. Bold lines represent various lengths

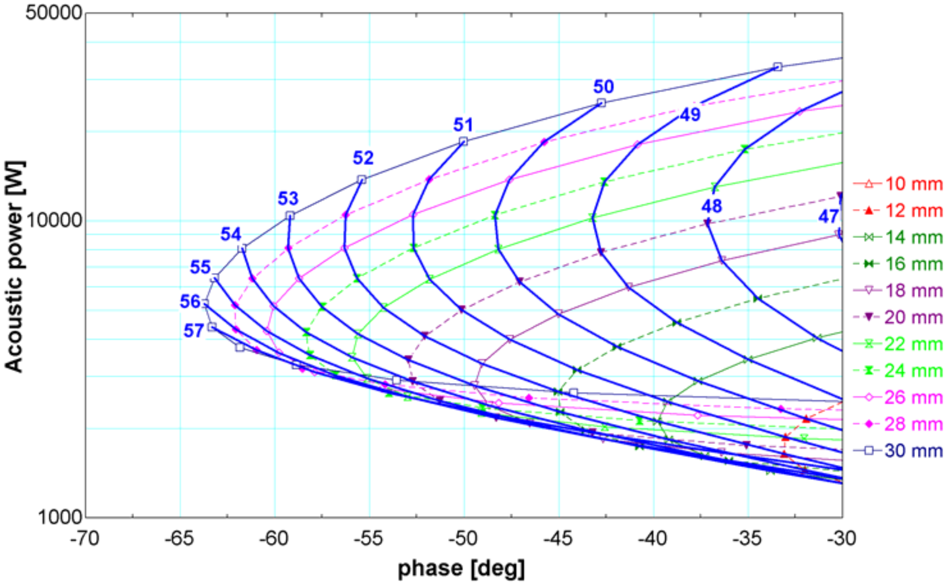

Figure 6.24 Inertance tube design chart at 40 Hz and 1.4 pressure ratio and 7.8 liter reservoir volume for intermediate inertance tube. Bold lines represent various lengths

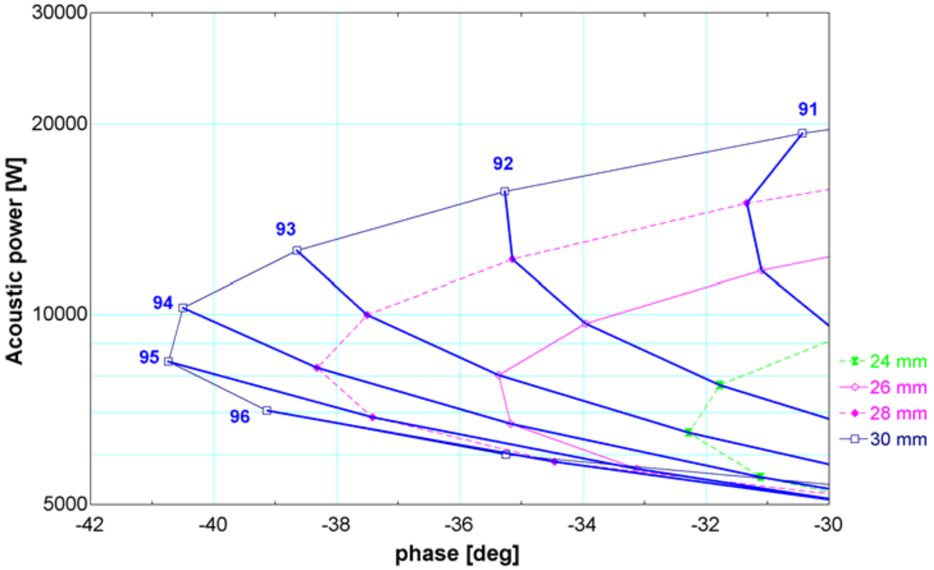

Figure 6.25 Inertance tube design chart at 40 Hz and 1.4 pressure ratio and 7.8 liter reservoir volume for long inertance tubes. Bold lines represent various lengths

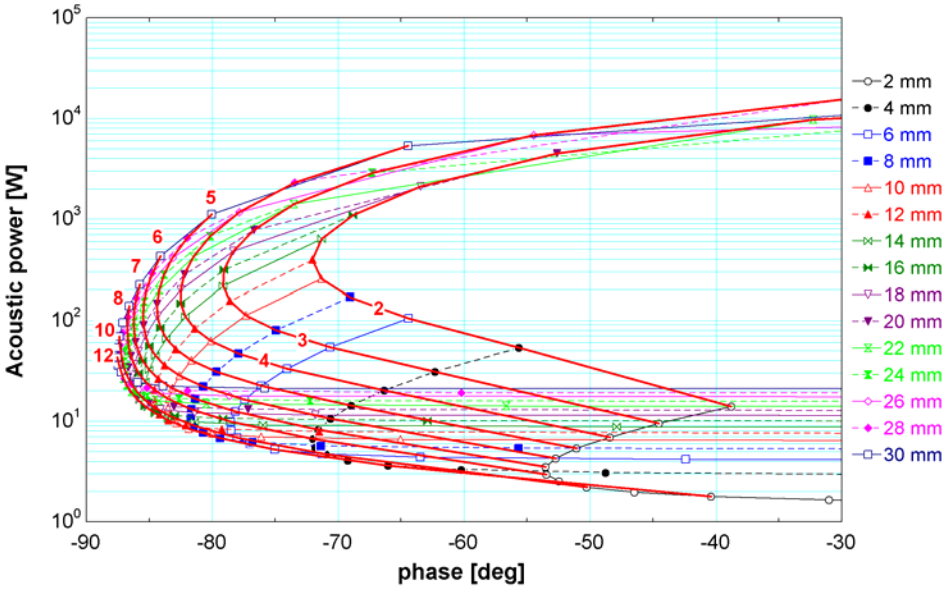

Figure 6.26 Inertance tube design chart at 50 Hz and 1.1 pressure ratio and 7.8 liter reservoir volume for short inertance tubes. Bold lines represent various lengths

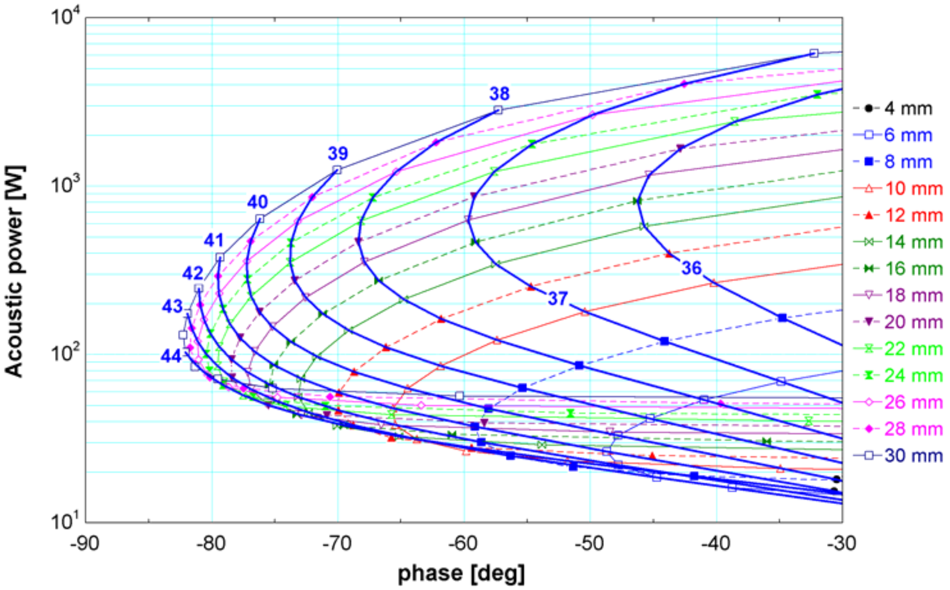

Figure 6.27 Inertance tube design chart at 50 Hz and 1.1 pressure ratio and 7.8 liter reservoir volume for intermediate inertance tube. Bold lines represent various lengths

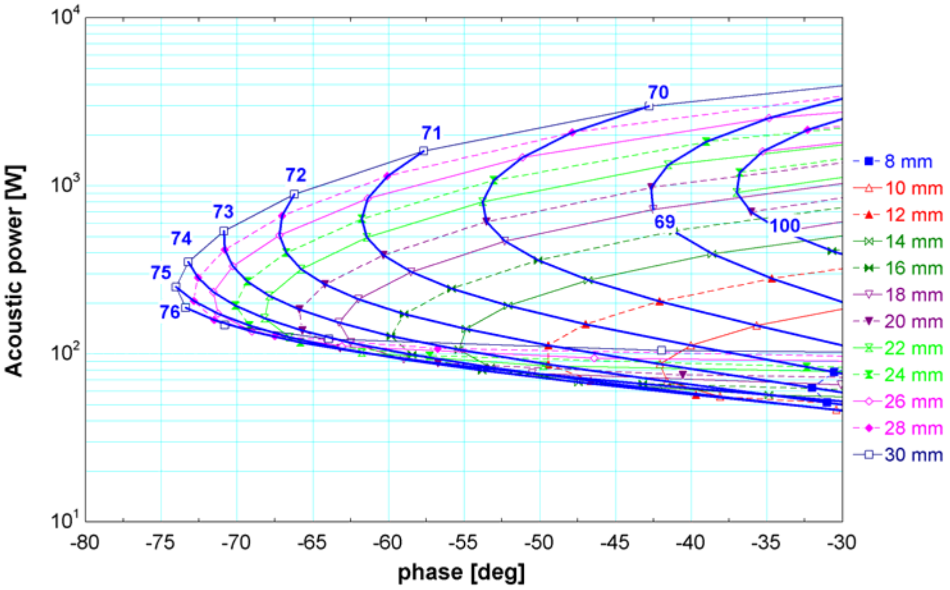

Figure 6.28 Inertance tube design chart at 50 Hz and 1.1 pressure ratio and 7.8 liter reservoir volume for long inertance tubes. Bold lines represent various lengths

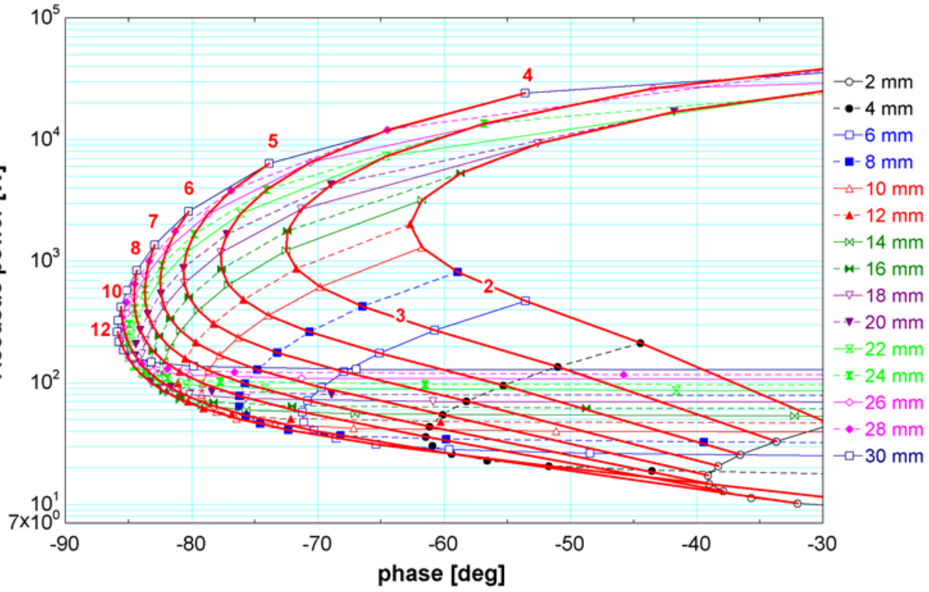

Figure 6.29 Inertance tube design chart at 50 Hz and 1.2 pressure ratio and 7.8 liter reservoir volume for short inertance tubes. Bold lines represent various lengths

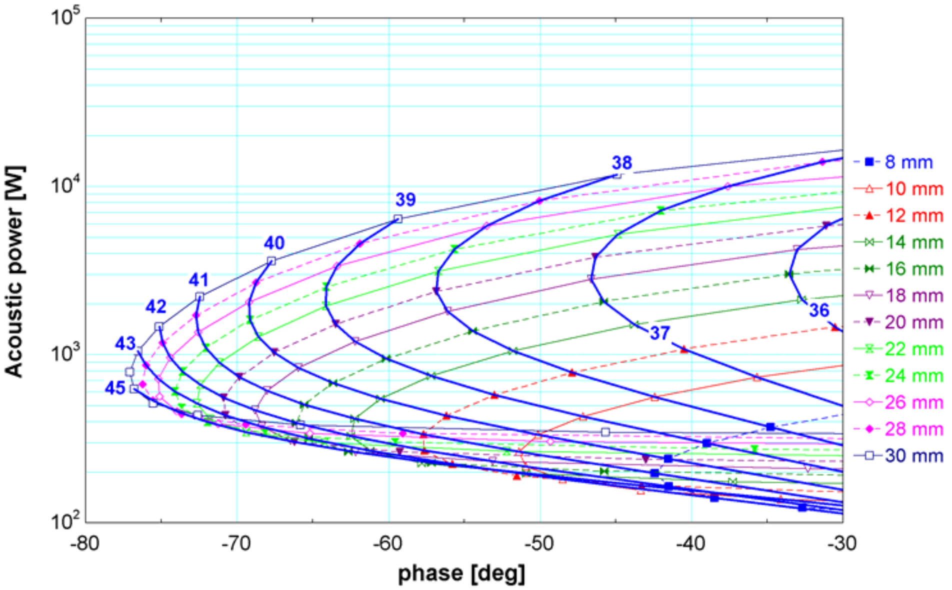

Figure 6.30 Inertance tube design chart at 50 Hz and 1.2 pressure ratio and 7.8 liter reservoir volume for intermediate inertance tube. Bold lines represent various lengths

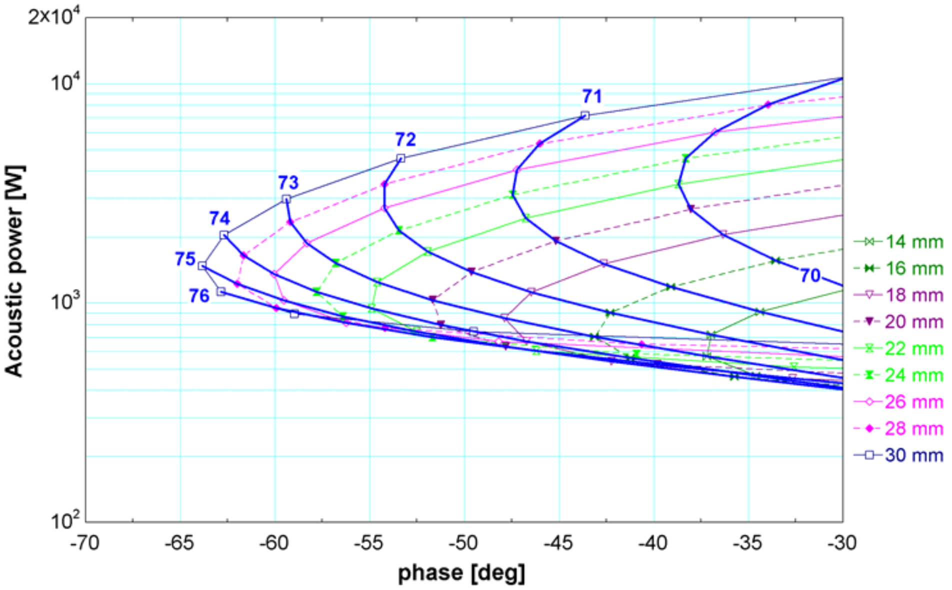

Figure 6.31 Inertance tube design chart at 50 Hz and 1.2 pressure ratio and 7.8 liter reservoir volume for long inertance tubes. Bold lines represent various lengths

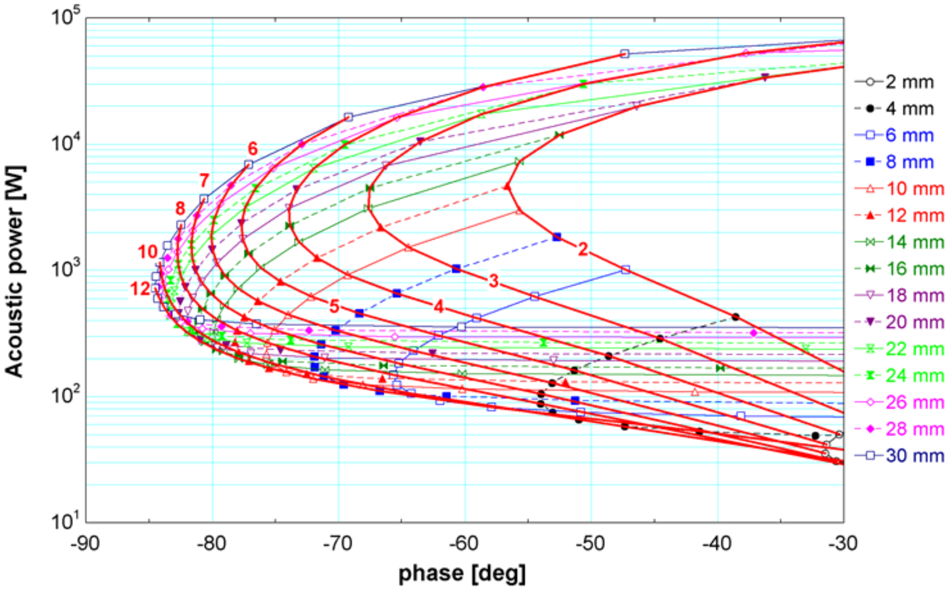

Figure 6.32 Inertance tube design chart at 50 Hz and 1.3 pressure ratio and 7.8 liter reservoir volume for short inertance tubes. Bold lines represent various lengths

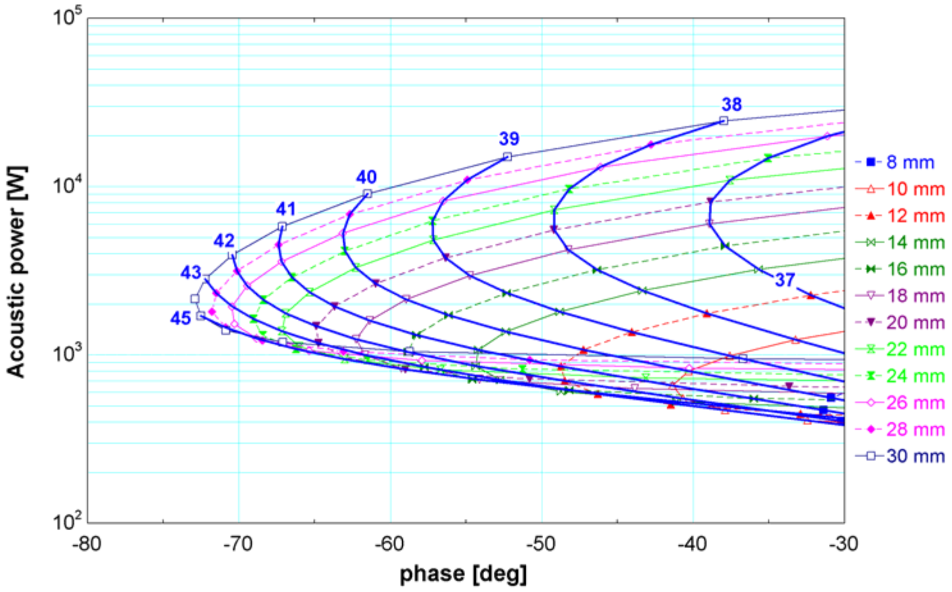

Figure 6.33 Inertance tube design chart at 50 Hz and 1.3 pressure ratio and 7.8 liter reservoir volume for intermediate inertance tube. Bold lines represent various lengths

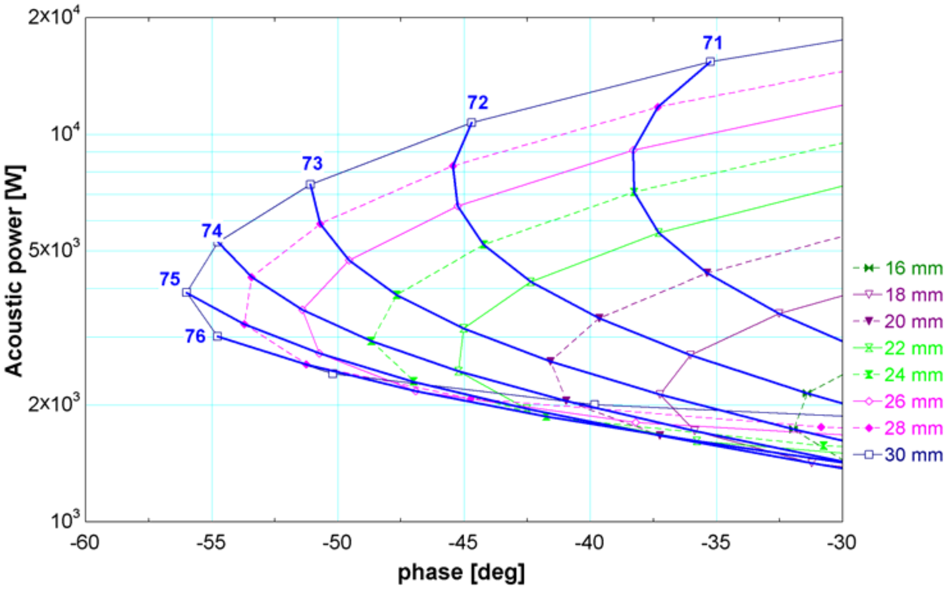

Figure 6.34 Inertance tube design chart at 50 Hz and 1.3 pressure ratio and 7.8 liter reservoir volume for long inertance tubes. Bold lines represent various lengths

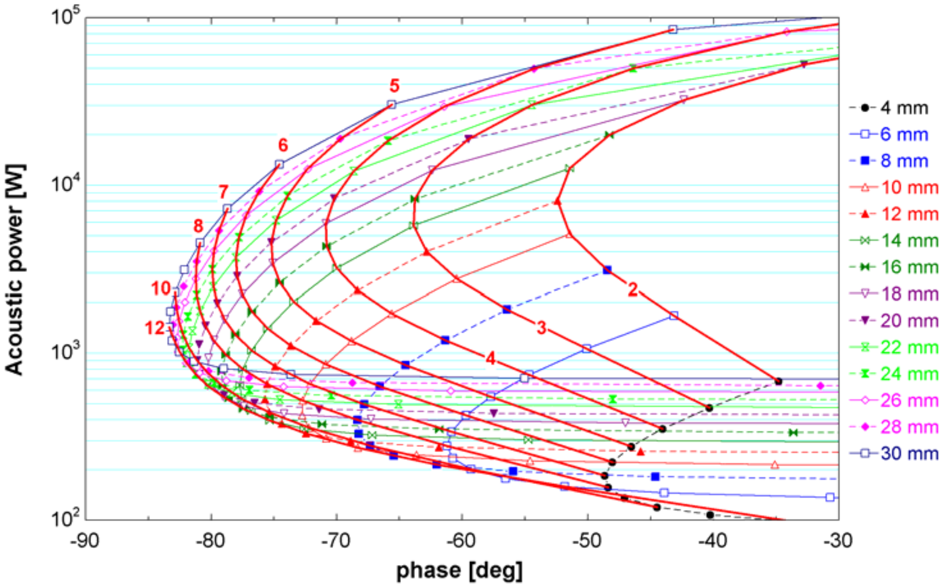

Figure 6.35 Inertance tube design chart at 50 Hz and 1.4 pressure ratio and 7.8 liter reservoir volume for short inertance tubes. Bold lines represent various lengths

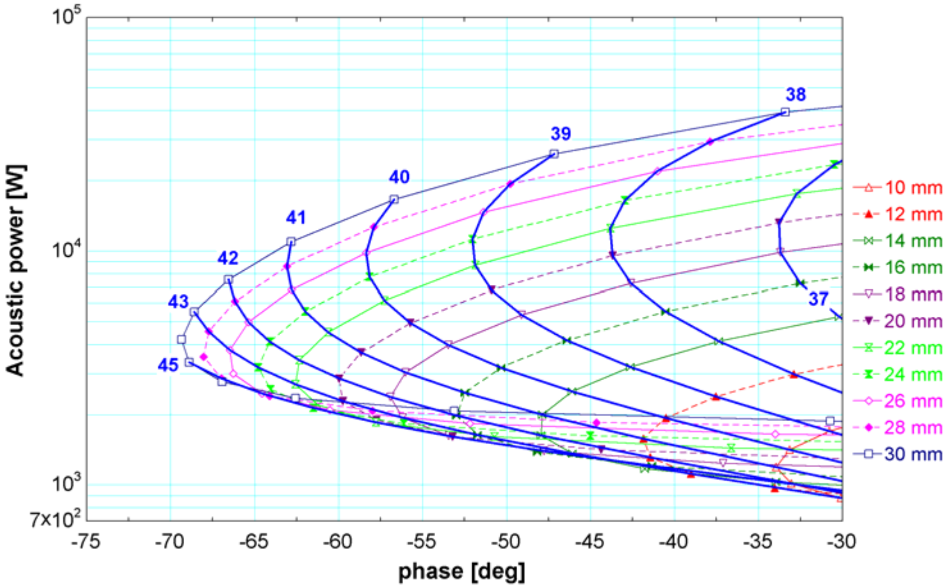

Figure 6.36 Inertance tube design chart at 50 Hz and 1.4 pressure ratio and 7.8 liter reservoir volume for intermediate inertance tube. Bold lines represent various lengths

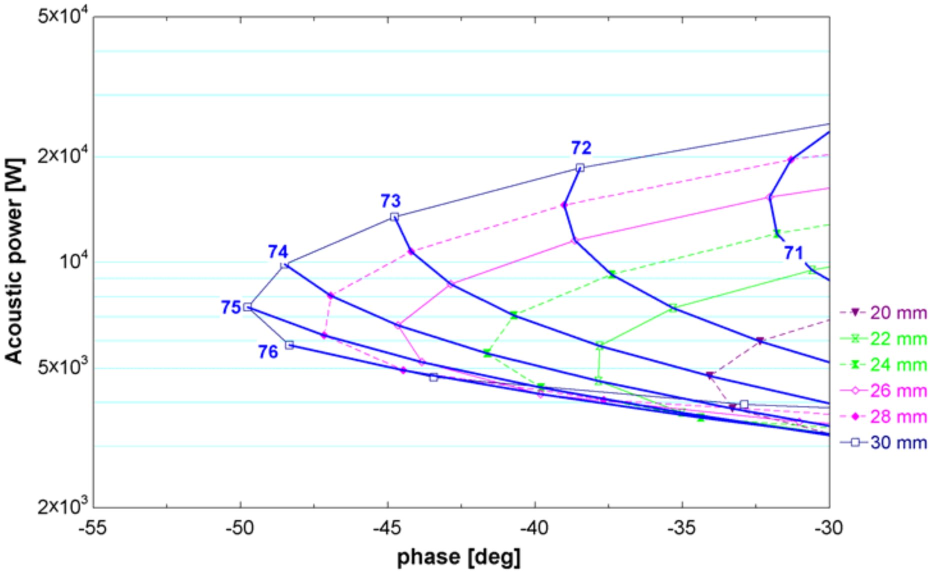

Figure 6.37 Inertance tube design chart at 50 Hz and 1.4 pressure ratio and 7.8 liter reservoir volume for long inertance tubes. Bold lines represent various lengths

CONCLUSIONS

Three models describing and predicting the inertance effect in inertance tubes for pulse tube refrigerators have been developed. Each model is capable of predicting the phase and mass flow at the inertance tube inlet. The transmission line model determines the complex impedance of the inertance tube and reservoir network by defining the characteristic impedance of the inertance tube, the impedance of the reservoir and the attenuation and propagation of pressure and mass flow rate in the tube. The lumped component model is more physically intuitive and treats the inertance tube and the reservoir as a simple network of four lumped electrical components that represent the resistance, compliance, and inertia of the tube and the compliance of the reservoir. The distributed component model divides the inertance tube into n increments and therefore yields essentially the same predictions as the transmission line model when a large number of increments are used. However, the advantage of the distributed model over the transmission line model is its ability to model the axial variation in the resistance of the inertance tube due to the variation in the mass flow rate variation along the tube. Also, the distributed component model is capable of including the fluid resistance associated with contraction/expansion at the interface between the reservoir and the inertance tube. The distributed component model is considered to be the most attractive of the three models and this model was subsequently verified experimentally.

Several attempts were made to measure the large, high frequency, high pressure mass flow rate into the inertance tube. A commercially available mass flow sensor based on hot film anemometry was packaged and integrated with a bypass tube in order to allow operation at the high pressures and flow rates required by the experiment. However, careful testing showed that the sensor exhibits abnormal behavior under oscillating flow conditions and therefore could not be used. Two methods of indirectly measuring the mass flow into the inertance tube using the principle of mass conservation in the compressor space were implemented. The first method assumed isothermal compression/expansion processes and the second method experimentally determined the best polytropic exponent to use for these processes. Both methods were capable of predicting the mass flow rate under certain operating conditions when no inertance tube was attached to the compressor. However, these methods failed to accurately predict the mass flow rate and its phase with respect to the inlet pressure when an inertance tube was connected.

Finally, the model was verified through an extensive comparison between the predicted and measured values of the time varying mass flow rate into the reservoir (calculated from the reservoir pressure) and the excellent pressure agreement with the distributed component model predictions.

Finally, the verified model was used to develop design charts for compressor frequencies of 30, 40, and 50 Hz at pressure ratios ranging from 1.1 to 1.4. These charts allow the pulse tube designer to conveniently specify the inertance tube geometry that will yield a desired acoustic power and phase. Examination of the design curves showed that there are regions of operation, very small acoustic powers and large, negative phase, that cannot be obtained by any inertance tube geometry. There are other regions where multiple combinations of length and diameter can be used to obtain a given phase and acoustic pressure.

REFERENCES

[1] Radebaugh R., *Australian Refrigeration, Air Conditioning, and Heating Journal*, vol. **55**, no. 2, pp. 22-29; vol. **55**, no. 3, pp. 21-27, (2001)

[2] Mikulin E.I., Tarasov A.A., Shrebyonock M.P., "Low-temperature expansion pulse tube," in *Advances on Cryogenic Engineering* **29**, edited by R.W. Fast, Plenum, New York, 1984, pp. 629-637.

[3] Zhu S, Wu P., Chen Z., *Crogenics* **30**, pp. 514-520 (1990)

[4] Marquardt, E.D., Radebaugh, R., Adv. Cryogenic Engr. **45**, Plenum, NY 2001, pp. 457-464.

[5] Kanao K., Watanabe N. Kanazawa Y., *Cryogenics* **34**, supplement: 167 (1994)

[6] Roach P.R., Kashani A., "Pulse tube coolers with an inertance tube: theory, modeling and practice" in *Advances on Cryogenic Engineering* **43B**, edited by P. Kittel, Plenum, New York, 1997, pp.1895-1902.

[7] Luo, E., Radebaugh R., Lewis, M., "Inertance tube models and their experimental verification" in *Advances on Cryogenic Engineering* **43**

[8] Radebaugh, R., “Pulse Tube Cryocoolers,” in *Low Temperature and Cryogenic Refrigeration*, edited by S. Kakac, H.F. Smirnov, and M.R. Avelino, Kluwer Academic Publishers, Dordrecht, 2003, pp. 415-434.

[9] Rohmann, C.P., Grogan E.C., "On the dynamics of pneumatic transmission lines", Transactions of the ASME, May 1957, pp 853-874

[10] Incropera, F.P., DeWitt, D.P., *Introduction to Heat Transfer*, John Wiley & Sons, New York, 2002, Chapter 8 and 11.

[11] Skilling, H.H., *Electric Transmission Lines*, McGraw-Hill, New York, Toronto, London, 1951, Chapter 1-4.

[12] Kays, W.M., London A.L., *Compact Heat Exchangers*, McGraw-Hill, New York, Toronto, London, 1964, Chapter 1.

[13] Ju Y.L., He G.Q., Hou Y.K., Liang J.T, Zhou Y., *Cryogenics* **43**, pp.1-7 (2003)

[14] Beitz, W., Grothe, K.-H., *Dubbel Taschenbuch fuer den Maschinenbau*, 19. Auflage, Spinger, Berlin, 1997 pp. P5

APPENDIX A

```
"=================================================================="
"            Transmission line model                                                     "
"=================================================================="

$Bookmark Input Parameters

"frequency"
f=10.81"[Hz]"
"dynamic pressure amplitude"
P_pt=2.08*10^5
"average pressure"
P_0=10.14*10^5
"working fluid"
GAS$='Helium'
"gas temperature"
T=293.0 "[K]"
"reservoir volume"
Vr_r=0.00378 [m^3]
Vr_i=0
"surface roughness"
rough=3.0*10^(-6)"[m]"
"Complex number i"
i_i=1
i_r=0

$Bookmark Assumed Inertance Size

D_i=0
D_r=.311*convert(inch,m) "[m]"
x_i=0
x_r=45*convert(ft,m) "[m]"

$Bookmark Gas Properties

"universal gas constant"
R_un=R#*convert(kJ,J)
"molecular weight"
MW=molarmass(GAS$)
"ideal gas constant"
R=R_un/MW "[J/kg-K]"
"specific heat ratio"
gamma=cP(GAS$,T=T,P=P_0_r)/cV(GAS$,T=T,P=P_0_r)
"density"
rho=P_0_r/(R*T)  "[kg/m^3]"
"viscosity"
mu=viscosity(GAS$,T=T,P=P_0_r) "[kg/m-s]"
"heat capacity"
cp=gamma*R/(gamma-1) "[J/kg-K]"
"gas thermal conductivity"
lambda=CONDUCTIVITY(Helium,T=T,P=P_0_r) "[W/m-K]"
```

```
$Bookmark Resistance Calculations

"mass flow rate"
m_dot=2*P_0_r*W_dotpt/(R*T*P_pt_r*cos(theta_rZ_x_D)) "[kg/s]"
"Reynolds number"
Nr=8*m_dot/(pi^2*mu*D)
"friction factor"
fr=0.046*Nr^(-0.2)
"resistance/length"
r_D=(64*fr*m_dot/(pi^3*rho*D^5))"[1/m^2-s]"

$Bookmark Impedance Parameters

"angular frequency"
omega=2*pi*f"[1/s]"
"inertance/length"
l_D=(4/(pi*D^2))"[1/m^2]"
"compliance/length"
c_D=(pi*D^2/(4*gamma*R*T))"[s^2]"
"reservoir compliance"
Cr=(Vr/(gamma*R*T))"[m*s^2]"
"load (reservoir) impedance"
(Zr)=(1/(i*omega*Cr)) "[m^(-1)*s^(-1)]"
"characteristic impedance"
(Zo_D)=(((r_D+i*omega*l_D)/(i*omega*c_D))^(1/2))"[1/m-s]"
"propagation factor"
zeta_D=((r_D+i*omega*l_D)*i*omega*c_D)^(1/2)"[m^(-1)]"
"reflection factor"
(K_D)=((Zr-Zo_D)/(Zr+Zo_D))
"attenuation factor"
alpha_D=Real(zeta_D)"[m^(-1)]"
"phase factor"
beta_D=Imag(zeta_D)"[m^(-1)]"
"impedance of line and load"
Z_x_D=((Zo_D*(Zr+Zo_D*tanh(zeta_D*x_r))/(Zo_D+Zr*tanh(zeta_D*x_r))))"[1/m-s]"
"phase of impedance"
theta_rZ_x_D=AngleRad((Z_x_D))"[rad]"
"magnitude of impedance"
magZ_x_D=(Magnitude(Z_x_d))"[1/m-s]"
"phase of impedance"
theta_Z_x_D=AngleDeg(Z_x_D)"[deg]"
"set impedance equal imdedance caused by mass flow"
magZ_x_D=R*T*P_pt_r^2*cos(theta_rZ_x_D)/(2*P_0_r*W_dotpt)

"==========================================================================="
"                                  End                                     "
"==========================================================================="
```

APPENDIX B

```
"================================================================"
"            Lumped parameter model                                  "
"================================================================"

GAS$='Helium'
"mean temperature"
Tbar=293 [K]
"mean Pressure"
Pbar=10.43e5 [Pa]
"pressure amplitude"
DP=1.244e5 [Pa]
"frequency"
freq=10.81 [Hz]
"inertance tube length"
L_line_ft_r=5
L_line_ft_i=0
L=L_line_ft*convert(ft,m)
"tube's wall thickness"
t_tube=0.031*convert(inch,m)
"tube diameter"
D=(0.375-2*t_tube)*convert(inch,m)
"reservoir volume"
V_res=1[gal]*convert(gal,m^3)
"specific gas constant"
Rg=R#*convert(kJ,J)/MOLARMASS(GAS$)
"specific heat"
cPg=cP(GAS$,P=Pbar,T=Tbar)
"polytropic exponent (abiabatic)"
k_ad=cPg/(cPg-Rg)
k=k_ad
"viscosity"
mu=viscosity(GAS$,T=Tbar,P=Pbar)
"density"
rho=Pbar/(Rg*Tbar)

"angular frequency"
omega=2*pi*freq
"total line compliance"
C_line=pi*D^2*L/(4*k*Rg*Tbar)
"reservoir compliance"
C_res=V_res/(k*Rg*Tbar)
"guessed mass flow to obtain guess values for EES"
m_dot_guess= m_dot
"Reynolds number of helium flow inside the tube"
Re=m_dot_guess*8/(pi^2*D*mu)
"friction factor"
f=0.046*Re^(-0.2)
"resistance of line"
R_line=f*64*m_dot_guess*L/(pi^3*rho*D^5)
"inertance of line"
```

```
L_line=4*L/(pi*D^2)
"half the line's compliance plus reservoir compliance"
Z_C2=1/(j*omega*(C_line/2+C_res))
"reservoir impedance"
Zres=(1/Z_C2)^(-1)
"resistance impedance of line"
Z_Rline=R_line
"inertance impedance of line"
Z_Lline=j*omega*L_line
"half the line's compliance"
Z_C1=1/(j*omega*C_line/2)
"total imdeance of line and reservoir"
Z=(1/Z_C1+1/(Zres+Z_Rline+Z_Lline))^(-1)
"get m_dot from impenace"
m_dot=DP/abs(Z)
"convert into gramms"
m_dot_gps=m_dot*convert(kg/s,g/s)
"phase angle"
theta=AngleDeg(Z)

"================================================================================"
"                              End                                               "
"================================================================================"
```

APPENDIX C

```
"================================================================"
"            Distributed component model                                          "
"================================================================"

"Input values"
"Number of desired increments"
n_r=10
n_i=0
"Mean pressure"
Pbar_r=10.26e5 [Pa]
"Pressure amplitude"
DP_r=1.8566e5  [Pa]
"Length of inertance tube in feet"
L_line_ft_r=40
"Outer diameter of the tube in inch"
OD_tube_r=0.5
"Measured Entrance Effect"
R_ent_r=232419
"Wall thickness of the tube in inch"
t_tube=0.032
"Volume of the reservoir in gallons"
V_res_gal=2.075
"Frequency of the compressor"
freq=15.27 [Hz]
"Average temperature"
Tbar=293 [K]
"Operating gas"
GAS$='Helium'
"Set imaginary part to zero"
R_ent_i=0
Pbar_i=0
DP_i=0
L_line_ft_i=0
OD_tube_i=0

"Calculate the knowns and convert"
D=(OD_tube-2*t_tube)*convert(inch,m)
L=L_line_ft*convert(ft,m)
V_res=V_res_gal*convert(gal,m^3)
Rg=R#*convert(kJ,J)/MOLARMASS(GAS$)
cPg=cP(GAS$,P=Pbar,T=Tbar)
"Heat capacity ratio"
k_ad=cPg/(cPg-Rg)
k=k_ad
mu=viscosity(GAS$,T=Tbar,P=Pbar)
rho=Pbar/(Rg*Tbar)
"Angular frequency"
omega=2*pi*freq

"Calculate the compliances and their impedance"
```

```
"Reservoir compliance"
C_res=V_res/(k*Rg*Tbar)
"Reservoir impedance of compliance"
Zr=(1/(j*omega*C_res))
"Compliance of entire tube"
C_line=pi*D^2*L/(4*k*Rg*Tbar)
"Impedance of the compliance of one increment"
Z_Cn=(1/(j*omega*C_line/(n_r)))
"Inertance of the entire line"
L_line=4*L/(pi*D^2)
"Impedance of the inertance of one increment"
Z_L=j*omega*L_line/n_r
"Calculate the resistance per element"
DUPLICATE            do=1, n_r
  Re[do]=m_dot_mag[do]*8/(pi^2*D*mu)
END
"Calculate the friction factor per element"
DUPLICATE            do=1,n_r
  f[do]=0.046*Re[do]^(-0.2)
END DO
"Impedance of the resistance of one increment"
DUPLICATE            do=1,n_r
  R[do]=f[do]*64*m_dot_mag[do]*L/n_r/(pi^3*rho*D^5)
END
"Impedance of Resistance and inertance combined"
DUPLICATE            do=1,n_r
  Zrl[do]=R[do]+Z_L
END

"Set up entire impedance starting from the inside"
"Total reservoir impedance (including entrance effect)"
Z_res=R_ent+Zr
"First impedance in series"
Z_s[1]=Z_res+Zrl[1]
"Impedance in parallel"
DUPLICATE do=1,n_r
  Z_p[do]=(Z_s[do]^(-1)+Z_Cn^(-1))^(-1)
END
"Impedance in series"
DUPLICATE do=2,n_r
  Z_s[do]=Z_p[do-1]+Zrl[do]
END
"nth impedance in parallel equals total impedance of network"
Z=Z_p[10]
"Calculate mass flow at inertance inlet"
m_dot[11]=DP/Z

"Calculate pressures and mass flow along the line"
"Pressure at inertance inlet"
P[12]=DP
"Pressure drop across reservoir entrance"
P[2]-P[1]=m_dot[1]*Z_ent
"Pressure drop across elements"
```

```
DUPLICATE do=2,n_r+1
  P[do+1]-P[do]=m_dot[do-1]*Zrl[do-1]
END
"Mass flow accumulated in the elements"
DUPLICATE do=1,n_r
  m_dot_c[do]=P[do+2]/Z_Cn
END
"Pressure in reservoir"
P[1]=m_dot[1]*Zr
"Kirchhoffs Law"
DUPLICATE do=2,n_r+1
  m_dot[do]=m_dot[do-1]+m_dot_c[do-1]
END

"Mass flow Magnitudes"
DUPLICATE       do=1,n_r+1
  m_dot_mag[do]=MAGNITUDE(m_dot[do])
END
"Magnitude of Pressure"
DUPLICATE       do=1, n_r+2
Pressure[do]=Magnitude(P[do])
END
"Phase angles of pressure along the line"
DUPLICATE       do=1,n_r+2
theta_p[do]=angledeg(P[do])
END
"Phase angles of mass flow along the line"
DUPLICATE       do=1,n_r+1
theta_m[do]=angledeg(m_dot[do])
END
"Mass flow at compressor outlet"
m_dot_compressor=m_dot_mag[11]
"Mass flow into reservoir"
m_dot_reservoir=m_dot_mag[1]
"Phase angle of impedance"
theta_compressor=-ANGLEDEG(Z_p[10])
"Accoustic power"
W=0.5*Rg*Tbar/Pbar*m_dot_mag[11]*DP*(cos(theta_m[11]*convert(deg,rad)))

"==================================================================="
"                    END                                              "
"==================================================================="
```

APPENDIX D

```
"=================================================================="
"                    Heat Exchanger Code                                              "
"=================================================================="

"Function for number of transfer units"
Function NTU(epsilon,C_r)
IF (C_r<1) THEN
           NTU:=1/(C_r-1)*ln((epsilon-1)/(epsilon*C_r-1))
ELSE
          NTU:=epsilon/(1-epsilon)
ENDIF
end

"Function for Nusselt Number"
Function Nu#_f(Re_f, Pr_W,f)
If (Re_f>2300) THEN
          Nu#_f=((f/8)*Re_f*Pr_W)/(1+12.7*(f/8)^0.5*(Pr_W^(2/3)-1))
ELSE
          NU#_f=4.36
ENDIF
end

$Bookmark Geometry
"Inner diameter of outer tube in inch"
d_o_i_inch=2.6
"Outer diameter of inner tube in inch"
d_i_o_inch=2.5
"Inner diameter of inner tube in inch"
d_i_i_inch=2
"Convertion of inch into m"
d_o_i=d_o_i_inch*Convert(inch,m)
d_i_o=d_i_o_inch*Convert(inch,m)
d_i_i=d_i_i_inch*convert(inch,m)
"Cross-sectional area of Helium-flow"
A_He=pi*d_i_i^2/4

$Bookmark Fluid Properties
"Heat capacity of water"
cp_w=CP(Water,T=T_W,P=P_W)
"Heat capacity of helium"
cp_He=CP(Helium,T=T_He,P=P_He)
"Density of water"
rho_w=DENSITY(Water,T=T_W,P=P_W)
"Density of Helium"
rho_He=DENSITY(Helium,T=T_He,P=P_HE)
"Viscosities "
mu_W=VISCOSITY(Water,T=T_W,P=P_W)
mu_W_w=VISCOSITY(Water,T=T_Cu,P=P_W)
mu_He=VISCOSITY(Helium,T=T_He,P=P_He)
"Prandel Number s"
```

```
Pr_W=PRANDTL(Water,T=T_W,P=P_W)
Pr_He=PRANDTL(Helium,T=T_He,P=P_He)
"Conductivities"
k_W=CONDUCTIVITY(Water,T=T_W,P=P_W)
k_He=CONDUCTIVITY(Helium,T=T_He,P=P_He)
k_Cu=k_('Bronze', T_Cu)

$Bookmark Temperatures and Pressures
"Temperature of helium at the outlet" T_He_o=295
"Temperature of water at the inlet"
T_W_i=283.2
"Mean Temperature of the wall"
T_Cu=(T_W+T_He)/2
"Pressure of water at inlet, psi"
P_w_psi=47
P_w=P_w_psi*convert(psi,bar)
"Mean pressure of helium"
P_He=20
"Mean water Temperature"

T_W=(T_W_o+T_W_i)/2
"Mean heliumTemperature"
T_He=(T_He_i+T_He_o)/2

$Bookmark Mass flow rates
"Mass flow of Helium"
m_dot_He=0.02
"Mass flow of water"
m_dot_w_inlet_gal=3
m_dot_w_inlet=m_dot_w_inlet_gal*Convert(gal/min,m^3/s)*rho_w
m_dot_w=m_dot_w_inlet
"Heat to remove"
Q_dot_rem=2
"Heat transfer of water"
Q_dot_w=m_dot_w*cp_w*(T_w_o-T_w_i)
"Heat transfer of helium"
Q_dot_He=m_dot_He*cp_He*(T_He_i-T_He_o)
Q_dot_w=Q_dot_rem
Q_dot_He=Q_dot_rem

$Bookmark Reynolds Numbers
"Maximum mass velocity"
G=m_dot_He/(porosity*A_fr)
"Reynolds for flow inside the screens"
Re_screens=G*d_w_h/mu_He
"Velocity of water"
v_W=m_dot_w/(s_f_spacing*s_f_length*rho_w)
"Hydraulic diameter fin passage"
d_h_f=4*s_f_spacing*s_f_length/(2*s_f_spacing+2*s_f_length)
"Reynoldsnumber in fin passage"
Re_f=d_h_f*v_W*rho_W/mu_W
```

```
$Bookmark Heat capacity rates and HX assumed HX efficiency
"Heat capacity rates"
C_1=m_dot_He*cp_He
C_2=m_dot_w_inlet*cp_W
C_min=min(C_1,C_2)
C_max=max(C_1,C_2)
"Heat capacity rate ratio"
C_r=C_min/C_max
"Assumed HX efficiency"
epsilon=C_1*(T_He_i-T_He_o)/C_min/(T_He_i-T_W_i)

$Bookmark Outer Fin Calculations
"Geometry"
"Outer fin diameter"
d_f_o_o=d_i_o
"Inner fin diameter"

d_f_o_i=d_i_o-2*s_f_length
"Fin thickness"
s_f_inch=.12
"Fin length"

s_f_length_inch=.08
"Gap between fins"
s_f_spacing_inch=.12
s_f=s_f_inch*Convert(inch,m)
s_f_length=s_f_length_inch*Convert(inch,m)
s_f_spacing=s_f_spacing_inch*Convert(inch,m)
"Wall thickness of inner tube"
wallthickness=(d_i_o-2*s_f_length-d_i_i)/2
"Fin inner radius"
r_f_i=(d_i_o-2*s_f_length)/2
"Fin outer radius"
r_f_o=d_i_o/2
"Modified radius"

r_f_o_c=r_f_o+(s_f/2)
"Surface area of outer fins"
A_f_o=(2*pi/4*(d_f_o_o^2-d_f_o_i^2))*N_f
"Surface area of base"
A_b=d_f_o_i*pi*s_f_spacing*N_f
"Total surface area"
A_t=A_f_o+A_b
"Number of fins"

N_f=L_f/(s_f_spacing+s_f)

"Friction factor"
f=0.184*Re_f^(-0.2)
"Nusselt Number"
Nu#_f=Nu#_f(Re_f, Pr_W,f)
"Convection coefficient"
```

```
h_f=Nu#_f*k_W/d_h_f

"Fin efficiency"
m=sqrt((2*h_f)/(k_Cu*s_f))
C2=(2*r_f_i/m)/(r_f_o_c^2-r_f_i^2)
"fin efficiency"
eta_f=C2*(Bessel_K1(m*r_f_i)*Bessel_I1(m*r_f_o_c)-
Bessel_I1(m*r_f_i)*Bessel_K1(m*r_f_o_c))/(Bessel_I0(m*r_f_i)*Bessel_K1(m*r_f_o_c)+Bessel_K0(m
*r_f_i)*Bessel_I1(m*r_f_o_c))
"Overall fin efficiency"
eta_0=1-A_f_o/A_t*(1-eta_f)


$Bookmark Screen Characteristics
"Wire diameter"
d_w=144.3E-6
"Spacing"
s_w=254E-6
"Hydraulic diameter of screens"
d_w_h=209.13E-6
"Screen diameter"
d_s=d_i_i
"Number of screens"
N_screens=L_f/(2*d_w)
"Porosity"
porosity=0.6466
"Specific volume"
alpha=pi/s_w
"ratio of free flow area to frontal area"
sigma=(s_w/d_w-1)^2/(s_w/d_w)^2
A_c_screens=sigma*A_fr
"Frontal aera"
A_fr=pi/4*d_i_i^2
"Total screen volume"
V=pi/4*d_i_i^2*L_f
"uncorrected pin length"
L_s_u=sqrt(pi)/4*d_s
"corrected pin length"
L_s_r=L_s_u*1.11

$Bookmark Fin Efficiency for Screens
"Modified pin length"
L_s_c=L_s_r+d_w/4
m_s=sqrt((4*h_screens)/(k_Cu*d_w))
"Screen efficiency"
eta_f_screens=tanh(m_s*L_s_c)/(m_s*L_s_c)
"Total screen efficiency"
eta_0_screens=eta_f_screens

$Bookmark Colburn Factor and total heat transfer coefficient
"Colburn factor"
j=(h_screens/(G*cp_He*Convert(kJ,J)))*Pr_He^(2/3)
"Colburn factor for porosity of 0.67"
```

```
j=0.11
"Geometry Coefficient"
F_star_f=2*pi*L_f/ln(r_f_o/r_f_i)
"Total surface of screens"
A_screens=V*alpha

$Bookmark Total heat transfer coefficient
"Total heat transfer coefficient"
1/(UA_f)=1/(h_f*eta_0*A_t)+1/(k_Cu*F_STAR_f)+1/(h_screens*A_screens*eta_0_screens)
NTU=UA_f/(C_min*Convert(kW,W))
NTU=NTU(epsilon,C_r)

"============================================================="
"                 END                                         "
"============================================================="
```